MAGNETICALLY ORDERED RELAXOR FERROELECTRIC LEAD IRON TUNGSTATE AND RELATED MATERIALS: SYNTHESIS, STRUCTURE & PROPERTIES

by

Li Feng

B. Sc., Sichuang University, 1982
M. Sc., CIAC, Chinese Academy of Sciences, 1989
M. Sc., New Orleans University, 1999

THESIS SUBMITTED IN PARTIAL FULFILLMENT OF
THE REQUIREMENTS FOR THE DEGREE OF

DOCTOR OF PHILOSOPHY

In the Department
of
Chemistry

SIMON FRASER UNIVERSITY

Spring, 2007

APPROVAL

Name: Li Feng

Degree: Doctor of Philosophy

Title of Thesis: Magnetically Ordered Relaxor Ferroelectric Lead Iron Tungstate and Related Materials: Synthesis, Structure & Properties

Examining Committee:

Dr. Vance E. Williams
Chair
Assistant Professor

Dr. Zuo-Guang Ye
Senior Supervisor
Professor, Department of Chemistry

Dr. Colin H. Jones
Supervisor
Professor, Department of Chemistry

Dr. Daniel B. Leznoff
Supervisor
Associate Professor, Department of Chemistry

Dr. Steven Holdcroft
Internal Examiner
Professor, Department of Chemistry

Dr. Arthur Mar
External Examiner
Professor, Department of Chemisty
University of Alberta

Date Approved: March 20, 2007

ABSTRACT

A complete ceramic solid solution between relaxor ferroelectric $Pb(Fe_{2/3}W_{1/3})O_3$ (PFW) and normal ferroelectric $PbTiO_3$ (PT), [(1-x)PFW-xPT] has been synthesized by a modified B-site precursor method and characterized by X-ray diffraction, differential scanning calorimetry, and dielectric measurements. It was found that, with the increase of PT content, the perovskite structure gradually changes from the pseudo-cubic to a tetragonal phase at room temperature, accompanied by the transformation from the relaxor ferroelectric behaviour of PFW to a normal ferroelectric state in the binary system. A phase diagram between PFW and PT has been established, which displays a morphotropic phase boundary (MPB) within the composition interval $0.25 \leq x \leq 0.35$.

The electrical transport properties of the polycrystalline dielectric/ferroelectric ceramics of (1-x)PFW-xPT have been studied with the help of complex ac impedance spectroscopic measurements combined with electric modulus formalism analysis. In particular, the resistivity, capacitance (or dielectric constant) and electric modulus at different temperatures have been analysed, and the electric contributions from each microstructural component (phase) have been assigned, which reveals that the ferroelectric behaviour of the system is dominated by the bulk (grain) phase of the ceramic materials.

Single crystals of the complex perovskite solid solution (1-x)PFW–xPT have been synthesized by the high temperature solution growth method using PbO as flux, and characterized by X-ray diffraction, dielectric and magnetic measurements. The relaxor ferroelectric behaviour of the crystals ($x \leq 0.27$) was fitted to the Vogel-Fulcher relaxation model. The macroscopic polarization induced under an alternating electric field was investigated and the influence of the PT component on the relaxor and ferroelectric behaviour was revealed in the PFW–PT single crystals.

Two types of magnetic ordering have been observed in the temperature dependence of magnetization in the crystals with $x \leq 0.27$. Weak low-temperature ferromagnetism was found to be enhanced by the addition of ferroelectric PT up to $x = 0.27$. The intrinsic relations between the perovskite structure, composition, magnetic ordering, and ferroelectric relaxation was discussed.

The ^{57}Fe-enriched PFW and 0.75PFW–0.25PT ceramic materials have been further investigated by Mössbauer spectroscopy. The influences of temperature and PT component on the spectra are discussed.

DEDICATION

To my dear parents, Xianke Feng and Zibi Zhao,

My brother, Ya Feng, and my sister, Yu Feng

And my nephews, Chi Feng, and Taiyi Xiang

To my beloved wife, Huaie Wang, and adorable daughter, Lucy (Yun) Feng

And to everyone who helped make this possible

ACKNOWLEDGEMENTS

I would like to thank my supervisor, Dr. Z.-G. Ye, for giving me the opportunity to finish the PhD research work and thesis, and for his extremely helpful guidance and continuous encouragement.

I would also like to thank the members of my supervisory committee, Dr. D. B. Leznoff and Dr. C. H. Jones, for their valuable suggestions, advice, and encouragement during my thesis work.

I would like to thank Dr. S. Holdcroft as the internal examiner of my thesis.

I would like to thank Dr. A. Mar as the external examiner of my thesis.

I would also like to thank the past and present members of our group for providing me with help, support and friendship. Especially, I would like to thank Dr. H. Guo and Dr. Simon Trudel for his great help and useful discussions on magnetic measurements.

I am appreciative of the members of Department of Chemistry for their support.

Finally, I would like to thank Dr. Z.-G. Ye and Simon Fraser University for their generous financial support.

Table of Contents

List of Tables

LIST OF FIGURES

List of Abbreviations

BT	$BaTiO_3$
DSC	differential scanning calorimetry
E_a	activation energy
E_C	coercive field
EDX	energy-dispersive x-ray spectroscopy
H_{hf}	magnetic hyperfine field
J	imaginary number $[(-1)^{1/2}]$
LFD	low-frequency dispersion
LRO	long range order
ME	magnetoelectric
MPB	morphotropic phase boundary
MPMS	Magnetic Properties Measurement System
M*	complex electric modulus
PBN	$(Pb_{1-x}Ba_x)Nb_2O_6$
PFW	$Pb(Fe_{2/3}W_{1/3})O_3$
PFT	$Pb(Fe_{1/2}Ta_{1/2})O_3$
PIN	$Pb(In_{1/2}Nb_{1/2})O_3$
PLZT	$(Pb_{1-3x/2}La_x)(Zr_yTi_{1-y})O_3$
PMN	$Pb(Mg_{1/3}Nb_{2/3})O_3$
PSN	$Pb(Sc_{1/2}Nb_{1/3})O_3$
PST	$Pb(Sc_{1/2}Ta_{1/2})O_3$
PT	$PbTiO_3$
PZN	$Pb(Zn_{1/3}Nb_{2/3})O_3$
RC	time constant (products of resistance and capacitance)
SQUID	Superconducting Quantum Interference Device
SRO	short range order
Tc	Curie temperature
T_d	dipole temperature
TEM	transmission electron microscopy

T_f	the temperature of dynamic freezing of the polar clusters
T_m	the temperature of the maximum dielectric constant
T_{MPB}	the temperature corresponding the MPB phase transition
T_N	Néel temperature
V-F	Vogel-Fulcher
XRD	X-ray diffraction
Z*	complex impedance
ε_o	the permittivity of free space
ε'	real permittivity
ε''	imaginary permittivity
Δ	quadrupole splitting
σ	conductivity
ρ	resistivity
δ	isomer shift
λ	wavelength
γ	gamma ray
χ	magnetic susceptibility

Chapter 1:
General Introduction

1.1 Ferroelectrics

A ferroelectric crystal is defined as a crystal that belongs to the pyroelectric family and exhibits a spontaneous polarization that can be switched by an electric field from one ground orientation state to the other [1]. Ferroelectric materials are a special type of dielectric having extremely large permittivity and the possibility of retaining some residual electrical polarization after an applied field is switched off.

Ferroelectrics can be characterized by the ferroelectric hysteresis loop, as shown in Fig. 1.1. When an electric field applied across a ferroelectric substance is increased, the induced polarization increases nonlinearly up to the saturation value P_S (if the electric field is high enough) because all of the ferroelectric domains align in the direction of the field. The P_S represents the spontaneous polarization [2]. As the electric field is reversed and removed completely, the polarization at zero field is called the remnant polarization, P_r. In this case, some of the domains remain aligned. With the applied field increasing to some extent in the opposite direction, the remnant polarization decreases to zero. The reverse electric field required to reduce the polarization to zero is called the coercive field, E_C. A saturation polarization in the reverse direction can be obtained if the opposite field applied is large enough. Consequently, the hysteresis loop of a ferroelectric can be established after the electric field cycle is applied on the ferroelectric sample.

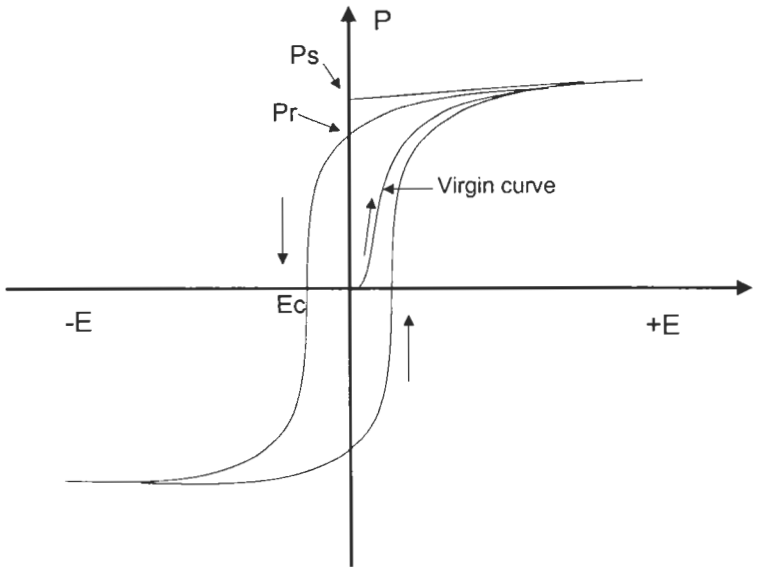

Figure 1.1: Typical electric field hysteresis loop displayed by ferroelectrics.

The spontaneous polarization usually decreases with increasing temperature and becomes zero at temperature T_C. This phase transition temperature, T_C, is called the Curie point. Ferroelectric phases can exist only below this temperature. Above T_C, a paraelectric phase appears, and the dielectric constant (ε) as a function of temperature, T, is given by the Curie–Weiss law:

$$\varepsilon = [C/(T-\theta)] + \varepsilon_\infty \quad , \qquad (1.1)$$

where C is the Curie-Weiss constant, θ is the Curie-Weiss temperature and ε_∞ is the part of the dielectric constant independent of temperature. ε_∞ can be neglected at temperatures near T_C [1].

Spontaneous polarization is always accompanied by crystal lattice deformation. A structural requirement for a crystal to have spontaneous polarization and to be ferroelectric is that its space group must be non-centrosymmetric. In order to change the polarization direction by reversing an applied field, an energy barrier between the two

polarization states (±P) has to be overcome. A one-dimensional free energy (G) plot against polarization (P) is presented in Fig 1.2 [3]. The potential energy barrier ΔE is temperature dependent [3]. As the temperature increases to T_C, the ΔE decreases to zero and spontaneous polarization disappears.

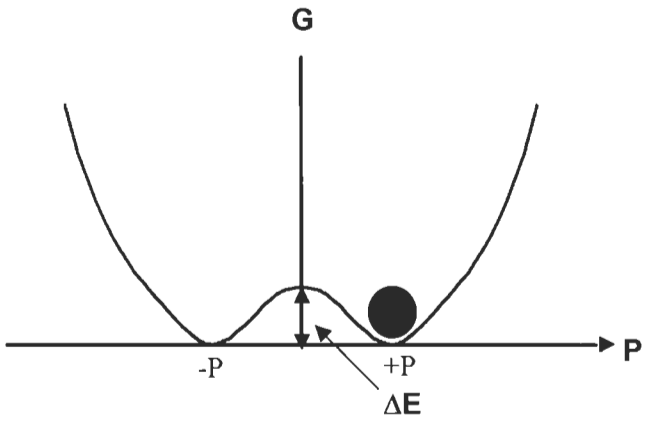

Figure 1.2: One dimensional free energy diagram, in terms of free energy (G) vs. polarization (P). A potential energy barrier (ΔE) has to be overcome from polarization states +P to –P.

1.2 Ferroelectric Perovskite Compounds

Many Pb-based perovskite compounds (general formula ABO_3) display ferroelectric behaviour because of their specific structure, as shown in Fig. 1.3. It has a primitive cubic structure, with A atoms at the cube corners, B atom at the body centre, and the oxygen atoms at the face centres. The perovskite structure can also be composed of a set of BO_6 octahedra arranged in a simple cubic pattern and linked together by shared oxygen

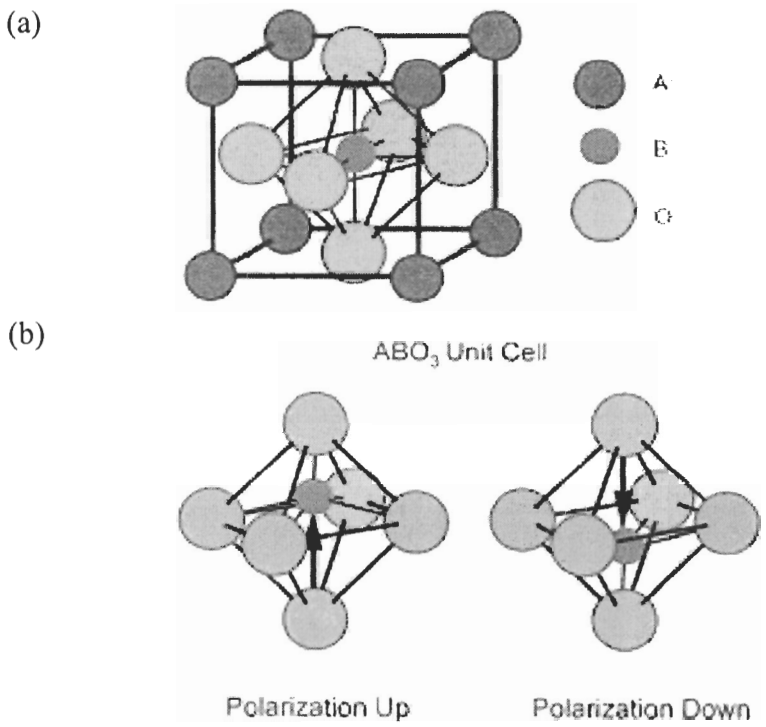

Figure 1.3: Perovskite ABO_3 unit cell, illustrating 180 ^{o} polarization reversals.

atoms, with the A atoms occupying the spaces between them. Cations A (Pb^{2+}, Ba^{2+}, Ca^{2+}, etc.) with lower charge and larger size occupy twelve coordinate cavities within this framework. Cation B (Ti^{4+}, Sc^{3+}, Zr^{4+}, Sn^{4+}, etc.) in octahedral site usually has smaller size with higher charge. There are minimum-energy positions off-center from the original octahedron that can be occupied by the B atom. Therefore, it is possible for the structure to be distorted and to demonstrate non-centric and polar symmetry, which results in the formation of dipoles even without an electric field being applied (Fig. 1.3b). The first ferroelectric perovskite compound discovered was $BaTiO_3$ [4, 5, 6]. It behaves as a

normal dielectric above T_C = 120 °C. However, below that temperature, Ti is displaced from its central position towards one of the apical oxygen atoms, which gives rise to a spontaneous polarization, as shown in Fig. 1.3b. It has been confirmed by X-ray diffraction that Ti is displaced by ~ 0.1 Å from the center of its octahedron in the direction of one of the oxygen atoms. Another example is complex perovskite $PbTiO_3$ [PT], which undergoes a first-order transition at T_C = 490 °C from cubic perovskite to a tetragonal ferroelectric one upon cooling and exhibits a significant displacement of small cation Ti^{4+} in octahedral B-site below the Curie temperature T_C [7, 8]. It is a typical ferroelectric with a sharp maximum of dielectric constant at the Curie temperature.

1.3 Relaxor Ferroelectrics

Differing from normal ferroelectrics, relaxor ferroelectrics exhibit a broad and diffuse maximum of dielectric permittivity around the temperature T_m with strong frequency dispersion [9], as shown in Fig. 1.4. The magnitude of the maximal dielectric constant decreases with the increasing frequency, while the corresponding T_m shifts toward higher temperature. There is no macroscopic phase transition into a ferroelectric state around T_m, not even a "diffuse" one. Neither birefringence nor macropolarization can develop without the application of an external electric field, the materials remaining isotropic to long coherent probing radiation, like polarized light, X-ray and neutron beams [10]. In addition, the local polarization and polar nano domains occur below a dipole temperature T_d far above the temperature of the maximal dielectric permittivity T_m, while the (induced) macro polarization vanishes at a temperature well below T_m.

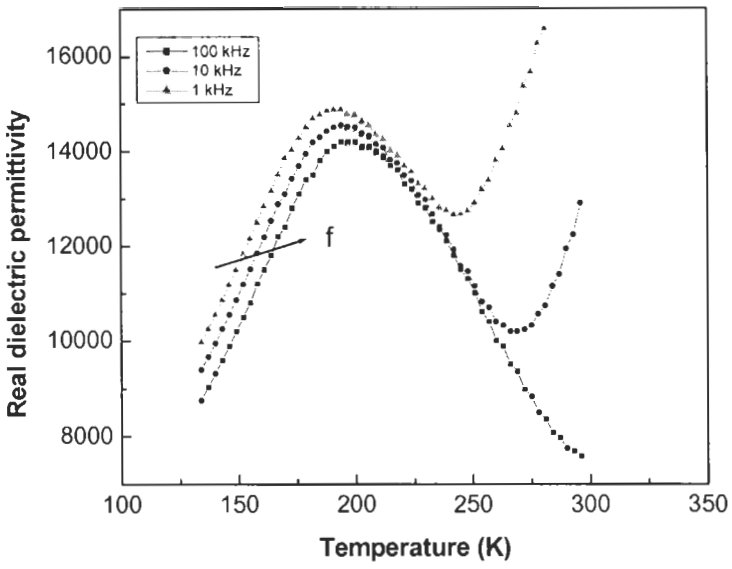

Figure 1.4: Typical temperature and frequency dependences of dielectric constant for the relaxor ferroelectric $Pb(Fe_{2/3}W_{1/3})O_3$ [PFW] [37].

The dielectric relaxation in relaxors is closely associated with the microstructural properties, the correlation of the local polar domains, and the ordered/disordered nanostructure. For example, in a complex perovskite compound $A(B'B'')O_3$, octahedral B-site positions (Fig.1.3) are occupied by B' and B" cations at random. On the nanoscopic scale, composition fluctuations and partial ordered/disordered nanostructure resulting in polar nanoregions (or clusters) are expected to exist, and are believed to be the main origin of the relaxor ferroelectric behaviour [9-11]. X-ray and neutron diffraction have also confirmed the positional disorder giving rise to the formation of the local dipole moment and polarization in relaxor ferroelectric $Pb(Mg_{1/3}Nb_{2/3})O_3$ [PMN] [12], $Pb(Fe_{2/3}W_{1/3})O_3$ [PFW] [13] and $Pb(Fe_{1/2}Ta_{1/2})O_3$ [PFT] [14]. Together with local

polar structure, the positional disorder and the related lattice distortion exhibit some structural factors essential to the relaxor behaviour.

The local distortions due to ionic displacements are in fact not totally random, but correlated. The correlation increases upon cooling, which is also the origin of the relaxor behaviour. The degree of order / disorder in the perovskite structure and the coherent length of the ordered nanodomains have a great influence on the relaxor ferroelectric properties [15, 16]. With increasing degree of order, the coherence length increases, causing the relaxor ferroelectric phase transition into a normal ferroelectric phase.

In order to explain the possible mechanism of the dispersive dielectric relaxation and the polarization behaviour, various models have been proposed. Among them, the diffuse phase transition model [17, 18], the superparaelectric model [19], the dipolar glassy-like model [20], and the random field-stabilized domain model [21, 22] have received the most attention.

The diffuse phase transition and polar regions were proposed by Smolenskii *et al.* [17, 18] for the explanation of the broadened dielectric peak at T_m. It was believed that the compositional fluctuations on the B-sites with disordered B' and B" occupation in $A(B'B")O_3$ cause the chemical inhomogeneity, which gives rise to various polar microregions with a distribution of the local Curie temperatures. The temperature T_m represents the mean Curie temperature. Therefore, a broadened phase transition occurs at T_m.

Cross [11] proposed the superparaelectric model for the relaxor ferroelectrics by analogy with the superparamagnetic state. It describes the nature of the micropolarization at high temperatures, in the region above T_m, where the micro polar regions are

considered to be dynamically disordered by thermal motion. Such a disordered state is not totally random, but shows some preferential orientation along one of the possible polar directions for a cluster of dipoles, leading to a net polarization in a micro domain. In the lower temperature region, the slowing down of the dynamics of polar clusters and their correlation obviously affect or attenuate the dielectric response and the polarization behaviour, giving rise to characteristic relaxor ferroelectric behaviour.

In the dipole glassy-like model, it is pointed out that the size of the polar regions and the potential barrier increase upon cooling. The dynamics of the polar regions will slow down, leading to a freezing of the dipoles, as in the case of the spin glasses in the dipole glass system [10]. The temperature dependence of the dielectric constant shows a broad maximum near the paraelectric to dipole glass transition due to a dynamic freezing. The dielectric relaxation can be described by the Vogel-Fulcher (V-F) equation, in terms of the AC frequency ω and the temperature T_m of the maximal dielectric constant:

$$\omega = \omega_0' \exp[-E_a / k(T_m - T_f)], \qquad (1.2)$$

where ω_0' is a fitting constant, E_a is the activation energy and T_f is the temperature of dynamic freezing of the polar clusters due to interactions. Satisfying the V-F equation is considered as a sign of freezing of the dipole system at T_f [20].

In the random field-stabilized domain model, proposed by Westphal and Kleemann [21, 22], it is stressed that the relaxor ferroelectricity in PMN can be attributed to the strong contribution of a quenched random electric field, arising from the charged nanodomains and the compositional fluctuations and chemical textures [23]. The random-fields are believed to be at the origin of the critical slowing-down, and freezing into

nanometric ferroelectric domains and the slow relaxation of the polarization below the Curie temperature.

Recently, Bokov and Ye [24, 25, 26] have discovered the "universal" relaxor dispersion in the perovskite PMN and related materials in the dielectric spectroscopic studies. The universal relaxor polarization can be described by a microscopic model of 'soft' polar nanoregions with unit cells that can freely choose several different directions, while the direction of the total moment of the nanoregion remains the same [26]. Hence, it is possible to apply a standard spherical model to relaxor ferroelectrics, which predicts the experimentally observed quadratic divergence of the universal part of the susceptibility above the critical temperature. The model is complementary to the so-called spherical random bond-random field model proposed by Blinc *et al.* [27].

1.4 Magnetic Properties

1.4.1 The Curie-Weiss Law

Because there are strong analogies between magnetic properties and the corresponding electrical properties, e.g. ferromagnetism *vs.* ferroelectricity, it is necessary to review some magnetic concepts here.

Generally speaking, any inorganic solid compound that has magnetic effects (interactions) must have unpaired d or f electrons on metal cations [28, 29]. The magnetic moments of unpaired electrons arise from electron spin and electron orbital motion around the nucleus. How the unpaired electrons are oriented depends on the magnitude of magnetic interaction energy between adjacent unpaired electrons or adjacent spins, which bring about different magnetic interaction behavior. If the atomic moment is oriented at

random, the whole material is paramagnetic, as shown in Fig. 1.5a. When the interaction energy is strong enough, the atomic moments are aligned parallel. The system is then said to be ferromagnetic (Fig. 1.5b). In some cases, the atomic moments form two sublattices. The magnetic moment on one sublattice is equal in magnitude, but aligned antiparallel to the other (Fig. 1.5c). The net magnetic moment is zero at very low temperature (0 K in theory). The system is said to be antiferromagnetic [28].

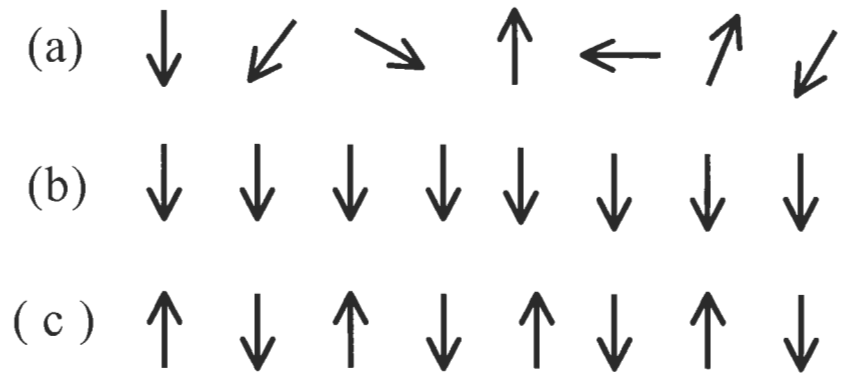

Figure 1.5: Schematic of magnetic phenomena in a one-dimensional crystal: (a) paramagnetism; (b) ferromagnetism; and (c) antiferromagnetism.

When a substance is placed in a magnetic field, all atomic moments will interact with the applied field and be reoriented, resulting in the magnetization of the substance. The ratio of the magnetization of the substance to the field is defined as the magnetic susceptibility χ,

$$\chi = M / H \quad , \tag{1.3}$$

where M is the specific magnetic moment (emu/g) and H is the magnetic field (Oe). The magnetization curve of M vs. H can often indicate different magnetic interaction

behaviour. The magnetic susceptibility is inversely proportional to temperature for a paramagnetic material. Within a paramagnetic substance, some spontaneous interactions between adjacent spins take place, which may develop into ferro- or anti-ferromagnetism at low temperatures. The high temperature magnetic behaviour of paramagnetic region is often described by the Curie-Weiss law [29]:

$$\chi = C / (T-\theta), \qquad (1.4)$$

where C is the Curie constant and θ is the Weiss constant. The different sign of θ indicates the different magnetic interaction in the range of temperature, as shown in Fig. 1.6.

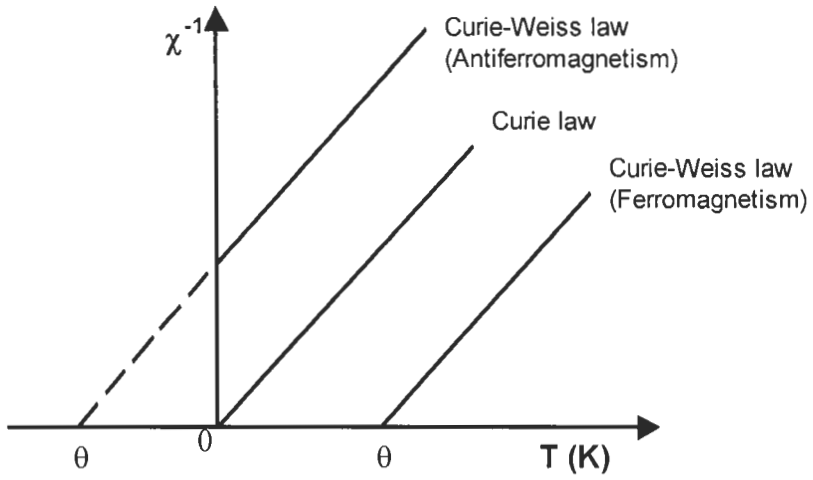

Figure 1.6: Reciprocal magnetic susceptibility vs. temperature for substances that show various magnetic features at different temperatures.

(a) For paramagnetic substances that show no tendency to magnetic order, the Weiss constant is zero.

(b) In the paramagnetic substances that show a tendency to ferromagnetic order, there is already some local alignment of spins. Hence, the Weiss constant has a positive value. The temperature that equals to the absolute value of θ is called the ferromagnetic Curie temperature T_C, below which the substance is ferromagnetic and does not obey the Curie-Weiss relationship.

(c) For the paramagnetic substances that show a tendency to antiferromagnetic order, the Weiss constant has a negative value. The temperature that equals the absolute value of θ is called the Néel temperature, T_N, below which the sample is antiferromagnetic. When the temperature is below T_N, the tendency toward antiparallelism becomes stronger. The antiparallel alignment will be perfect at 0 K. Thus, antiferromagnetic substances have a small positive susceptibility at all temperatures.

1.4.2 Magnetic Hysteresis Loop

Similar to the ferroelectric materials, ferromagnetic materials also have a domain structure. Within each domain, the spins align parallel. Different domains have different spin orientations and can be aligned parallel to an applied magnetic field on them. A magnetic hysteresis loop occurs in the plot of magnetization M against magnetic field H, as shown in Fig. 1.7. Similar to the definition in a dielectric hysteresis loop, at large enough magnetic field (H), a saturated magnetization (M_S) can be obtained. M_r is the remnant magnetization as H decreases to zero, and H_C is the coercive force for removing all induced magnetization from the magnetic substance. The area in the hysteresis loop is expressed as hysteresis loss or loss energy when a cyclic magnetic field is applied to a ferromagnetic substance [28].

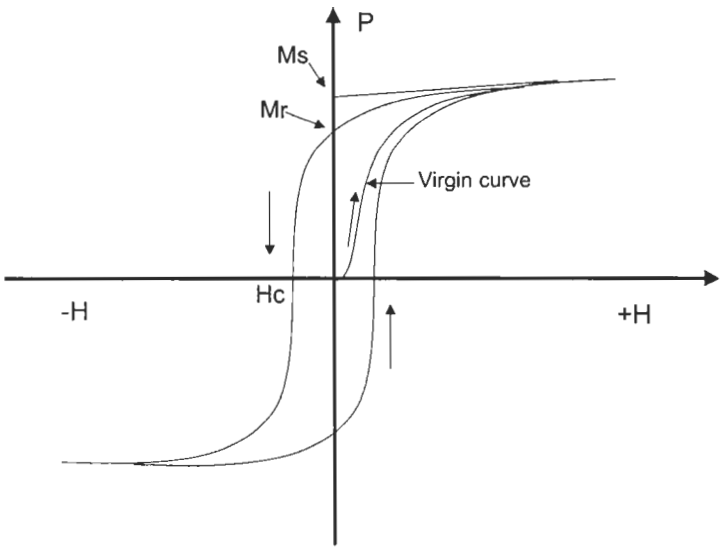

Figure 1.7: Magnetic hysteresis loop.

1.5 Magnetically Ordered Relaxor Ferroelectric Perovskite $Pb(Fe_{2/3}W_{1/3})O_3$ [PFW] and $Pb(Fe_{2/3}W_{1/3})O_3$–$PbTiO_3$ [PFW-PT] Systems

Over the past 20 years, lead-based perovskite $Pb(B'B'')O_3$ relaxor has gained considerable interest and found many applications, such as high-capacitance multilayered capacitors, electrostrictive devices, etc, [30]. This is mainly due to the low sintering temperature, high diffuse dielectric permittivity peak and the possibility to modify these physical and chemical properties [30, 31].

As mentioned previously, the perovskites with relaxor ferroelectric behaviour, like the family of complex composition $A(B'B'')O_3$, where cations B' and B" on the B-site have different valence but a fixed ratio, are characterized by chemical order-disorder on the B-site, giving rise to polar nanostructures. The following are some typical Pb-based relaxor ferroelectric complex perovskite compounds: $Pb(Mg_{1/3}Nb_{2/3})O_3$ [PMN],

$Pb(Zn_{1/3}Nb_{2/3})O_3$ [PZN], $Pb(Sc_{1/2}Nb_{1/2})O_3$ [PSN], $Pb(Sc_{1/2}Ta_{1/2})O_3$ [PST], $Pb(Fe_{2/3}W_{1/3}]O_3$ [PFW], $Pb(In_{1/2}Nb_{1/2})O_3$ [PIN], $(Pb_{1-3x/2}La_x)(Zr_yTi_{1-y})O_3$ [PLZT] and $Pb_{1-x}Ba_xNb_2O_6$ [9, 10, 32-35].

Among them above, PFW is of particular interest, because it exhibits not only relaxor ferroelectric but also magnetic ordering. In PFW perovskite structure with $Pm\bar{3}m$ symmetry, the A-sites are occupied by Pb^{2+} ions and the octahedral B-site positions are filled by Fe^{3+} and W^{6+} ions at random. On the microscopic scale, polar nanoregions (or clusters) are expected to exist due to composition fluctuations and partial order/disorder, which is believed to be the origin of the relaxor ferroelectric behaviour [9-11, 36]. Compared with other relaxors, PFW contains paramagnetic Fe^{3+} ($3d^5$) ions on the B-site with an occupancy of 66.7%, which possibly involves in some magnetic ordering activities upon cooling while the polar nanodomains develop. The magnetic and dipolar interactions in PFW possibly give rise to some peculiar properties in this relaxor.

PFW-containing multicomponent systems may demonstrate superior dielectric/ferroelectric properties compared to the single component PFW system due to significant structural improvements. The binary $Pb(Fe_{2/3}W_{1/3})O_3$ –$PbTiO_3$ [PFW-PT] system is of particular interest [37-42]. PFW is a relaxor ferroelectric and antiferromagnet, while PT is a typical ferroelectric with a sharp maximum of dielectric constant at T_C = 763 K. It is possible to move the Curie temperature to around room temperature and modify the relaxor ferroelectric and magnetic properties by adding an appropriate amount of PT component to the PFW system. Hence, there are relationships among the ferroelectric relaxation, magnetic ordering, perovskite structure, and composition in the (1-x)PFW-xPT systems.

1.6 Previous Studies on the PFW and PFW – PT Systems

1.6.1 Synthesis and Characterization of the $Pb(Fe_{2/3}W_{1/3})O_3$ [PFW] and the $Pb(Fe_{2/3}W_{1/3})O_3$ –$PbTiO_3$ [PFW-PT] Ceramics

Many studies have been performed to improve relaxor ferroelectric properties of PFW for potential applications. These include the preparation of the PFW ceramics with high purity and high density, element-doped PFW, thermal annealing treatment conditions, and forming solid solutions.

Two kinds of high temperature reaction routes were often used for the preparation of PFW ceramics [43-45]. Some other soft chemistry-based routes such as co-precipitation [46] and sol-gel [47] were also tried to synthesize the PFW compound. In a conventional solid state reaction of mixed oxide where all chemicals are directly reacted at high temperature, it is difficult to prepare a monophased PFW compound because of the formation of undesirable, more stable second phases such as $PbWO_4$, Pb_2WO_5 and pyrochlore $Pb_2FeWO_{6.5}$ ($A_2B_2O_7$-type) phase [48-52]. The presence of these second phases with non-ferroelectric properties seriously damages the perovskite microstructure and dielectric properties of the ceramic materials. The other high temperature reaction route is the Columbite method, which was first employed by Swarts and Shrout [44] for the preparation of perovskite $Pb(Mg_{1/3}Nb_{2/3})O_3$ (PMN). In this method, Fe_2O_3 and WO_3 are first reacted together to form Fe_2WO_6 – type structure $B'B''_2O_6$ (not really a columbite phase) by calcinations at high temperature (~1000 ^oC), then followed by the addition of PbO at a second step to form PFW ceramics at the temperatures of 850^o to 900^o [44]. Another name for this method is the B-site precursor method because it

involves the formation of B-site precursor oxides, in which cations prefer to occupy the B-sites of the perovskite structure, followed by a reaction with the A-site species [53]. Therefore, the direct reactions between PbO and WO_3 can in principle be avoided and the subsequent formation of the pyrochlore phase $Pb_2FeWO_{6.5}$ and other side products ($PbWO_4$ and Pb_2WO_5) can be suppressed. The content of the pyrochlore phase in the PFW products can be determined on the basis of X-ray diffraction (XRD) spectrum according to the following formula [54]:

$$\text{Pyrochlore content (\%)} = \{I_{pyro}(222) / [I_{pyro}(222) + I_{perov}(110)]\} \times 100, \qquad (1.6)$$

where $I_{pyro}(222)$ is the intensity of the (222) reflection peak ($2\theta = 29.65^{\circ}$) of the pyrochlore phase and $I_{perov}(110)$ is the intensity of the (110) peak of the perovskite phase. A higher content of perovskite phase (97-98%) can be obtained in the columbite method, compared with ~86% using the conventional mixed oxide method [53, 55]. Improved dielectric properties of PFW were achieved by using the columbite method [43].

As discussed above, it is very difficult to obtain a very pure PFW perovskite by using any synthetic method. Lattice defects always exist in the PFW structure where oxygen vacancies form defect pairs with positively charged defect sites in order to neutralize the charge in the system [56, 57]. In addition, the second phases resulting in non-stoichiometric PFW phase also affect the domain wall motion and the dielectric response leading to ageing. Ageing is a process for a system to evolve from a nonequilibrium state to the equilibrium state [58]. It shows a strong dependence on the frequency and has a log linear function of ageing time. Some authors have investigated the influence of element doping in PFW on the microstructure, dielectric properties, and ageing rate. A certain amount of Mn-doping in PFW ($Pb(Fe_{2/3}W_{1/3})_{1-x}Mn_xO_3$, $x \leq 2$ at%)

was found to control the loss of normal and relaxor ferroelectrics and adjust the magnitude of the dielectric constant and T_{max} by changing its ageing effect [58, 59]. The Mn ions, existing in the form of Mn^{2+} (r = 0.67 Å) or Mn^{3+} (r = 0.58 Å) [60], occupy the B-sites, resulting in the existence of oxygen vacancies in compensation for the charge balance in the perovskite compound. Hence, it provides reorientable dipole pairs that are responsible for the ageing process of Mn-modified PFW ceramics [61]. The Co-doped PFW ($Pb[(Fe_{2/3}W_{1/3})_{1-x}Co_x]O_3$, $x \leq 7.5$ at%) and Cr-doped PFW ($Pb[(Fe_{2/3}W_{1/3})_{1-x}Cr_x]O_3$, $x \leq 5$at%) exhibit a decrease of the dielectric permittivity maximum and the phase transition shifts toward high temperature [62]. It was suggested that both ions incorporated on the B-sites of PFW are compensated by oxygen vacancies, in order to keep the charge balance. Relaxor ageing behavior was observed for both doped compositions.

In addition to the Mn, Co and Cr doping on the B-sites of PFW perovskite structure, some studies on Na or La doping on the A-site of the perovskite, $Pb_{1-x}Na_x[Fe_{(2-x)/3}W_{(1+x)/3}]O_3$ and $Pb_{1-x}La_x[Fe_{(2+x)/3}W_{(1-x)/3}]O_3$ were also reported [63, 64]. It was found that Na^+ (r = 1.02 Å [63]) or La^{3+} (r = 1.32 Å [65, 66]) doping in PFW results in the decrease of the lattice constant of the perovskite structure. The Na-doping significantly improves the ordering of Fe and W cations (~1:1 ratio) on the B sites of the PFW lattice, while La-doping enlarges the difference of Fe^{3+}/W^{6+} ratio in the ordered and disordered regions. After La doping into PFW, the dielectric permittivity maximum decreases and the transition peak broadens, while the corresponding transition temperature, T_m, shifts toward lower temperature. On the other hand, the Na doping does not cause obvious changes in the transition temperature and the dielectric permittivity maximum, which

seems to be in contradiction to the improvement of the ordering of the PFW structure lattice. This may be related to the presence of the non-ferroelectric $PbWO_4$ phase and the mixing of two cations (Na and Pb) on the A sites which may contribute to a certain degree of disorder to counterbalance the increased order on the B sites [64].

The influence of thermal treatments on the relaxor ferroelectric properties of the manganese-doped PFW ceramics was investigated in Refs [67, 68]. Air annealing causes a sharpening of the dielectric permittivity peak and higher permittivity maximum values. Oxygen annealing does not cause evident changes in the dielectric permittivity plot against temperature. The difference is that air annealing can alter the oxygen vacancy equilibrium concentration in the PFW perovskite structure, significantly increasing the possibility of rearranging Fe^{3+} and W^{6+} in B sites. The presence of vacancies favors the diffusion of B cations. It was further suggested that the manganese ions and oxygen vacancies couple to the spontaneous dipoles, enhancing long-range dipolar interaction, thus promoting dipolar order, which accounts for the enhancement of the dielectric maximum value.

In the complex perovskite compound PFW, Fe^{3+} and W^{6+} ions exhibit a disordered occupancy on the B-site. The degree of ordering in PFW can be modified by forming a solid solution with a long-range ordered perovskite compound $PbTiO_3$ [PT]. Partial substitution of Ti^{4+} ions ($r \approx 0.605$ Å [69]) for the Fe^{3+} and W^{6+} ions enhances the related lattice distortion in the perovskite structure, thus modifying the relaxor ferroelectric properties as well. In the binary PFW-PT system, with the PT content increasing, the relaxor ferroelectric may be transformed into a normal ferroelectric phase, accompanied with a structural phase transition from a pseudo-cubic to a tetragonal phase. The

coexistence of multi-phases may take place in a certain composition range. The boundary (or region) of the multi-phases is called the morphotropic phase boundary (MPB) near which the system is expected to exhibit anomalous dielectric properties [40 – 41, 70]. X-ray diffraction results at room temperature demonstrate that the PFW-PT solid solutions with 0 – 20wt% of PT have cubic structure, and those with 30wt% - 100wt% of PT show tetragonal structure [71]. Mitoseriu *et al.* determined a morphotropic phase boundary in the (1-x)PFW-xPT system at 300 K in the range of compositions, $0.20 \leq x \leq 0.37$ [72]. He also investigated the dielectric behavior of (1-x)PFW-xPT with x = 0, 0.2, 0.3 and 0.4 using a modified Landau theory proposed for the ferroelectric relaxor. The temperature dependence of the local order parameter (the average local square polarization $< p_i >^2$) displays the evolution of the system from short-range order (SRO) to long-range order (LRO) ferroelectric, with the increasing PT component. However, the anomaly related to MPB was not observed on the temperature dependence of the dielectric constant of (1-x)PFW-xPT [73, 74]. The microstructural evolution of 0.68PFW-0.32PT ceramics was analyzed using *in situ* TEM over the temperature range of 16 to 300 K [75]. At 16 K, all grains show a macrodomain structure throughout their volume, but at T>250 K a domain-free shell is formed around the central core that still exhibits strong domain wall. EDS (Energy Dispersive X-ray Spectrometer) analysis revealed that the cores were Ti-rich and the shells are W-rich with respect to the bulk composition. So far, systematic and detailed studies of the PFW-PT system in terms of component (structure) and dielectric properties are still lacking.

1.6.2 Relaxor Ferroelectric PFW Single Crystal

While almost all of the chemical and physical characterizations have been carried out on PFW and PFW-PT polycrystalline ceramic systems, single crystals of PFW and PFW-PT are expected to display superior dielectric properties to polycrystalline PFW ceramics when appropriate crystallographic directions are chosen for the measurements. This is because single crystals usually show a perfect and continuous structure without any heterogeneous phases due to the presence of grain boundaries. Unfortunately, the growth of PFW and PFW-PT single crystals has encountered some difficulties arising from the control of the thermal and chemical parameters of multi-component systems and from the volatility of the solvents at high temperatures [76, 77]. Recently, Ye *et al.* successfully synthesized single crystals of PFW from a high temperature solution growth using ($PbO + B_2O_3$) as flux [14, 38]. The grown small crystals (~ 1.0 x 1.0 x 1.0 mm^3) exhibited a regular cubic morphology, black and semi-metallic luster, and a good optical isotropy, without inclusions or internal stress. The structural analysis of the single crystal by X-ray diffraction shows that it has an average primitive cubic perovskite structure with *Pm3m* symmetry. The structural refinement demonstrates a positional disorder due to shifts of atoms (Pb, Fe and W) from their ideal positions. Hence, a disordered structural model was presented for PFW. It was found that at zero electric field the PFW crystals remain optically isotropic down to 10 K, and show typical relaxor ferroelectric behaviour in the temperature dependence of the dielectric permittivity. A macroscopically polar phase can be induced by the application of an electric field and remain metastable when the field is removed at low temperature. Under an alternating electric field, the induced polarization gave rise to dielectric hysteresis loops showing

ferroelectric behaviour at low temperature below 80 K. However, no PFW-PT single crystals have been successfully grown and reported so far.

1.6.3 Magnetic Properties of Perovskite Compounds PFW and (1-x)PFW-xPT

Besides relaxor ferroelectric properties, PFW is also believed to be a "ferroelectric antiferromagnetic" material, because of an antiferromagnetic ordering taking place below the Néel temperature, T_N = 363 K. Above T_N, the temperature dependence of the magnetic susceptibility $\chi = C/(T-\theta)$ is satisfied [78, 79]. In the PFW perovskite structure, the paramagnetic ions Fe^{3+} ($3d^5$) are located on the octahedral B-sites with an occupancy of 66.7%. Magnetic ordering may occur upon cooling as the polar nanodomains form and develop. Earlier studies found that the antiferromagnetic order of PFW ceramics takes place in the temperature range of 363 K ~ 383 K on the temperature dependence of magnetization [78, 80, 81]. Later, Al'shin *et al.* [82] claimed that there are two Curie-Weiss regions below T_N = 383 K, on the basis that the antiferromagnetic ordering and a small spontaneous magnetic moment occur at low temperatures. Mössbauer spectroscopy measurements of PFW indicated that one magnetic ordering should occur in the magnetic sublattice I below 415 K and the other in the magnetic sublattice II below 383 K. [83]. Clearly, there is inconsistency in an agreement on the results of magnetic measurements of the PFW ceramics.

In a recent study of the PFW single crystal, Ye *et al.* observed two types of antiferromagnetic phase transitions in the temperature dependence of the magnetization at T_{N1} = 350 K and T_{N2} = 20 K, respectively, as shown in Fig. 1.8 [14]. They proposed that these antiferromagnetic orders arise from two different types of interaction, one from a

superexchange in the Fe/W disordered nanoregions through a – Fe^{3+}– O^{2-} – Fe^{3+} – pathway below 350 K, and the other from the superexchange of – Fe^{3+} – O^{2-} – W^{6+} – O^{2-} – Fe^{3+}– pathway in the Fe/W ordered nanoregions below 20 K. The unusual ordered/disordered microstructure features are believed to give rise to the intriguing magnetic ordering behaviour in the PFW perovskite compound.

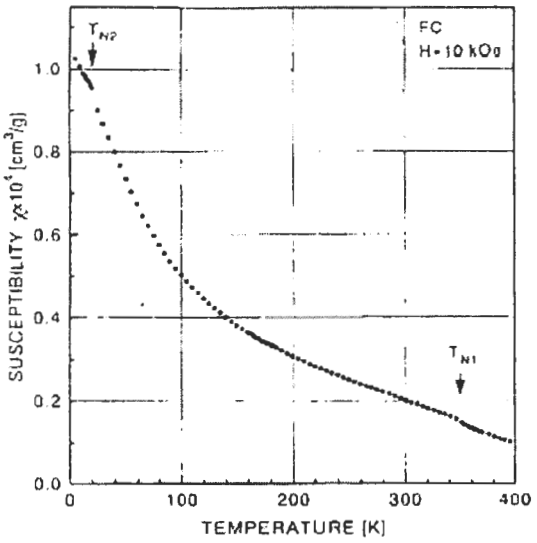

Figure 1.8: Temperature dependence of the magnetic susceptibility (χ) of the PFW single crystal measured by SQUID at H = 10 kOe (//<100>$_{cub}$ after field cooling [14].

The influence of the perovskite structural order/disorder on the magnetic order of PFW was recently discussed in the ceramics of (1-x)PFW-xPT ($0 \leq x \leq 0.50$) solid solution [84, 85]. Two types of antiferromagnetic ordering transitions were found when the PT content is small ($x \leq 0.25$). With the amount of PT component increasing, or with the transition from short-range ordered relaxor to long-range ordered ferroelectric, the

low-temperature antiferromagnetic Néel point shifts toward a higher temperature and the high-temperature one shifts toward a lower temperature. Unfortunately, no detailed explanation was provided of the shift of the low-temperature Néel transition towards higher temperature. The induced magnetization of the PFW ceramics was also investigated under an alternating electric field. At the temperatures below the low-temperature Néel transition, a very slim hysteresis loop was obtained, suggesting a weak ferromagnetism in the material [84].

1.6.4 Magnetoelectric Effect in the Multiferroic PFW and PFW-PT Systems

Magnetism and ferroelectricity involve local spins and off-centre structural distortions, respectively. These two kinds of interactions can coexist in some particular materials, termed multiferroics, or magnetoelectrics [86-88]. Since some substances possess simultaneous electric and magnetic dipole moments, the applied electric (magnetic) fields may induce not only electric (magnetic) polarization, but also magnetic (electric) polarization [89, 90]. First-principle calculations proved that the magnetoelectric effect is caused due to the role of the d electrons of the transition metals associated with their magnetic properties, which tends to reduce the off-centre ferroelectric distortion [91]. Therefore, the ferroelectric (magnetic) transition is probably influenced by the magnetic (ferroelectric) behavior. The magnetoelectric effect has been observed in many multiferroics, such as the perovskite $BiFeO_3$ [92] and $BiMnO_3$ [90], the boracite family [93], and $RMnO_3$ (R= rare earth) [94].

The magnetoelectric phenomenon in PFW single crystal was first reported by Ye *et al.* [14]. A slight deviation of the magnetization from linearity in the temperature

interval of the dielectric relaxation around T_m = 175 K is possibly a sign of magnetoelectric coupling within the perovskite compound (Fig. 1.8). The slowing down in the dynamics of the polar clusters, which was considered to be the origin of the dispersive dielectric peak in relaxor ferroelectrics, seems to interrupt the magnetic interaction. Mitoseriu *et al.* [84] discussed the magnetoelectric effect based on the fact that an anomaly of the magnetic hysteresis loop observed at the phase transition temperature 175 K in the PFW ceramics, as shown in Fig. 1.9. However, it is difficult to detect an obvious magnetoelectric interaction. The complete (non-reversible) rotation of the ferroelectric domains by an applied magnetic field is rarely observed. The theoretical study of the coupling mechanism between antiferromagnetic and ferroelectric ordering based on the soft-mode theory for a ferroelectric system and the mean-field approximation for the magnetic subsystem [95] indicated that the Néel temperature would decrease with decreasing magnetoelectric coupling. Thus, in the (1-x)PFW-xPT system, the maximum magnetoelectric coupling seems to occur in pure PFW. Generally speaking, the magnetoelectric effects observed in the experiments of temperature and magnetic field dependence of magnetization are very weak in PFW and PFW-PT systems. It is also necessary to clarify by means of other magnetic or dielectric measurement techniques.

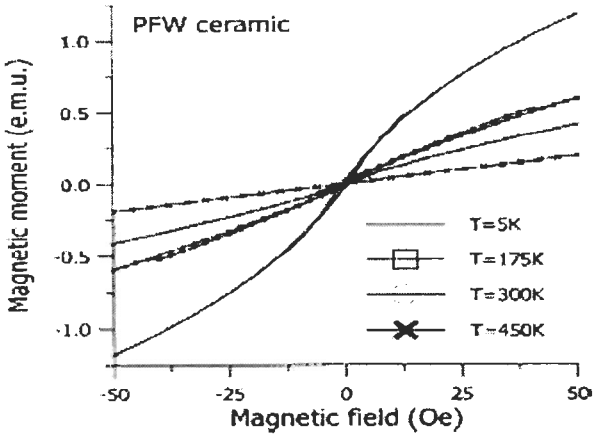

Figure 1.9: Magnetic hysteresis loops of the PFW ceramics at different temperatures [84].

1.7 Objectives and Plans of This Work

Some fundamental studies on the ferroelectric and magnetic properties of the PFW and PFW-PT ceramics systems have been carried out, although some results are not in agreement with each other. Generally speaking, systematic and detailed studies of the PFW-PT ceramic and single crystal systems in terms of phase (structure) transitions, dielectric, relaxor ferroelectric, and magnetic properties are still not reported. Such studies will be useful in order to reveal the intrinsic relationships among composition, structure, relaxor ferroelectric and magnetic properties of this system.

The plan of this work is to synthesize the (1-x)PFW-xPT solid solution system in the focus on ceramics and single crystals, and to characterize the structural, dielectric, relaxor ferroelectric, and magnetic properties, in order to provide a better understanding of the structure-property relations of this magnetically ordered relaxor ferroeletric system. It is composed of the following parts.

(1) Synthesis, Structure and Properties of the (1-x)PFW-xPT Solid Solution Ceramics

A modified B-site precursor method is developed to synthesize highly pure perovskite phase of (1-x)PFW-xPT, with x = 0, 0.10, 0.20, 0.25, 0.30, 0.325, 0.35, 0.40, 0.60, and 0.80. The phase and structure are characterized by X-ray diffraction.

The dielectric/ferroelectric properties and the phase transitions will be examined by means of dielectric measurements and differential scanning calorimetry (DSC) analysis. A ferroelectric phase diagram of the solid solution system is established, which describes the perovskite phase as a function of composition and temperature. A morphotropic phase boundary (MPB) is located within a certain composition interval, which separates a pseudocubic (rhombohedral) phase from a tetragonal phase. The relaxor ferroelectric behavior of (1-x)PFW-xPT systems will be investigated as a function of frequency, temperature, and perovskite structural ordering (or composition).

(2) AC Impedance Spectroscopic Analysis of the Electrical Microstructural Phases in the (1-x)PFW-xPT Ceramics

It is known that polycrystalline ceramics materials contain different microstructural phase components. Each phase component makes individual contribution to the total electric response of the system. The electrical transport properties of microstructure phases in the (1-x)PFW-xPT polycrystalline system will be studied with the help of complex ac impedance spectroscopic measurements combined with electric modulus formalism analysis. The resistivity, electric modulus, and capacitance of the microstructure phases, are measured and analyzed as functions of temperature and

frequency. More importantly, the influence of each microstructural component phase on the ferroelectric behaviour of the (1-x)PFW-xPT ceramics system will be discussed.

(3) Growth and Characterization of the (1-x)PFW-xPT Single Crystals

Single crystals of the (1-x)PFW-xPT solid solution, with x = 0, 0.07, 0.13, 0.17, 0.27, and 0.75, are grown from high temperature solution using PbO as flux. The dielectric measurements are carried out as a function of temperature and frequency. The relaxor ferroelectric mechanism is further analyzed with the help of the dispersive dielectric relaxation models. In addition, the dependence of the macroscopic polarization of relaxor ferroelectrics on the external applied electric field will also be investigated.

(4) Magnetic Properties of the (1-x)PFW-xPT Single Crystals

The magnetic properties of the (1-x)PFW-xPT single crystals are investigated by measuring the temperature and magnetic field dependences of the magnetization. The macroscopic magnetization by the application of a magnetic field is studied, which further reveals the different magnetic interactions at various temperatures. The variation of the magnetic interaction behaviour with the perovskite microstructure and composition will be discussed to understand of the experimental results obtained in the PFW-PT system.

(5) Mössbauer Spectroscopic Measurements of the PFW and 0.75PFW – 0.25PT Ceramics

The magnetic properties and hyperfine interactions in the ^{57}Fe-enriched PFW and 0.75PFW-0.25PT ceramics are studied by means of the Mössbauer spectroscopic

measurements. The magnetic interaction between the magnetic moment of the nucleus and the internal magnetic field arising from the ceramic materials at different temperatures is discussed. The influence of the PT-component on the Mössbauer spectra of PFW-PT is also further discussed.

(6) General Summary

Finally, a general summary is given on this magnetically ordered relaxor ferroelectric (1-x)PFW-xPT system.

1.8 References

[1] T. Mitsui, I. Tatsuzaki and E. Nakamura, *An introduction to the physics of ferroelectrics*, Gordon and Breach Science Publishers, New York (1976).

[2] R. E. Eitel, *Ph. D thesis in materials science and engineering*, Pennsylvania State University (2003).

[3] F. Jona & G. Shirane, *Ferroelectric Crystals*, Dover Publication Inc., New York (1993).

[4] L. E. Cross and K. H. Härdtl, *Encyclopedia of Chemical Technology* **10**, 1 (1980).

[5] W. J. Merz, *Phys. Rev.*, **91**, 513 (1953).

[6] M. E. Line and A. M. Glass, *Principles and Applications of Ferroelectrics and Related Materials*, Clarendon Press, Oxford (1977).

[7] G. Shirane and S. Hoshino, *J. phys. Soc. Jpn.* **6**, 265 (1951).

[8] A. R. West, *Basic Solid State Chemistry*, John Wiley & Sons, Ltd., Chichester

(1996).

[9] L. E. Cross, *Ferroelectrics* **151**, 305 (1994).

[10] Z.-G. Ye, *Key Eng. Mater.* **155 – 156**, 81 (1998).

[11] L. E. Cross, *Ferroelectrics* **76**, 241 (1987).

[12] A. Verbaere, Y. Piffard, Z.-G. Ye and E. Husson, *Mat. Res. Bull.* **27**, 1227 (1992).

[13] A. Geddo Lehmann, F. Kubel, Z.-G. Ye and H. Schmid, *Ferroelectrics* **172**, 277 (1995).

[14] Z.-G. Ye, K. Toda, M. Sato, E. Kita and H. Schmid, *J. Korean Phys. Soc.* **32**, S1028 (1998).

[15] C. A. Randall and A. S. Bahlla, Jpn. *J. Appl. Phys.* **29**, 327 (1990).

[16] C. A. Randall and A. S. Bahlla, T. R. Shrout and L. E. Cross, *J. Mater. Res.* **5**, 829 (1990).

[17] G. A. Smolenskii, *J. Phys. Soc. Japan* **28**, 26 (1970).

[18] G. A. Smilenskii, V. A. Isupov, A. I. Agranovskaya and S. N. Popov, *Soviet Phys. –Solid State* **2**, 2584 (1961).

[19] D. Viehland, S. J. Jang, and L. E. Cross, *J. Appl. Phys.* **68,** 2916 (1990).

[20] U. T. Höchli, K. Knorr and A. Loidl, *Adv. Phys.* **39.** 405 (1990).

[21] V. Westphal, W. Kleemann and M. D. Glinchuk, *Phys. Rev. Lett.* **68**, 847 (1992).

[22] W. Kleemann and A. Klössner, *Ferroelectrics* **150**, 35 (1993).

[23] L. A. Bursill, H. Qian, J.-L. Peng and X.-D Fan, *Physica B*, **216**, 1(1995).

[24] A. A. Bokov and Z.-G. Ye, *J. Phys.; Condens. Matter* **12**, L541 (2000).

[25] A. A. Bokov and Z.-G. Ye, *Phys. Rev. B.* **65**, 144112 (2002).

[26] A. A. Bokov and Z.-G. Ye, *Phys. Rev.* B **66**, 064103 (2002).

[27] R. Pirc and R. Blinc, *Phys. Rev.* B **60**, 13470 (1999).

[28] C. N. R. Rao, *Solid State Chemistry*, Marcel Dekker, Inc. New York, (1974).

[29] F. Fiorillo, *Measurement and Characterization of Magnetic Materials*, Elsevier Academic Press, Amsterdam, (2004).

[30] T. R. Shrout and A. Halliyal, *Am. Ceram. Soc. Bull.* **66** (4), 704 (1987).

[31] G. H. Haerlling, *J. Am. Ceram. Soc.* **82**(4) 797 (1990)

[32] C. G. F. Stenger, F. L. Scholten and A. J. Burggraaf, *Solid State Common* **32**, 989 (1979).

[33] N. Setter and L. E. Cross, *J. Mater. Sci.*, **15**, 2478 (1980).

[34] F. Chu, I. M. Reaney and N. Setter, *Ferroelectrics* **151**, 343 (1995).

[35] J. Chen, H. M. Chan, and M. P. Harmer, *J. Am. Ceram. Soc.* **72**, 593 (1989).

[36] Z.-G. Ye, *Ferroelectrics* **184**, 193 (1996).

[37] L. Feng and Z.-G. Ye, *J. Solid State Chem.* **163**, 484 (2002).

[38] Y. –J. Kim and S.-W. Choi, *Ferroelectrics* **186**, 287 (1996).

[39] M. Yonezawa, *Am. Ceram. Soc. Bull.* **62**, 1375 (1983).

[40] V. V. Gagulin, S. K. Korchagina, Y. A. Shevchuk, N. V. Fadeeva and V. V. Bogatko, *Ferroelectrics* **204,** 345 (1997).

[41] L. Mitoseriu, A. Stancu, C. Fedor and P. M. Vilarinho, *J. Appl. Phys.* **94**, 1918 (2003).

[42] L. Mitoseriu, P. M. Vilarinho, M. Viviani and J. L. Baptista, *Mater. Lett.* **57**, 609 (2003).

[43] L. Zhou, P. M. Vilarinho, J. L. Baptista, *Mater. Res. Bull.* **29**, 11, 1193 (1994).

[44] S. L. Swartz, T. R. Shrout, *Mater. Res. Bull.* **17**, 1245 (1982).

[45] A. S. Khim, J. Wang and J. Xue, *Solid State Ionics* **132**, 55 (2000).

[46] C. H. Lu, Y. C. Wong, *Ceram, Int.* **21**, 413 (1995).

[47] C. H. Lu, K. Shinozaki, N. Mitzutani, *J. Am. Ceram. Soc.* **75,** 1303 (1992).

[48] G. A. Smolenskii, A. I. Agranovskaya, V. A. Isupov, *Sov. Phys. Sol. State* **1**, 907 (1959).

[49] C. H. Lu, N. Ishizawa, K. Shinozaki, N. Mizutani, M. Kato, *J. Mat. Sci. Lett.* **7**, 1078 (1988).

[50] P. M. Vilarinho, J. L. Baptista, *J. Europ. Ceram. Soc.* **11**, 407 (1993).

[51] A. I. Agraanovskaya, Bull. *Acad. Sci. USSR Phys. Ser.* 1271 (1960).

[52] M. P. Kassarjian, R. E. Newnham and J. V. Bigger. *Amer. Ceram. Soc. Bull.* **64**, 1108 (1985).

[53] B.-H. Lee, N.-K. Kim, B.-O. Park and S.-H. Cho, *Mater. Lett.* **33**, 57 (1997).

[54] G. Drazic, M. Trontelj, and D. Kolar, *Mater. Sci. Eng.* B **26**, 189 (1994).

[55] L. Zhong *Mater. Res. Bull.* **1**,193 [1994].

[56] W. Y. Pau, T. R. Shrout and L. E. Cross, *J. Mater. Sci. Lett.* **8**, 771 (1989).

[57] G. Drazic, H. Trontelj and D. Kolar, *Mater. Sci. Eng.* B **26**, 189 (1994).

[58] R. Natarajan, J. P. Dougherty, *J. Mater. Sci.* **33**, 1991 (1998).

[59] Q. M. Zhang, J. Zhao and L. E. Cross, *J. Appl. Phys.* **79**, 1 (1996).

[60] X. Wang and X. Yao, *Ferroelectric* **154**, 307 (1994).

[61] L. Zhou, P. M. Vilarinho, and J. L. Baptista, *Mater. Res. Bulletin* **31**, No. 6, 699 (1996).

[62] C. Miranda, P. M. Vilarinho and L. Zhou, *Ferroelectrics* **233**, 269 (1999).

[63] L. Zhou, P. M. Vilarinho and J. L. Baptista, *J. European Ceram Soc.* **18**, 1383 (1998).

[64] L. Zhou, P. M. Vilarinho and J. L. Baptista, *Key. Engng. Mater.* Vol. **132**, 1080 (1997).

[65] L. Zhou, P. M. Vilarinho, P. Q. Mantas, J. L. Baptista, and E. Fortunato, *J. European Ceramic Soc.* **20,** 1033 (2000).

[66] R. D. Shannon and C. T. Prewitt, , *Acta. Cryst.* B **26**, 1046 (1970).

[67] P. M. Vilarinho, Ph. D thesis, Aveiro University, Portugal, (1994).

[68] L. Zhou, P. M. Vilarinho and J. L. Baptista, *J. Mater. Sci.* **33,** 2673 (1998).

[69] R. D. Shannon, *Acta. Crystallogr*, **A32** 751 (1976).

[70] B. Jaffe, W. R. Cook, and H. Jaff, *Piezoelectric Ceramics*, Academic Press, London (1971).

[71] T. S. Shrout, Z. P. Chang, N. Kim, and S. Markgraf, *Ferroelectrics Lett.* **12**, 63 (1990).

[72] V. J. Tennery, K. W. Hang and R. E. Novak; *J. Am. Ceram. Soc.* **51**, 671 (1968).

[73] L. Mitoseriu. M. M. Carnasciali, P. Piaggio, P. Nani, *Appl. Phys. Lett.* **81**, 5006 (2002).

[74] L. Mitoseriu, A. Stancu and C. E. Fedor, *J. Opt. and Adv. Mater.* Vol. **5**, 3, 787 (2003).

[75] Z. Li, A. Wu, P. M. Vilarinho and I. M. Reaney, *J. Phys.: Condens. Mater* **17**, 2167 (2005).

[76] Z.-G. Ye and H. Schmid, *Ferroelectrics* **162**, 119 (1994).

[77] D. Elwell and H. J. Sheel, *Crystal Growth from High Temperatue solution,* Academic Press, New York, (1975).

[78] G. A. Smolenskii and A. F. Ioffe, in "*Colloque International de magnetisme de Grenoble*", 71 (1958).

[79] V. A. Bokov, I. E. Myl'nikova and G. A. Smolenskii, *Soviet phys.-JETP* **15**, 447 (1962).

[80] G. A. Smolenskii and V. a. Bokov, *J. Appl. Phys*. **35**, 915 (1964).

[81] V. A. Bokov, I. E. Myl'nikova, and G. A. Smolenskii, *Ferroelectrics-Antiferomagnets, Zh. Eksp. Teor. Fiz*. Vol. **42** (2), 643 (1962).

[82] V. I. Al'shin, *Investigation of Magnetoelectric Interactions in magnetically Ordered Crystals, Cand. Sci. (phys.-math.) Dissertation*, Leningrad: Inst. Of Semiconductors, USSR Acad. Sci., (1970).

[83] Yu. N. Venevtsev, V. V. Sklyarevskii, I. I. Lukashevich, *Kristallografiya*, Vol. **21** (5), 971 (1976).

[84] L. Mitoseriu, D. Marré, A. S. Siri and P. Nanni, *Appl. Phys. Lett*., Vol. **83** (26), 5509 (2003).

[85] L. Mitoseriu, D. Marré, A. S. Siri, A. Stancu, C. E. Fedor and P. Nanni, *J. Opt. and Adv. Mater*. Vol. **6** (2), 723 (2004).

[86] G. A. Smolenskii and I. E. Chupis, *Ferroelectromagnets*. Usp. Fiz. Nauk. **137**, 415 (1982).

[87] H. Schmid, *Ferroelectrics* **162**, 317 (1994).

[88] J. Wang, J. B. Neaton, H. Zheng, V. Nagarajan, S. B. Ogale, B. Liu, D. Viehland, V. Vaithyanathan, D. G. Schlom, U. V. Waghmare, N. A. Spaldin, K. M. Rabe, M.

Wuttig, R. Ramesh. *Science* **299**, 1719 (2003).

[89] S. A. Boguslavskii, Izbrannye Trudy po Fizike, Moscow: *Fizmatgiz* **231** (1961).

[90] T Kimura, S Kawamoto, I Yamada, M Azuma, M TakanoT . *Phys. Rev.* B **67**, 180401 (2003).

[91] N. A. Hill, K. M. Rabe, *Phys. Rev.* B **59**, 8759 (1999).

[92] G. A. Smolenskii, V. M. Yudin, E. S. Sher and Yu. E. Stolypin, *Sov. Phys, JETP* **16**, 622 (1963).

[93] E. Ascher, H. Rieder, H. Schmid and H. Stössel, *J. Appl. Phys.* **37**, 1404 (1966).

[94] T. Katsufuji, *Phys. Rev.* B **64**, 104419 (2001).

[95] C. G. Zhong and Q. Jiang, *J. Phys.: Condens. Matter* **14**, 8605 (2002).

Chapter 2:
Experimental and Principles

2.1 Introduction

In this chapter, the experimental methods and the basic principles that are used in this thesis work are introduced. The main experimental methods include X-ray diffraction for structure and phase characterization, AC impedance spectroscopy for dielectric, electrical conductivity and resistivity measurements, Sawyer-Tower circuit for dielectric hysteresis measurement, differential scanning calorimetry (DSC) for thermal analysis and phase transition, superconducting quantum interferometric device (SQUID) magnetometer for magnetic measurements, and Mössbauer spectroscopy for magnetic properties studies.

2.2 X-ray Diffraction (XRD) for Crystal Structure Characterization

Different crystal structures (d-spacing, Bragg angle and atomic numbers) have distinct X-ray diffraction patterns (angles and intensities of the reflection peaks). Therefore, the "fingerprint" feature of the X-ray diffraction pattern has been used widely for the identification of crystalline materials [1].

Single crystals are built up of regular arrangements of atoms in three dimensions. These arrangements can be represented by repeatable unit cell with six parameters. They are three unit cell edges a, b, c, and three angles α (between b and c), β (between a and c), γ (between a and b) [2]. When a crystal structure changes, for example from cubic ($a = b = c$ and $\alpha = \beta = \gamma = 90°$) to tetragonal ($a = b \neq c$ and $\alpha = \beta = \gamma = 90°$) structure, the X-

ray diffraction pattern also changes, as shown in Fig. 2.1. The 200 reflection peaks in cubic structure split into the (002) and (200)/(020) peaks in tetragonal structure, and the (220) reflection peak splits into the (202)/(022) and (220) peaks, because the lengths of the unit cell edges are no longer equal after the structure symmetry change. All (111) reflections in the tetragonal structure are identical and display only one peak (Fig. 2.1(b)). Based on this principle, the phase symmetry and phase components of the (1-x)PFW-xPT solid solution can be characterized in this work, especially for the compositions near the morphotropic phase boundary where multiple phases coexist.

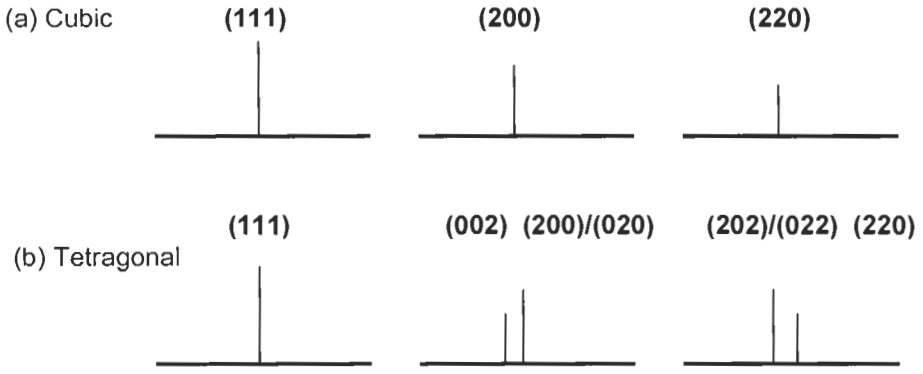

Figure 2.1: Characteristic X-ray spectrum for (a) Cubic (prototype) and (b) Tetragonal. The corresponding splitting is shown as the crystal structure changes from cubic to tetragonal phase.

2.2.1 XRD Instruments Used in Our Work

Two types of X-ray diffraction apparatus were used for the structural analysis of the ceramics and single crystals. One is Philips PW 1730 X-ray diffractometer. The resolution of angle 2θ scanning is usually ≥ 0.02°. The maximum current and voltage used are 40 mA and 45 kV, respectively. The R-AXIS RAPID X-ray diffractometer is

made by Rigaku International Corporation. This apparatus is capable of rapidly collecting (usually less than 30 min.) the diffraction pattern of low-molecular single crystal. It is mainly composed of three sections: main body, X-ray generator, and host computer sections. The maximum operation current and voltage are 50 mA and 45 kV, respectively.

2.3 Dielectric Spectroscopy

2.3.1 Simple Principles of Dielectric Constant Measurements

Dielectric materials ideally have zero electrical (ionic) conductivity and are used as capacitors and electrical insulators in a variety of applications. When a potential difference is applied to the dielectric electrodes of a parallel capacitor, a polarization of charge arises, although long-range motion of ions or electrons should not occur. The capacitance (C) of a dielectric substance can be expressed by

$$C = \varepsilon_r \varepsilon_o (A/d) , \qquad (2.1)$$

where ε_o is the permittivity of free space, 8.854×10^{-12} F m^{-1}, ε_r is the dielectric constant (or relative real permittivity), A is the area of plates of the parallel capacitor, and d is the thickness of the capacitor [3, 4].

In a real dielectric constant measurement, an alternating electromotive force Φ with frequency f is applied to the electrodes of a parallel capacitor structure, and an alternating magnitude of current, i, can be written in the following form

$$i = jf\varepsilon_r C_o \Phi \qquad (2.2)$$

where $j = \sqrt{-1}$, $C_o = \varepsilon_o A/d$ is the vacuum capacitance of the space cell with electrode area (A). Because of the existence of dielectric loss (including the leakage current) in dielectric materials, the dielectric constant ε_r has to be written in a complex form:

$$\varepsilon_r^*(f) = \varepsilon'(f) - j\varepsilon''(f) \quad , \tag{2.3}$$

where ε' is the real part of the dielectric permittivity (usually called dielectric constant) and ε'' the imaginary part of the dielectric permittivity. The ratio of imaginary part to real part of the dielectric permittivity represents the dielectric loss. In a complex coordinate system, it is equal to

$$\tan \delta = \varepsilon''/\varepsilon' \quad , \tag{2.4}$$

where $\tan \delta$ is the tangent of the dielectric loss angle.

2.3.2 AC Impedance Analyzer and Broadband Dielectric Spectrometer

The measurements of the dielectric permittivity as a function of temperature at different frequencies were carried out using a Solartron impedance analyzer associated with a Solartron 1296 dielectric interface or using an Alpha high-resolution dielectric/impedance analyzer (NovoControl), as shown in Fig.2.2. A wide frequency range of 1 Hz to 1000 kHz is often applied for the dielectric measurements. The experiments are carried out upon heating in the temperature range of 100 K to 700 K.

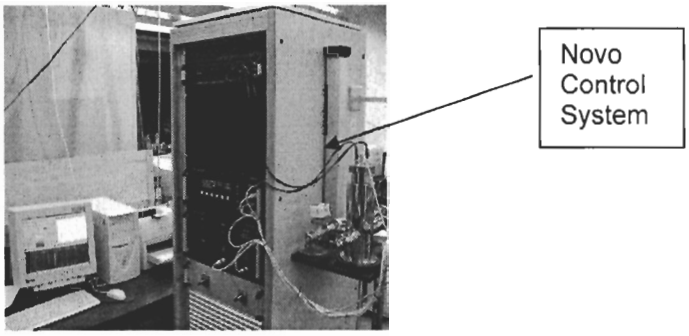

Figure 2.2: Alpha high-resolution broadband dielectric/impedance spectrometer (NovoControl)

The dielectric and impedance spectroscopy was employed in this work to characterize the dielectric properties, relaxor ferroelectric behaviour and the electrical microstructure of the (1-x)PFW-xPT solid solution ceramics and single crystals.

2.4 Ferroelectric Hysteresis Loop Measurements

The induced polarization under the application of an electric field can be investigated with the help of ferroelectric hysteresis loop measurements in which the electric field dependence of the polarization of a dielectric substance is obtained. When such a hysteresis loop is observable, the dielectric substance shows ferroelectricity, because the macroscopic polarization occurs and some residual electrical polarization is retained after an applied electric field is switched off in the system, as explained in section 1.1.

2.4.1 Sawyer-Tower Circuit for Ferroelectric Hysteresis Loop Measurements

In order to measure the polarization as a function of electric field, a RT66A standard ferroelectric testing system (Radiant Tech.) combined with RT66A high voltage interface (HVI) was used based on the principle of Sawyer-Tower circuit that is a typical ferroelectric measurement method [4]. Figure 2.3a is a photograph of the test set-up with the HVI connected and Fig. 2.3b is a modified Sawyer – Tower circuit describing the principle of measurement [5, 6]. An alternating voltage V is applied on a dielectric sample with capacitance C_x and resistance R_x. If the thickness of a sample is d, an electric field gradient can be expressed in terms of E = V/d, which is often used in the measurements of induced polarization of the dielectric substance. An RC circuit is connected in series with the sample C_x in the circuit. The parallel RC circuit allows compensation for any phase shift due to conductivity or dielectric loss in the sample. Two capacitors in the circuit are connected in series. Therefore, the voltage V_r across C_r is proportional to the charge (Q) of the sample C_x by

$$V_r = Q/C_r = (A/C_r)P \propto P \quad , \tag{2.5}$$

here A is the electrode area of a sample and P is the polarization of the sample. The voltage is monitored and converted into the polarization of the sample. The polarization (or electric displacement) plot against electric field applied is displayed on a typical RT66A software data screen.

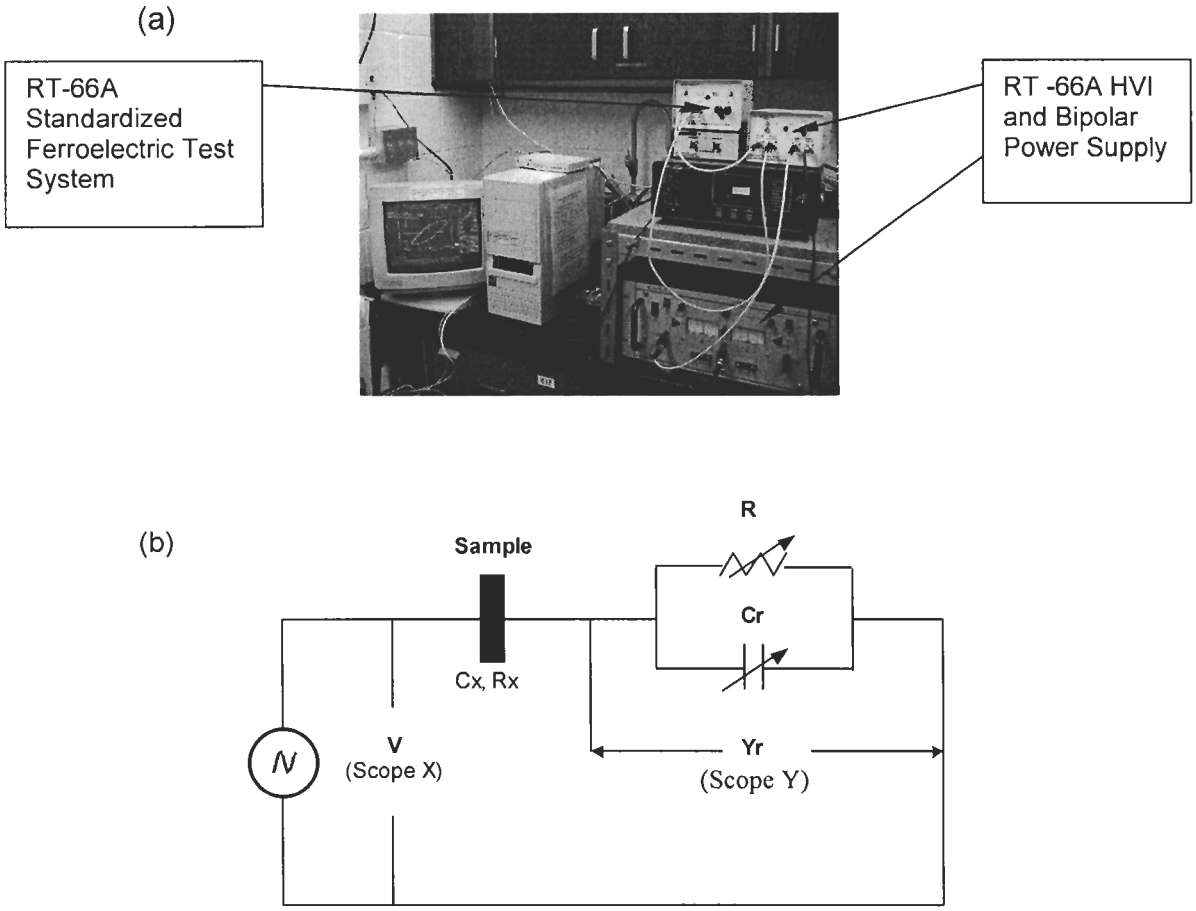

Figure 2.3: (a) RT66A standard ferroelectric testing system (Radiant Tech.), (b) A modified Sawyer-Tower circuit for the measurement of ferroelectric hysteresis loops [5].

The dielectric hysteresis loop measurements are carried out in this work to characterize the ferroelectricity of the (1-x)PFW-xPT single crystals.

2.5 Differential Scanning Calorimetry (DSC)

In order to analyze and confirm the structural phase transition in the (1-x)PFW-xPT solid solution system, the temperature dependence of heat flow is measured using the differential scanning calorimeter (DSC) technique in this work.

Figure 2.4 is a schematic setup of the DSC measurement system (DSC6200, Seiko Exstar [7]) used in our experiments. The specimen and the reference in different alumina pans are placed on top of the sample and reference holder, respectively. The weights of crushed ceramic specimen and α-alumina powder reference are 30~40 mg and 20 ~ 30 mg, respectively, for an approximate heat capacity balance between them. The reference sample has to have a constant thermal change in the experimental temperature range in order to have a stable reference baseline [8].

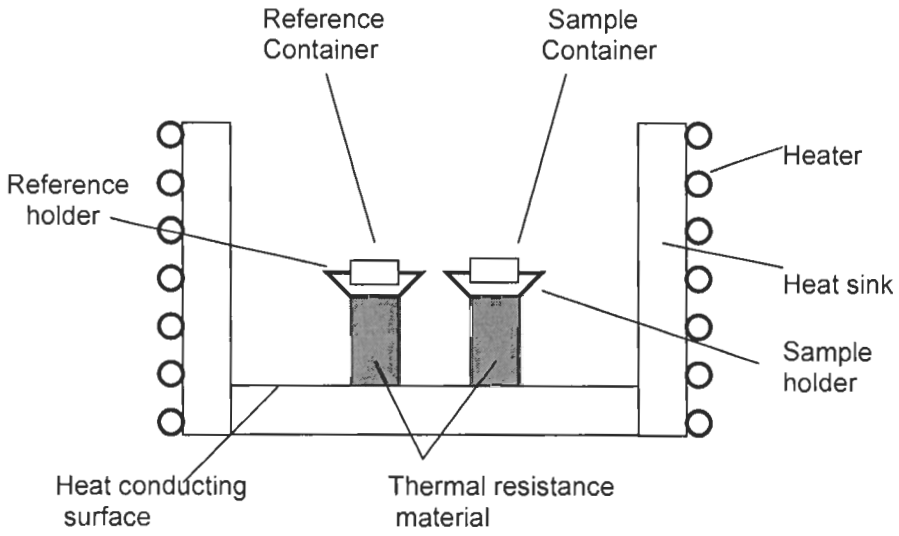

Figure 2.4: DSC measurement setup

For the DSC6200 module, the measurement temperature range is –150 °C to 725 °C and the thermal detection range is ±100 μW ~ ±100 mW. Hence, in most cases, the heat flow in a solid-state phase transition or a chemical reaction is usually detected by the DSC6200 unit.

2.6 Magnetic Measurements

2.6.1 Basic Magnetic Measurement Principle

When a sample with magnetic properties moves through the metal coils under the condition of magnetic field, the magnetic flux density (or magnetic induction) B within the metal coil will be changed because of the variation of magnetic moment of the sample and obeys the following equation [9, 10]:

$$B = H + 4\pi M \quad , \tag{2.6}$$

where H is the applied magnetic field (Oe), and M is the magnetization of the sample (emu/g, or emu/mole).

The ratio of M over H is called the magnetic susceptibility χ (emu/g /Oe),

$$\chi = M / H \quad . \tag{2.8}$$

which is often plotted against temperature for the studies of magnetization properties of the sample. The dia-, para-, or antiferromagnetic substances usually have constant susceptibility χ under normal condition, such as magnitude of magnetic field, and retain no magnetism when the field is removed. However, the ferromagnetic substance is quite different (see section 1.4)

2.6.2 Magnetic Measurement by a Superconducting Quantum Interference Device (SQUID) [10]

The magnetic moment of a sample is measured by moving the sample through the detection coil in a series of steps. At each step, the sample's magnetic moment produces some magnetic flux through the superconducting detection coils, which is then detected by a SQUID magnetometer (Superconducting Quantum Interference Device). Because the

detection coils, connecting wires, and the SQUID input coil form a closed superconducting loop, any change of magnetic flux in the detection coils produces a change in the persistent current in the detection circuit, which is proportional to the change in magnetic flux. The SQUID electronics produces an output voltage that is proportional to the current flowing in the SQUID input coil. Hence, the SQUID device has a function as an extremely sensitive current-to voltage convertor. The SQUID we used can operate in a magnetic field as large as 7 teslas in the temperature range of 2 K to 400 K.

Figure 2.5 is a photograph of the MPMS XL system used in the magnetic measurements of the (1-x)PFW-xPT solid solution single crystal.

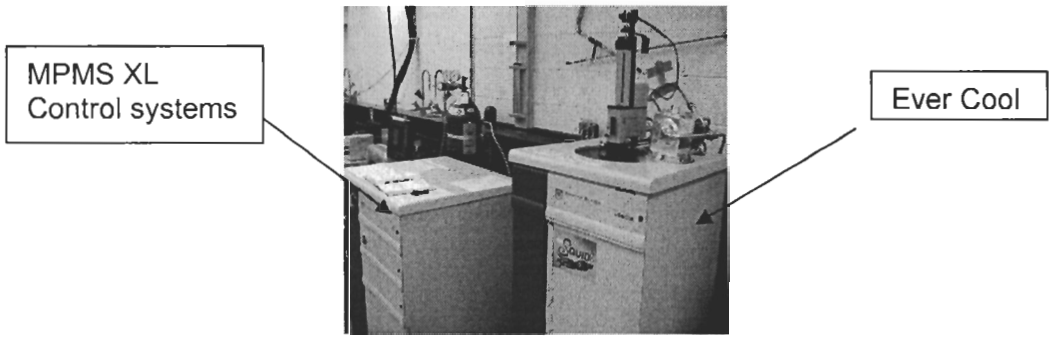

Figure 2.5: MPMS XL magnetic measurement system.

2.7 Mössbauer Spectroscopy

2.7.1 Simple Principle of Mössbauer Spectroscopic Measurement

The Mössbauer effect is recoilless nuclear resonance absorption, in which a system absorbs a quantum of energy equal to the difference between two energy states. It was discovered in 1958 by the German physicist R. L. Mössbauer, who was awarded the Nobel Prize for this work [11].

Mössbauer spectroscopy is also γ-ray (gamma ray) spectroscopy. The gamma rays are electromagnetic rays. The only difference between gamma rays and X-rays is that the former comes from the nucleus and is somewhat higher in energy (14.4 keV for ^{57}Fe) than the latter. γ-rays are produced by the decay of radioactive elements such as $^{57}Fe_{29}$ or $^{119}Sn_{50}$. Under certain conditions of 'recoilless emission', all of this energy change is transmitted to the emitted γ-rays with a highly monochromatic beam of radiation. If a sample contains similar atoms to the emitter, the γ-rays may be absorbed by the same atoms in the sample. A Mössbauer spectrum is normally produced by varying the energy of γ-rays and measuring the nuclear resonance absorption as a function of energy of γ-rays. In practice, the energy of the γ-rays is modified by making use of the Doppler effect, in which the γ-ray source is moved at a constant velocity either towards or away from the sample. This can increase or decrease the energy of the γ-rays on a sample. Hence, it enables the very small energy changes resulting from the hyperfine interactions between the nucleus and its surrounding electrons to be investigated.

Several types of information may be obtained from Mössbauer spectroscopy. First, if emitter and sample are identical, the resonant absorption peak occurs when the radiation source is stationary. Secondly, when the source and the absorbent are not identical, the absorption peak is shifted, which is called chemical shift (isomer shift), δ. The chemical shift arises from the columbic interaction of the nuclear charge and the electron charge. The variation of electron density around the nucleus is closely related to the oxidation states, coordination numbers and chemical bond character [12].

2.7.2. Quadrupole Splitting and Magnetic Hyperfine Splitting

When the nuclear quadrupole moment appears in an asymmetric electric field produced by an asymmetric electric charge distribution or ligand arrangement, an electric quadrupole interaction occurs. This gives rise to a splitting of the nuclear energy level. In case of ^{57}Fe, the excited state, I (spin quantum number) = 3/2, splits into two substates characterized by m_I (magnetic quantum number) = $\pm$ ½ and $m_I = \pm$ 3/2 in the presence of a non-zero electric field gradient. This leads to a two-line spectrum and the two lines are separated by the quadrupole splitting Δ, as shown in the middle of Fig. 2. 6. Δ is sensitive to local structure and oxidation state [12, 13].

When nucleus and spin state are placed in a magnetic field, there is a magnetic dipole interaction between any nuclear magnetic moment and magnetic field. The magnetic field arises either from the internal magnetic field produced by the samples or from an externally applied field. Each nuclear energy level splits into $(2I + 1)$ sublevels. For isotope ^{57}Fe, the excited state I = 3/2 has four sublevels and the ground state I = ½ splits into two. A total of six-line magnetic hyperfine splitting (nuclear level) can be obtained according to the selection rule, as shown on the right of Fig. 2.6. Hence, six possible absorption lines (sextet) appear in a Mössbauer spectrum. The study of hyperfine splitting, especially as a function of temperature, can provide useful information on magnetic ordering within the samples.

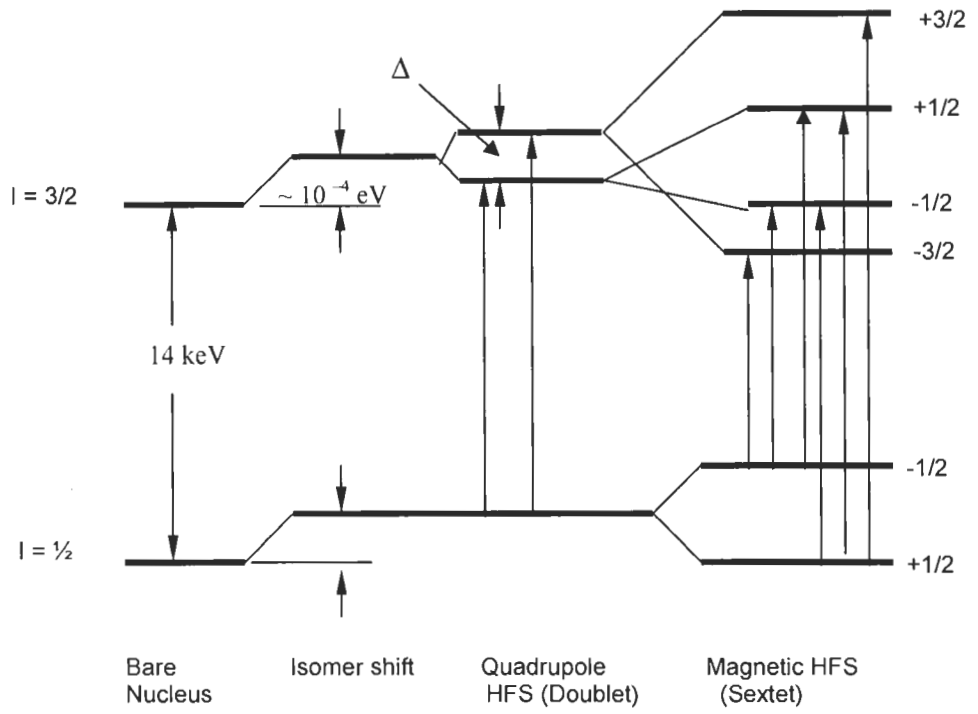

Figure 2.6: Energy level diagram for ^{57}Fe showing the origins of the isomer shift, quadrupole hyperfine splitting and magnetic hyperfine splitting. Each of the vertical arrows on the right side between ground and excited states represents a possible absorption line. HFS stands for hyperfine splitting.

2.7.3 Mössbauer Spectroscopic Experimental

Mössbauer measurement system mainly includes a radioactive source containing the Mössbauer isotope in an excited state and an absorber consisting of the material to be investigated which contains this same isotope in its ground state. A detector is placed behind the absorber for collection of the γ-rays that is not absorbed by a sample. In our experiment, the source for ^{57}Fe Mössbauer spectroscopy is radioactive ^{57}Co which undergoes a spontaneous electron capture transition to give a metastable state of ^{57}Fe. It in turn decays to the ground state through a gamma ray cascade. The energy of Mössbauer

gamma rays is 14.4 keV. Another major component is a device called a multichannel analyser that can store an accumulated total of γ-counts registered by the detection system. When a given channel is open, only γ counts coming at the same velocity from the γ-ray source are accumulated. Therefore, the channel number in practice represents a different γ-ray energy. A Web Research spectrometer in the transmission mode is used in our Mössbauer spectroscopic measurements in the temperature range of 295 K~4.4 K. The WMoss (v. 2.5) Mössbauer spectral analysis software is used to fit the experimental data. The experiments at high temperatures (353 K and 373 K) are carried out by use of a constant acceleration Harwell Mössbauer drive. A sample for Mössbauer measurements is usually prepared in the form of a thin disc or thin layer of powders sandwiched between the Kapton tapes.

Mössbauer spectroscopy is used in this work to investigate the magnetic properties and hyperfine interactions of the PFW and PFW-PT solid solution.

2.8 References

[1] A. R. West, *Basic Solid State Chemistry*, John Wiley & Sons, Ltd., Chichester (1996)

[2] G. H. Stout and L. H. Jensen, *X-ray structure determination*, John Wiley & Son, New York (1989).

[3] Y.-H. Xu, *Ferroelectric Materials and Their Applications*. North-Holland, the Netherlands (1991).

[4] C. B. Sawyer and C. H. Tower, *Phys. Rev.* **35**, 269 (1930).

[5] J. K. Sinha, *J. Sci. Instrum.* **42**, 696 (1965).

[6] Y.-H. Bing, *PhD thesis,* Simon Fraser University (2005).

[7] *Differential Scanning Calorimeter Module Operation Manual*, DSC 6200, Seiko Instruments Inc.

[8] M. E. Brown, *Handbook of Thermal Analysis and Calorimetry*, Elsevier Science B. V. Netherlands, (1998).

[9] W. M. Visscher, *Annals of Physics* **9**, 194 (1960).

[10] *MPMS User's Manual*, Quantum Design, San Diego, (2003).

[11] R. L. Mössbauer, *Z. Physik* **151**, 124 (1958).

[12] Richard l. Cohen, *Applications of Mössbauer Spctroscopy* **1**, Academic Press New York, (1976).

Chapter 3:
Synthesis, Structure and Properties of the $(1-x)Pb(Fe_{2/3}W_{1/3})O_3$-$xPbTiO_3$ [(1-x)PFW-xPT] Solid Solution Ceramics

The following chapter is a revised version of the paper published in ***Journal of Solid State Chemistry*** **163**, 484-490 (2002) by **L. Feng and Z.-G. Ye**. The use of this article is by permission of the publisher of Elsevier, Science.

3.1 Introduction

Complex perovskite $Pb(Fe_{2/3}W_{1/3})O_3$ (PFW) exhibits a broad and diffuse maximum of dielectric permittivity around T_m = 180 K with strong frequency dispersion [1]. Macroscopically, no ferroelectric phase transition occurs upon cooling through T_m. These properties are characteristic of relaxor ferroelectric behaviour (2-4). PFW shows an average primitive cubic perovskite structure with $Pm\bar{3}m$ group, in which the A-site are occupied by Pb^{2+} ions and the octahedral B-sites positions are filled by Fe^{3+} and W^{6+} ions at random. On the microscopic scale, polar nanoregions (or clusters) are expected to exist due to composition fluctuations and partial order/disorder, which is believed to be the origin of the relaxor ferroelectric behavior (2-4). On the other hand, PFW contains paramagnetic Fe^{3+} ($3d^5$) ions on the B-site with an occupancy of 66.7%. Magnetic order may occur upon cooling while the polar microdomains develop. PFW single crystals indeed show two antiferromagnetic orderings at T_{N1} = 350 K and T_{N2} = 20 K, respectively [5]. The former was supposed to result from the magnetic interactions *via* the superexchange pathway, $-Fe^{3+}- O - Fe^{3+}-$, within the disordered local clusters, and the

latter would arise from the $-Fe^{3+} - O - W - O - Fe^{3+} -$ superexchange pathway within the ordered microdomains [5]. The magnetic and dipolar interactions in PFW are expected to give rise to some peculiar properties in this relaxor.

It was known that the synthesis of pure PFW is difficult because of the formation of other non-ferroelectric phases, such as pyrochlore $Pb_2FeWO_{6.5}$, $PbWO_4$, and Pb_2WO_5. Almost-pure polycrystalline PFW was prepared using the columbite/wolframite precursor method [6], with improved dielectric properties compared with the samples prepared by the conventional mixed-oxide method [7, 8], in which lead tungsten oxide second phases ($PbWO_5$ and Pb_2WO_5) seemed to be present in a remarkable amount. In the columbite process, direct reaction between the B-site metal oxides and PbO is basically prohibited at the early stage, preventing the formation of the pyrochlore-type phase.

When PFW forms multicomponent systems with other ferroelectrics, the materials exhibit excellent multifunctional properties due to an improvement of dielectric properties, a higher Curie temperature, and a lower firing temperature [9-11]. Therefore, PFW has been known as a promising material for a multilayered ceramic capacitor [11]. Among the binary systems, $Pb(Fe_{2/3}W_{1/3})O_3$–$PbTiO_3$ (PFW-PT) is of particular interest. PFW is a relaxor ferroelectric and antiferromagnet, while $PbTiO_3$ is a typical ferroelectric with a sharp maximum of dielectric constant at Tc = 763 K. It is possible to move the Curie temperature to around room temperature and to modify the relaxation behavior by choosing an appropriate amount of PT in the system. Some results were reported on the preparation of the PFW and the PFW-PT ceramics at high temperature using additives or columbite method [6, 9]. It is found that the relaxor ferroelectric behaviour attenuates

with the increase of the PT content. But systematic studies of the PFW-PT system in terms of phase transitions and dielectric and magnetic properties are still lacking.

In the present work, an improved B-site precursor method is developed to synthesize a highly pure perovskite phase of (1-x)PFW-xPT. The phase formation and the structural parameters are characterized by X-ray diffraction. Phase transitions and the related properties are studied by differential scanning calorimetry and dielectric measurements.

3.2 Experimental

A modified B-site precursor method (12-15) was adopted for the synthesis of (1-x)PFW-xPT , with various compositions, x = 0, 0.10, 0.20, 0.25, 0.30, 0.325, 0.35, 0.40, 0.60, and 0.80. It consists of a two-step reaction process taking place sequentially. In the first step, an intermediate (or precursor) phase or a mixture of phases was formed by means of reacting the oxides of the B-site elements. In the second step, the B-site precursor phase was reacted with the other (A-site) reactant to form the complex perovskite phase. When the intermediate phase has a columbite structure, such as $MgNb_2O_6$, the B-site precursor method can be referred to as the so-called "columbite method" [12].

Fe_2O_3 (99.99%, Alfa) and WO_3 (99.9%, Alfa) were mixed in a mole ratio of 1:1 and finely ground in acetone media for 4 hours, and then dried and preheated at 1000 °C for 2 hours to form Fe_2WO_6. Afterward, PbO (99.99%, GFS Chemicals) or a mixture of PbO and TiO_2 (99.99%, Aldrich) was mixed with Fe_2WO_6 in a stoichiometric ratio and finely ground in acetone media for 4 hours. The mixture was initially calcined at 800 °C

for 2 hours, reground, and pressed into a pellet with a weight of 2.3 g~2.5 g. This pellet was finally sintered at 850 °C–890 °C for 2-3 hours. With the increase of PT component, the sintering temperature was increased slightly. Figure 3.1 is a diagram of a Muffle furnace for the preparation of the PFW-PT ceramics. The temperature ramps were controlled at 5 °C/min for heating and 2 °C/min for cooling (to 700 °C), followed by a final cooling to room temperature at 250 °C/h. PFW and PFW-PT compounds were formed according to the following solid state reactions:

$$Fe_2WO_6 + 3PbO \longrightarrow 3Pb(Fe_{2/3}W_{1/3})O_3 \quad (3.1)$$

$$(1\text{-}x)Fe_2WO_6 + 3xTiO_2 + 3PbO \rightarrow 3Pb[(Fe_{2/3}W_{1/3})_{1-x}Ti_x]O_3 \quad (3.2)$$

Since the Fe_2WO_6 phase was presynthesized, the direct reactions between PbO and WO_3 can be avoided in the B-site precursor method. Therefore, subsequent formation of the pyrochlore $Pb_2FeWO_{6.5}$ phase will be suppressed in the final reaction.

Phase analysis and structural refinement of the (1-x)PFW-xPT system were performed based on powder X-ray diffraction measurement (Philips X-ray diffractometer, Cu$K\alpha$ radiation, $\lambda = 1.5418$ Å) .

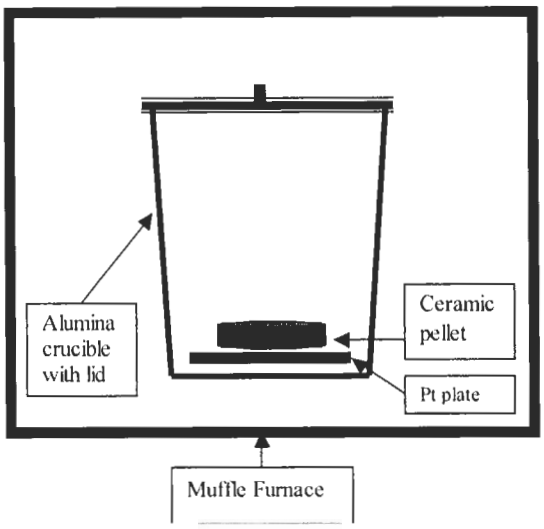

Figure 3.1: Schematic diagram of the set-up for the preparation of the (1-x)PFW-xPT ceramics at high temperature.

The thermal analysis was performed using a Seiko ExStar DSC 6200 apparatus for the (1-x)PFW-xPT ceramic sample. All the DSC runs were performed under flowing nitrogen gas using alumina powder (20~30 mg) as reference. The sample with 30~40 mg was first heated at 20 ^{o}C/min to 600 K to eliminate any adsorbed H_2O traces, and then cooled to 170 K, followed by heating to 500 K at a cooling/heating rate of 10 ^{o}C/min.

The ceramic pellet was properly polished into a sample with a size of ~ϕ10 x 1.0 mm^3. Silver paste was put on top and bottom surfaces of the sample that forms electrodes. The ceramic electrode was dried at 150 ^{o}C in oven for 2 hours before measurements. Complex dielectric permittivity of the (1-x)PFW-xPT ceramics was measured as a function of temperature at frequencies f = 1, 10, and 100 kHz, under isothermal conditions. The measurements were carried out upon heating from 100 to 600 K at the temperature intervals of 3~5 degrees by means of a computer-controlled

impedance analyzer (Solartron 1260) associated with a dielectric interface (Solartron 1296).

3.3 Phase Analysis and Structural Refinement

Figure 3.2 shows the XRD patterns of Fe_2WO_6 before and after calcining, as well as the diffraction patterns of $ZnTa_2O_6$ (tri-αPbO_2 structure) [16] and $MgNb_2O_6$ (columbite structure) [17] as references. From the comparison of Fig.3.2b with Fig. 3.2c, it can be seen that Fe_2WO_6 obtained as the B-site precursor compound $B_2'B''O_6$, crystallizes in a tri-αPbO_2 type structure, rather than in a columbite-type structure as reported in Ref. [6]. The two structures can be distinguished from each other according to the XRD patterns given in Fig. 3.2c and 2d.

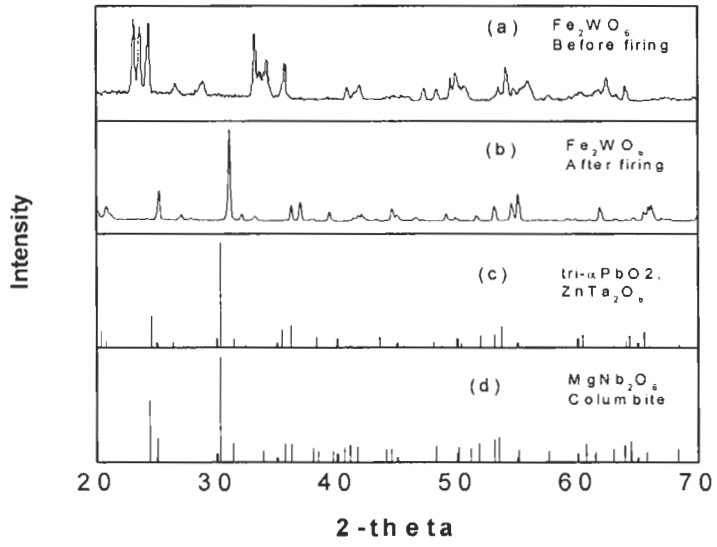

Figure 3.2: X-ray diffraction patterns of (a) Fe_2WO_6 before firing; (b) Fe_2WO_6 after firing at 1000 ^oC for 2 h; (c) $ZnTa_2O_6$ of tri-αPbO_2 structure; and (d) $MgNb_2O_6$ of columbite structure [17].

Identification and analysis of the perovskite phase with regard to the undesirable pyrochlore phase was carried out after the final reaction. The content of pyrochlore phase in the products was calculated according to the following equation [18],

$$\text{Pyrochlore content (\%)} = \{I_{pyro}(222)/[I_{pyro}(222) + I_{perov}(110)]\} \times 100, \qquad [3.3]$$

where $I_{pyro}(222)$ is the intensity of the (222) reflection peak of the pyrochlore phase and $I_{perov}(110)$ is the intensity of the (110) peak of the perovskite phase. Figure 3.3 shows the XRD patterns of the PFW samples prepared at 800 °C for 2 h (a) and sintered at 890 °C (b). A nearly pure PFW phase was formed after calcinations (with the pyrochlore content below the detectable limit) and a highly pure PFW product was obtained after sintering. These results show an improvement in the preparation of pure PFW by the B-site precursor technique, compared with the conventional mixed-oxide method (10, 19, 20).

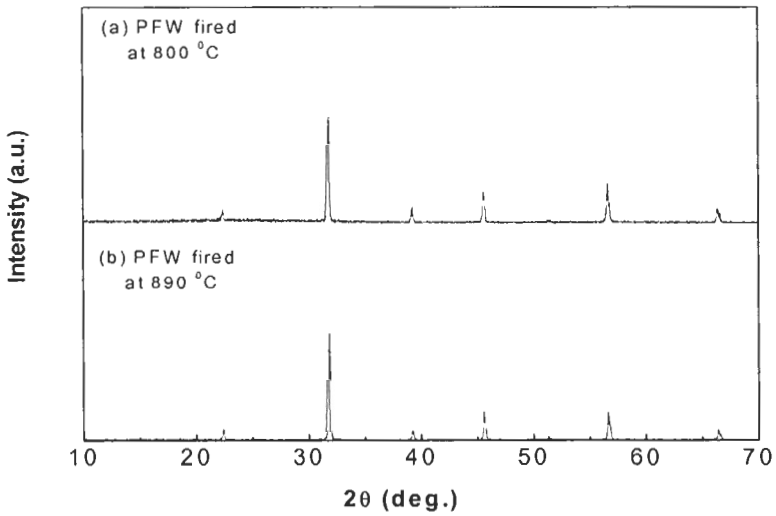

Figure 3.3: X-ray diffraction patterns of (a) PFW powder after calcining at 800 °C and (b) PFW ceramics after sintering at 890 °C, both showing the perovskite phase.

The XRD patterns of various compositions of (1-x)PFW-xPT (x = 0 to 0.80) are presented in Fig. 3.4. The compounds of $0 \leq x \leq 0.25$ show a cubic perovskite structure at room temperature. When the PT content, x, is increased to higher than 0.25, the diffraction peaks (100), (200), and (211) start splitting. With further increase of x, the splitting becomes more and more significant for all the indexed peaks except for the (111), indicating that (1-x)PFW-xPT gradually transforms from a pseudocubic perovskite structure into a tetragonal structure.

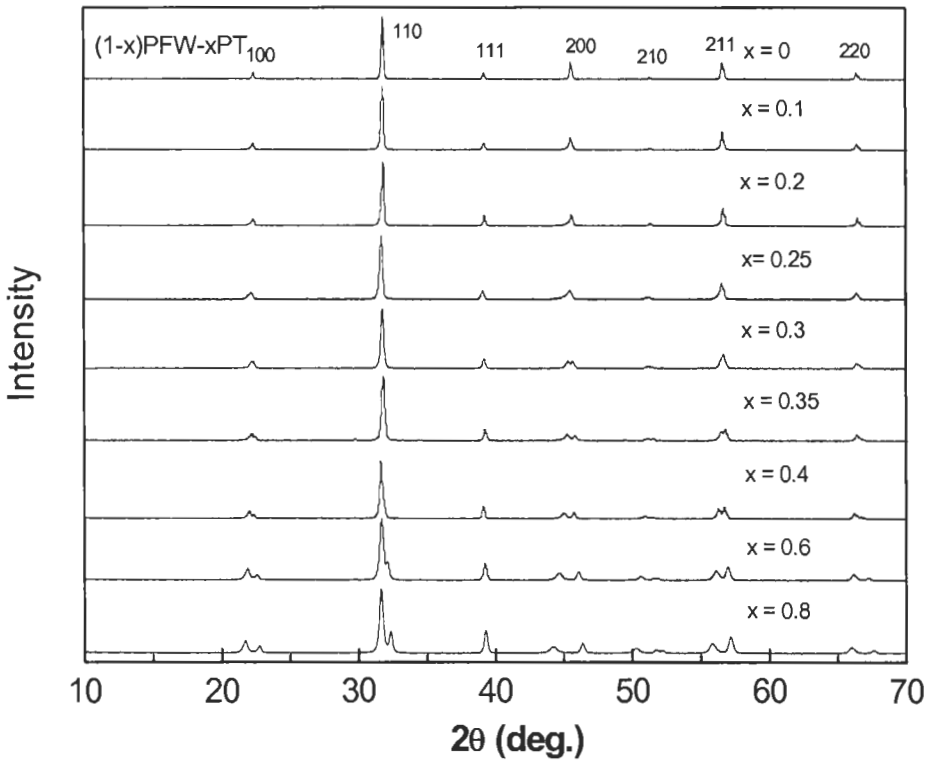

Figure 3.4: X-ray diffractograms for various compositions of the (1-x)PFW-xPT system at room temperature, showing a tetragonal splitting for $x \geq 0.25$.

The lattice parameters of (1-x)PFW-xPT were refined in the cubic $Pm\bar{3}m$ and/or tetragonal *P4mm* phase. Figure 3.5 shows the variation of the lattice parameters as a function of PT content. The parameter a of the cubic perovskite phase decreases slightly from 3.9909 Å to 3.9734 Å with the increase of x from 0 to 0.2. Such a variation can be attributed to the substitution of the smaller Ti^{4+} ions (r = 0.605 Å) for the Fe^{3+} ions (r = 0.645 Å) on the B-site, while W^{6+} (r = 0.60 Å) has almost the same size as Ti^{4+} [21]. At x = 0.40, the tetragonal symmetry can be monitored with a clear split of the parameters, a = 3.9357 Å and c = 4.0433 Å. With further increase of x from 0.4 to 1.0, a continues to decrease slightly while c increases more pronouncedly. Accordingly, the c/a ratio augments from 1.0273 (for x = 0.4) to 1.0651 (for x = 1.0), indicating an increase of

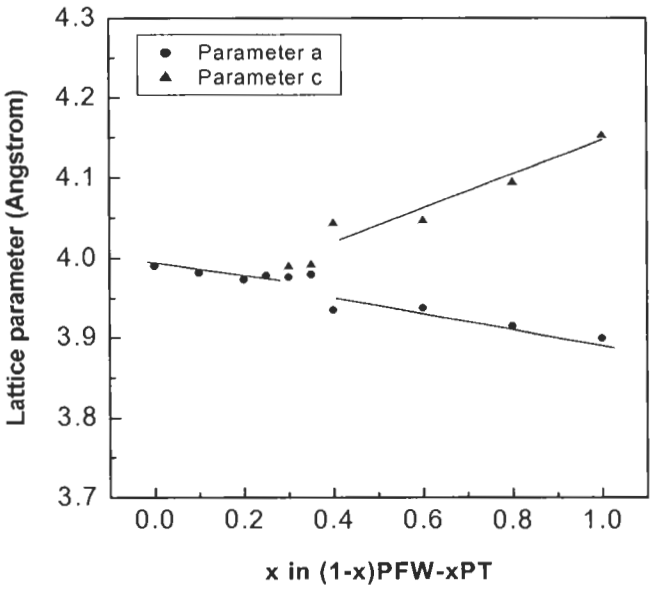

Figure 3.5: Variation of the pseudocubic (a) and tetragonal (a and c) lattice parameters with x for (1-x)PFW-xPT at room temperature. Solid lines indicate the data trend for visual reference only.

tetragonality (Fig. 3.6). The compositions of x = 0.30-0.35 show a very small split between a and c, and a c/a ratio close to 1, indicating the onset of tetragonal distortion from the cubic symmetry.

The corresponding volume change *versus* PT content is also presented in Fig. 3.6. The volume of the cubic phase decreases from 63.56 $Å^3$ to 62.73 $Å^3$ with x increasing from 0 to 0.2. The volume of the tetragonal phase increases slightly from 62.60 $Å^3$ (for x = 0.4) to 63.15 $Å^3$ (for x = 1.0), suggesting that the size effect of Ti^{4+} ions is predominated by the tetragonal distortion of the unit cell. For x = 0.25 to 0.35, an irregular variation of lattice volume is observed, suggesting that both the cubic and the tetragonal phases may coexist within that composition range at room temperature.

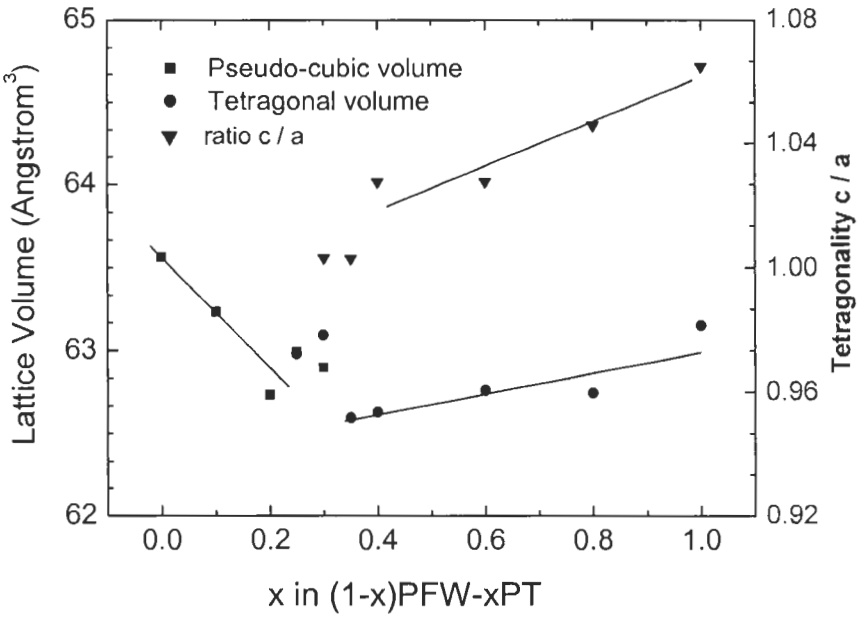

Figure 3.6: Variation of the pseudocubic and tetragonal unit cell volume and the tetragonality c/a as a function of Ti content in (1-x)PFW-xPT. Solid lines indicate the data trend for visual reference only.

3.4 Differential Scanning Calorimetry (DSC) Measurements

Differential scanning calorimetry (DSC) was carried out to analyze the phase transition in the (1-x)PFW-xPT ceramic system, in which a morphotropic phase boundary (MPB) is expected. Figure 3.7 shows some DSC results. Upon heating, two endothermic peaks occur at 250 and 281 K, 240 and 311 K, and 210 and 342 K, respectively, for each of the compositions x = 0.25, 0.30, and 0.35. The low-temperature thermal event indicates the morphotropic phase boundary from the low-temperature phase to the tetragonal phase at T_{MPB}, and the high-temperature peak shows the tetragonal to cubic phase transition at Tc. Therefore, the morphotropic phase boundary of (1-x)PFW-xPT is localized in the composition range of $0.25 \leq x \leq 0.35$.

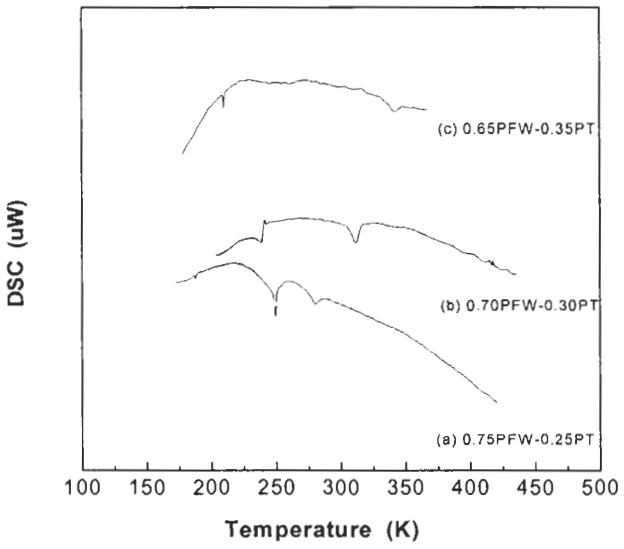

Figure 3.7: DSC scanning curves upon heating for (a) 0.75PFW-0.25PT, (b) 0.70PFW-0.30PT, and (c) 0.65PFW-0.35PT.

3.5 Dielectric Properties

The temperature and frequency dependences of the real part of dielectric permittivity are presented in Fig. 3.8 for different compositions. In Fig. 3.8a, PFW displays a broad and diffuse maximum of dielectric constant with strong frequency dispersion, demonstrating a typical relaxor ferroelectric in the system. The temperature of permittivity maximum T_m varies from 181 K at 1 kHz to 197 K at 100 kHz. The maximum value of the dielectric constant decreases with increasing frequency. The dielectric dispersion below T_C reflects typical relaxor ferroelectric behavior arising from the responses of polar microdomains (relaxators) with a spectrum of relaxation time [2-4]. Since the relaxation appears at low temperature (<181 K), the contribution of mobile charges is not significant. In the high-temperature paraelectric phase ($T > T_m$), another frequency dispersion appears, which is particularly significant at low frequencies. Such a low-frequency dispersion (LFD) can be attributed to the conductivity effects due to slowly mobile electronic charges. These charges arise from the Fe^{3+} ions (d^5), which are usually combined with Fe^{2+} ions to form charge defects. Electrons hopping between $Fe^{3+}$and Fe^{2+} ions would result in the conductivity, which in turn gives rise to dielectric dispersion, more remarkable at lower frequencies, as shown in Fig. 3.8a. The LFD was also observed in other relaxor ferroelectric systems, such as $Pb(Mg_{1/3}Nb_{2/3})O_3$-$PbTiO_3$, where the contribution to the electronic conduction comes from structural defects [3]. The reason the LFD is more significant in the high-temperature phase is two-fold. First, the paraelectric phase of PFW-PT has a disordered cubic perovskite structure like PFW [5], with the Fe^{3+}, W^{6+}, and Ti^{4+} ions statistically distributed on the B-sites. This provides a relatively short Fe^{3+} - Fe^{2+} distance, favouring the electron hopping between the two

ions. Second, the LFD appears more significantly in the high-temperature range (>250 K), where thermal activation enhances the electric conduction and hence results in the frequency dispersion.

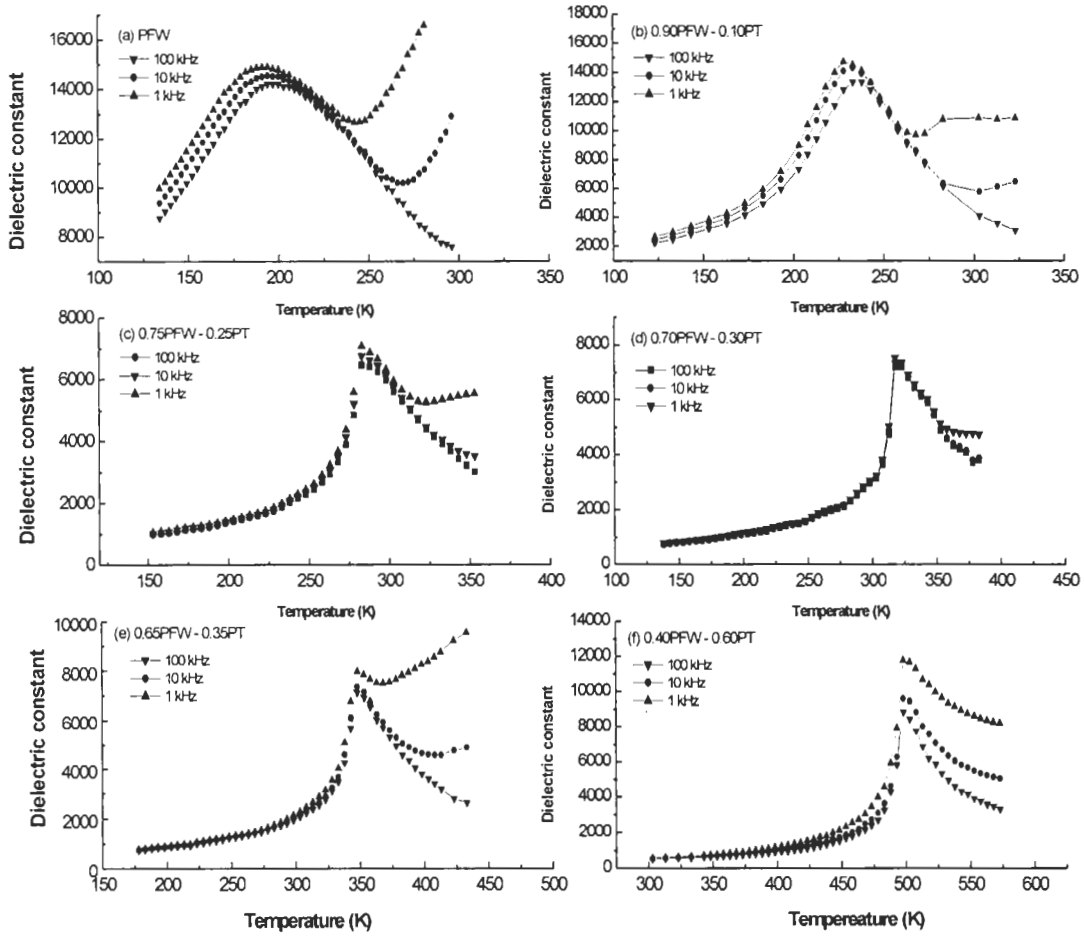

Figure 3.8: Temperature dependences of the real part of dielectric permittivity at frequencies f = 1, 10, and 100 kHz for various compositions: (a) PFW, (b) 0.90PFW-0.10PT, (c) 0.75PFW-0.25PT, (d) 0.70PFW-0.30PT, (e) 0.65PFW-0.35PT, and (f) 0.40PFW-0.60PT.

With the increase of PT content, the low-temperature dielectric dispersion (i.e., the relaxor relaxation below T_C) is significantly attenuated. The dielectric properties of 0.75PFW-0.25PT are shown in Fig. 3.8c, where no significant relaxation appears around and below Tc = 288 K, indicating that the substitution of Ti^{4+} for $(Fe_{2/3}W_{1/3})^{4+}$ has induced a transformation from the relaxor regime in PFW toward a long-range (normal) ferroelectric state. The dielectric permittivity of 0.70PFW-0.30PT shows nondispersive peaks at Tc = 320 K, corresponding to the ferro- to paraelelctric phase transition (Fig. 3.8d). Tc further increases to 350 K and 500 K for x = 0.35 (Fig. 3.8e) and 0.60 (Fig. 3.8f), respectively.

For the compositions around the morphotropic phase boundary, x = 0.25-0.35, in contrast to the DSC measurements in which the morphotropic phase transition has been clearly detected with T_{MPB} varying from 250 K to 210 K, the temperature dependence of the dielectric constant (Fig. 3.8c-e) show only weak or broad anomalies around T_{MPB}. This phenomenon can be understood on the basis of the fact that the MPB transition occurs between two polar (and ferroelectric) phases, and therefore involves relatively weak structural instability and small net polarization changes compared with the ferro-/paraelectric transition at Tc. As a result, the dielectric measurements usually show weak effects for the MPB transition. This behaviour was also observed in the other relaxor-based solid solution systems with MPB, such as $Pb(Mg_{1/3}Nb_{2/3})O_3$-$PbTiO_3$ [22] and $Pb(Zn_{1/3}Nb_{2/3})O_3$-$PbTiO_3$ [23], in which the MPB transition appears as a weak and broad dielectric anomaly, while it can be clearly detected as a first-order transition by optical domain studies [24] or by DSC measurements (with appearance of latent heat) [25].

Therefore, thermal analysis by DSC is more sensitive for detecting the morphotropic phase transition in the PFW-PT system.

3.6 Morphotropic Phase Diagram of the PFW-PT Binary System

Based on the results of XRD, DSC, and dielectric measurements, a ferroelectric phase diagram for the (1-x)PFW-xPT binary system has been established, as shown in Fig. 3.9. It indicates the phase boundaries and phase transition temperatures of the solid solution system. Up and down triangles represent the transition temperatures detected by DSC analysis and the filled and open circles correspond to the phase transition temperatures obtained from the dielectric measurements. The Curie temperature increases almost linearly with the increase of PT content x, from T_m = 181 K for PFW to Tc = 763 K for PT. The symmetry of the low-temperature ferroelectric phase with a small PT content can be refined in a pseudocubic symmetry with a slight rhombohedral *R3m* distortion, as in the case of $Pb(Zn_{1/3}Nb_{2/3})O_3$-PT [26] and $Pb(Mg_{1/3}Nb_{2/3})O_3$-PT [27] systems. For example, the edge and angle of the unit cell are individually 3.989 Å and 90.064 ° for 0.80PFW-0.20PT, and 3.978 Å and 89.976 ° for 0.75PFW-0.25PT at room temperature according to the rhombohedral-hexagonal transformation to the XRD measurement results [28]. A cubic perovskite structure appears above the Curie temperature line. At room temperature, the cubic phase transforms into the tetragonal phase at a PT content of about 25%. The cubic and tetragonal phases coexist for the compositions around the phase boundary, as shown by the anomalies in the variations of lattice parameters and volume (Figs. 3.5 and 3.6). Below the Tc line, the ferroelectric rhombohedral and tetragonal phases are separated by a morphotropic phase boundary

(MPB) which is located in the composition range $0.25 \leq x \leq 0.35$ below ~ 280 K. At the compositions near the MPB, both the rhombohedral and the tetragonal phases may coexist. For compositions close to the MPB, successive phase transitions from the rhombohedral to the tetragonal and then to the cubic phase may occur upon heating, as revealed by the DSC analysis (Fig. 3.7).

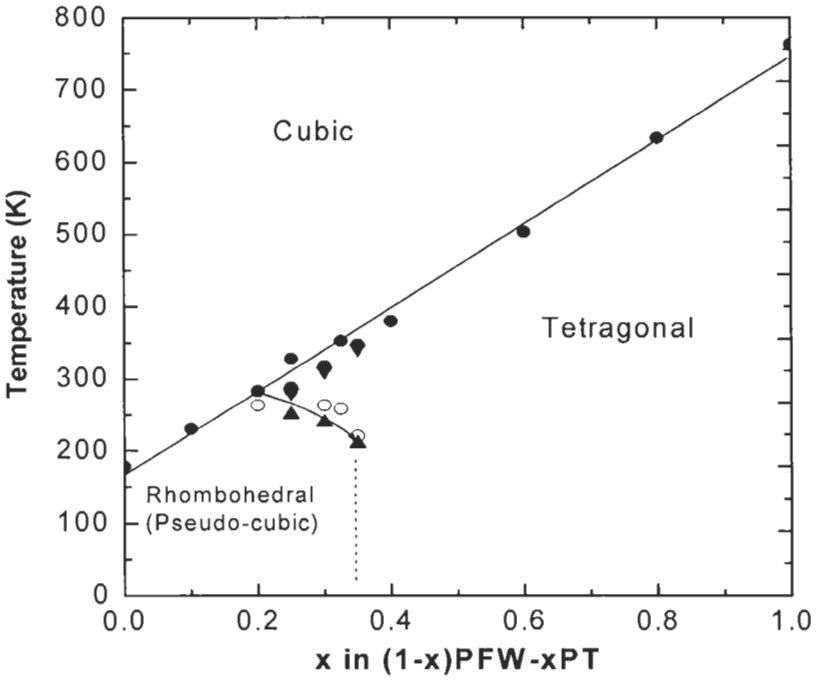

Figure 3.9: Phase diagram of the (1-x)PFW-xPT system delimiting the high-temperature cubic phase and the low-temperature ferroelectric rhombohedral (pseudocubic) and tetragonal phases. A morphotropic phase boundary (MPB) is located at $0.25 \leq x \leq 0.35$. Up and down triangles represent the transition temperatures measured by DSC analysis; filled and open circles correspond to the phase transition temperatures detected by dielectric measurements.

3.7 Conclusions

A modified B-site precursor method, which consists of forming the tri-αPbO_2-type Fe_2WO_6 phase prior to final reactions with PbO or (PbO + TiO_2), has been developed to prepare a pure and complete solid solution system of (1-x)PFW-xPT. The structural refinements based on X-ray diffractograms at room temperature indicate that the perovskite (1-x)PFW-xPT transitions from a cubic phase to a tetragonal phase at a PT content of $x \geq 0.25$, where a splitting of the cubic lattice parameter a into the tetragonal parameters a and c.

The temperature dependences of the dielectric permittivity at various frequencies have revealed that the ferroelectric phase transition temperature Tc increases with the increasing Ti^{4+} content on the B-site, while the relaxor ferroelectric behaviour of PFW is gradually transformed into a normal (long-range) ferroelectric state, as evidenced by the sharp and nondispersive dielectric permittivity peaks around Tc for $x \geq 0.25$. For the compositions $0.25 \leq x \leq 0.35$, the DSC analyses have revealed a low-temperature phase transition at T_{MPB} which is related to the existence of a morphotropic phase boundary, in addition to the high-temperature ferro-/paraelectric phase transition at Tc.

A complete phase diagram for the (1-x)PFW-xPT system has been established, which delimits a high-temperature paraelectric cubic phase, a ferroelectric rhombohedral (pseudocubic) phase, and a ferroelectric tetragonal (*p4mm*) phase. The morphotropic phase boundary is located at $0.25 \leq x \leq 0.35$, which separates the rhombohedral (pseudo-cubic) phase from the tetragonal phase. PFW-PT compositions within the MPB range exhibit successive phase transitions from the rhombohedral to a tetragonal, and then to a cubic phase upon heating. Such a phase diagram is of relevance to further investigation

and understanding of the magnetic, dielectric, and magnetoelectric properties of the PFW-PT system.

3.8 References

[1] Z.-G. Ye and H. Schmid, *Ferroelectrics* **162**, 119 (1994).

[2] L. E. Cross, *Ferroelectrics* **76**, 241 (1987).

[3] L. E. Cross, *Ferroelectrics* **151**, 305 (1994).

[4] Z.-G. Ye, *Key Eng. Mater.* **155 – 156**, 81 (1998).

[5] Z.-G. Ye, K. Toda, M. Sato, E. Kita and H. Schmid, *J. Korean Phys. Soc.* **32**, S1028 (1998).

[6] L. Zhou, P. M. Vilarinho and J. L. Baptista, *J. Mater. Sci.* **33**, 2673 (1998).

[7] P. M. Vilarinho, J. L. Baptista, *J. Eur. Ceram. Soc.* **11**, 407 (1993).

[8] C. H. Lu, N. Ishizawa, K. Shinozaki, N. Mizutani, M. Kato, *J. Mat. Sci. Lett.* **7**, 1078 (1988).

[9] Y. –J. Kim and S.-W. Choi, *Ferroelectrics* **186**, 287 (1996).

[10] M. Yonezawa, *Am. Ceram. Soc. Bull.* **62**, 1375 (1983).

[11] T. R. Shrout and A. Halliyal, *Am. Ceram. Soc. Bull.* **66**(4), 704 (1987).

[12] S. L. Swartz, T. R. Shrout, *Mater. Res. Bull.* **17**, 1245 (1982].

[13] A. Halliyal, U. Kumar, R. E. Newhnam, and L. Cross, *Am. Ceram. Soc. Bull.* **66**, 671 (1987).

[14] B.-H. Lee, N.-K. Kim, J.-J. kim, and S.-H. Cho, *Ferroelectrics* **211**, 233 (1998).

[15] M. –C. Cae, S. –M. Lim, and N. K. Kim, *Ferroelectrics* **242**, 25 (2000).

[16] Wong-ng, H. McMurdie, B. Paretzkin, C. Hubbard, and A. Dragoo, JCPDS-ICDD File #39-1484 [powder Diffraction **3**, 121 (1998)]

[17] C. Roob and McCarthy, *JCPDS-ICDD File #33-875.*

[18] G. Drazic, M. Trontelj, and D. Kolar, *Mater. Sci. Eng.* **B26**, 189 (1994).

[19] G. A. Smolenskii, A. I. Agranovskaya, V. A. Isupov, *Sov. Phys. Sol. State* **1**, 907 (1959).

[20] M. Yonezawa and T. Ohno, "Proceedings of the Japanese Study Seminar on Dielectric and Piezoelectric Ceramics," **T-8**, 1 (1982).

[21] R. D. Shannon, *Acta. Crystallogr* **A32** 751 (1976).

[22] S.W. Choi, T. R. Shrout, S. J. Jang, and A. S. Bhalla, *Mater. Lett.* **8**, 253 (1989).

[23] L. Zhang, M. Dong, and Z.-G. Ye, *Mater, Sci. Eng.* B**78**, 96 (2000).

[24] Z.-G. Ye and M. Dong, *J. Appl. Phys.* **87**, 2312 (2000).

[25] M. Mendoza and Z.-G. Ye, unpublished.

[26] J. Kuwata and K. Uchino, and S. Nomura, *Jpn. J. Appl. Phys.* **21**, 1298 (1982).

[27] T. R. Shrout, Z. P. Chang, N. Kim, and S. Markgra, *Ferroelectrics Lett.* **12**, 63 (1990).

[28] B. D. Cullity, Elements of X-Ray Diffraction, Addision-Wesley Publishing Company, Inc. Reading, USA (1956).

Chapter 4:

Electrical Microstructure and Properties of Relaxor Ferroelectric $Pb(Fe_{2/3}W_{1/3})O_3$–$PbTiO_3$ Solid Solution System

4.1 Introduction

Complex perovskite $Pb(Fe_{2/3}W_{1/3})O_3$ [PFW] is a typical relaxor ferroelectric material exhibiting a broad and diffuse maximum of dielectric permittivity with strong frequency dispersion [1, 2]. PFW-based multi-component systems show excellent multi-functional properties due to an improvement of dielectric properties, a higher Curie temperature, and a low firing temperature [3, 4]. Therefore, PFW has been known as a promising material for multilayered ceramic capacitors [5].

The previous studies on PFW single crystals indicated that PFW indeed exhibits relaxor ferroelectric behaviour with the temperature of dielectric permittivity maximum around $T_m \approx 180$ K. Two types of magnetic interactions via (i) $-Fe^{3+}-O-Fe^{3+}-$ and (ii) $-Fe^{3+}-O-W-O-Fe^{3+}-$ were suggested to take place at the temperatures $T_{N1} = 350$ K and $T_{N2} = 20$ K, respectively [6]. In recent years, the solid solution of $Pb(Fe_{2/3}W_{1/3})O_3$ – $PbTiO_3$ (PFW-PT) has been given considerable attention. PFW has a disordered structure on the octahedral B-site of the perovskite that are occupied by Fe^{3+} and W^{6+} ions at random, which results in the presence of polar nanoregions giving rise to the ferroelectric relaxation [7]. $PbTiO_3$ is a typical ferroelectric compound with a sharp peak in the dielectric constant at the paraelectric/ferroelectric phase transition temperature T_C=763 K. The relaxor ferroelectric behaviour of PFW can be modified by the addition of the PT

content in the PFW-PT solid solution, as shown in Chapter 3. Up to now, systematic studies of PFW-PT system have been missing. No detailed information on the effects of microstructural phases on the electrical properties has been reported in the binary system [8].

Ac impedance spectroscopic technique has been applied to measure and analyze the electrical properties of materials in many fields, such as solid electrolytes [9], batteries [10], as well as most of electrochemical reaction processes. West *et al.* [11, 12] and Macdonald *et al.* [13] reported the impedance spectroscopic analysis of a number of electroceramics (polycrystalline material with useful electronic properties), such as $Ca_{12}Al_{14}O_{33}$ and $BaTiO_3$. This powerful method can characterize resistive (resistance) and reactive (capacitance and inductance) properties of electroceramic systems. In particular, it can be applied for distinguishing the electrical responses of each microstructural component or phases (electrode, grain boundary, grain bulk, *etc.*) according to their different electrical relaxation times and/or time constants (product of resistance and capacitance), and for indicating whether or not the overall conductance of the system is dominated by an individual phase (component) at different temperatures. Sakurai *et al.* [14] investigated the ac impedance spectroscopy of the PFW ceramics at room temperature. A simple equivalent electric circuit composed of resistance and capacitance of grain and grain boundary phases was presented to simulate the impedance spectra of the ceramics. The impedance analysis of the multi-component system $Pb(Zn_{1/3}Nb_{2/3})O_3$-$Pb(Fe_{2/3}W_{1/3})O_3$-$Pb(Fe_{1/2}Nb_{1/2})O_3$ [PZN-PFW-PFN] was reported by Drazic *et al.* [8]. However, so far, no detailed impedance spectroscopic measurements

combined with electric modulus formalism analysis on the PFW and PFW-PT polycrystalline ceramics have been reported.

In the previous chapter, highly pure peroviskite compounds of the (1-x)PFW – xPT solid solution were synthesized by an improved B-site precursor method and characterized by X-ray diffraction. In this chapter, ac impedance spectroscopic measurements of the ceramic system are carried out at different temperatures and frequencies. The relationships among microstructure, composition, and electrical properties have been analyzed and discussed based on the combined complex impedance and electrical modulus spectra.

4.2 Principles of Electric Analysis of Dielectric Ceramics

4.2.1 Impedance and Electrical Modulus Principles

When a small sine-wave signal, $\mathbf{V}(t) = V_m\sin(\omega t)$, where ω ($= 2\pi f$) is the angular frequency and V_m is the magnitude of voltage V, is applied to a material system, a steady state current $\mathbf{I}(t) = I_m\sin(\omega t + \theta)$ is generated. Here I_m is the magnitude of current I and θ is the phase difference between the voltage and the current ($\theta = 0$ when the system is a pure resistor). The complex impedance (Z*) of a system can be defined as [13]

$$\mathbf{Z^*} = \mathbf{V}(t) / \mathbf{I}(t) \quad , \tag{4.1}$$

and its magnitude:

$$Z_m = V_m / I_m . \tag{4.2}$$

In a pure resistance system, the impedance $\mathbf{Z^*} = R$ is a constant. If the system is a pure capacitor, the impedance $\mathbf{Z^*} = -j/\omega C$, where C is capacitance and imaginary number j =

$\sqrt{-1}$. In this case, θ is not equal to 0 and the impedance $\mathbf{Z^*}$ is frequency dependent. When a system is a parallel circuit composed of resistor and capacitor (parallel RC element), as shown in Fig. 4.1, the total impedance is given as follows:

$$\mathbf{Z^*} = (1/R+j\omega C)^{-1} = R/(1+\omega^2C^2R^2) - j\omega CR^2/(1+\omega^2C^2R^2) = Z' - jZ'', \qquad (4.3)$$

with $Z' = R/(1+\omega^2C^2R^2)$ and (4.4)

$$Z'' = \omega CR^2/(1+\omega^2C^2R^2) \quad , \qquad (4.5)$$

where Z' and Z" are real and imaginary parts of the impedance, respectively. The magnitude of the impedance is $|Z| = (Z'^2 + Z''^2)^{1/2}$. In addition, a circle equation can be deduced from Equations 4.4 and 4.5:

$$(Z'-R/2)^2 + Z''^2 = (R/2)^2 \qquad (4.6)$$

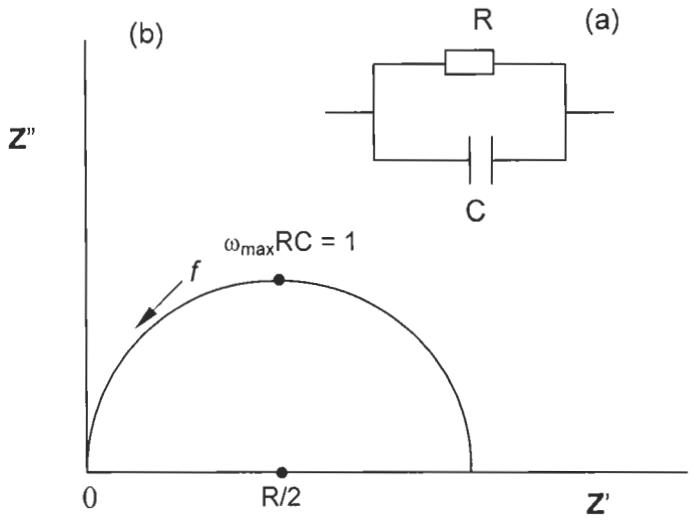

Figure 4.1: (a) Parallel RC circuit and (b) the corresponding ac impedance spectrum. Arrow indicates the direction of increasing frequency.

The corresponding impedance spectrum is a semicircle, as a function of frequency (f), as shown in Fig. 4.1b. In impedance experiments, the frequency applied is often in the range of $10^{-2} \sim 10^{7}$ Hz. It is easily found that the resistance can be obtained from the intercept on the real axis (Z' axis) at low frequency. In practice, it is equal to the diameter of the semicircle curve. By solving the differentiation equation dZ"/dZ' = 0, a relationship between the frequency at maximal imaginary, ω_{max}, and time constant, RC, can be obtained:

$$\omega_{max}RC = 1 \quad . \tag{4.7}$$

Therefore, the resistance and capacitance can be obtained by analyzing the impedance spectrum. The time constant (RC), which is independent of the sample geometry, and the frequency (f_{max}), are the two characteristic parameters to each semicircle. When an impedance spectrum is composed of a distorted semicircle due to the overlap of semicircles with similar time constants, it is difficult to get the numerical solution for each semicircle in the impedance spectrum. Hence, electric modulus analysis has to be applied in such complicated systems.

The complex electric modulus M* is defined as [12]:

$$\boldsymbol{M^*} = j\omega C_o \boldsymbol{Z^*} \, , \tag{4.8}$$

$$\boldsymbol{M^*} = M'\text{-}jM'' \, , \tag{4.9}$$

where C_o is the vacuum capacitance of the measuring cell electrodes with an air gap in place of the sample, $C_o = \varepsilon_o/k$, where ε_o is the permittivity of free space (8.854×10^{-14} F/cm), and $k = l / A$, is the cell constant where l is the thickness and A is the area. M' and M" are real part and imaginary part of the modulus, respectively. The modulus spectroscopy can give most emphasis to those elements with the smallest capacitance,

whereas impedance plots highlight those with the largest resistance. The combination of impedance and modulus analyses can effectively reveal the electrical features of each component (phase) in a complex electroceramic system.

In order to clearly analyze and interpret the impedance spectrum of a polycrystalline material system, it is necessary to have an equivalent circuit model that simulates the electrical properties of the spectrum. Each semicircle in impedance or modulus spectrum can be described by a parallel RC element in the circuit. Each parallel RC element is contributed by individual phase component (electrode, grain boundary, grain bulk, *etc.*) in the ceramic system. Therefore, a complicated impedance spectrum can be represented by a simple equivalent circuit, from which the electrical contributions to the system from each microstructural phase can be clearly depicted.

4.2.2 Microstructural Phase Model for Polycrystalline Ceramics

In polycrystalline ceramic systems, the microstructure is not uniform in local area and consists mainly of grain and grain boundary phases (and possibly very small amount of impurities). Each component (phase) makes an individual contribution to the total electrical properties of the ceramic system. Some conduction models have been proposed for the simulation of the electrical properties in electro-ceramic materials [13] based on different equivalent circuit diagrams, correlating the microstructure of the sample and its impedance spectra. One of them is the "series layer model" that is composed of two phases (grain and grain boundary) to be stacked in layers parallel to the measuring electrodes in the system. This model is equivalent to an electrical circuit with two parallel RC elements connected in series, as shown in Fig. 4.2(a). The impedance spectrum of the

series model usually consists of two semicircles in the complex impedance plane. Figure 4.2(b) shows the equivalent electrical circuit for the "parallel layer model", in which the layers of two different phases are stacked across the electrodes. It often shows only one relaxation (i.e. one semicircle in impedance spectrum). The third model termed the "brick layer model" (Fig. 4.2c) treats the ceramic microstructure as an array of cubic-shaped grains (bricks), separated by thin grain boundaries. In this model two current paths are possible. One is through the grains and across grain boundaries, and the other along grains boundaries. When the conductivity of grains is much larger than that of grain boundaries, the conduction passes predominantly through the grains and across grain boundaries. The circuit is equivalent to that of the "series layer model", and two semicircles appear in the impedance spectrum. If the conductivity of grain boundaries is higher than the conductivity of grains, the circuit is equivalent to the circuit of the "parallel layer model", and one semicircle often appears in the impedance spectrum.

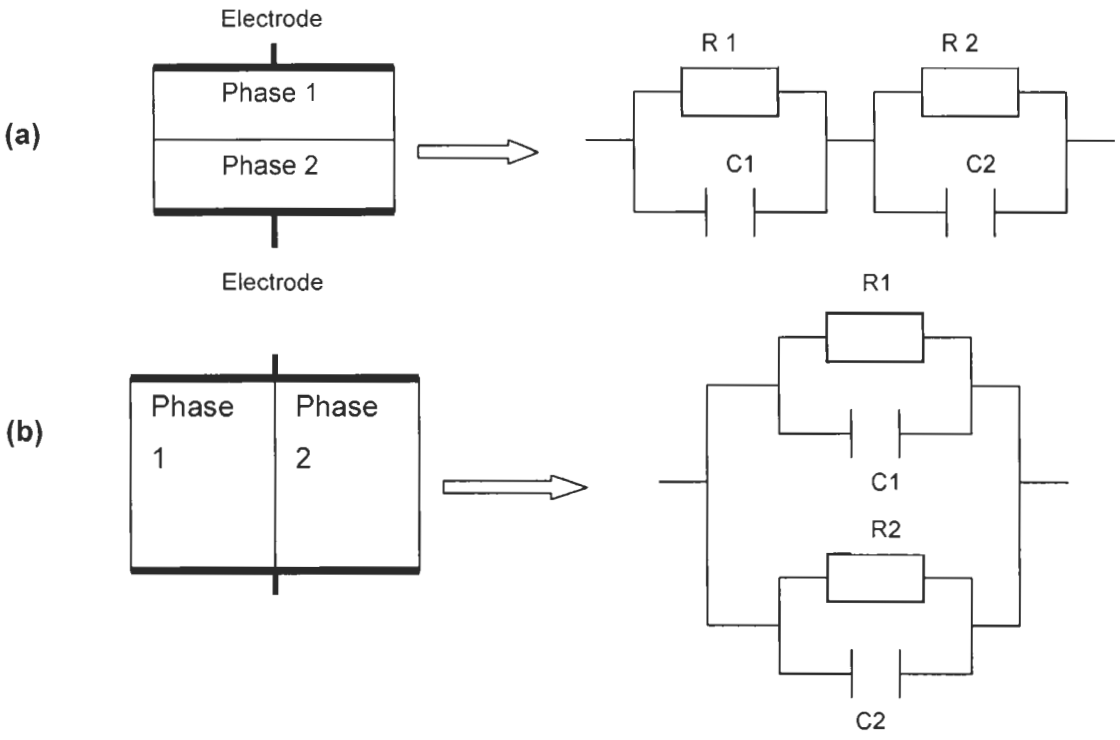

(C)

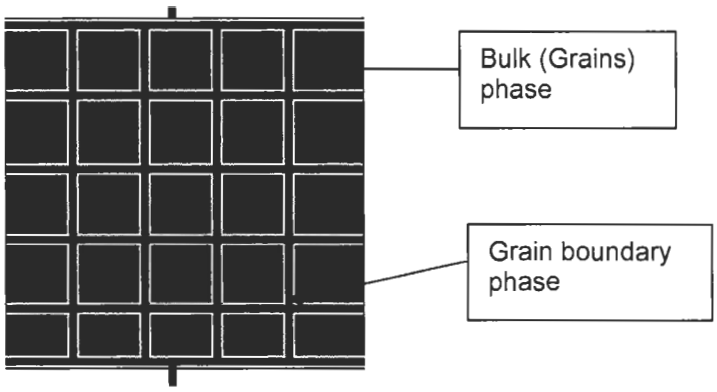

Figure 4.2: Various models for the ceramics with two-phase components. (a) "Series layer model" and the corresponding equivalent electrical circuit; (b) "Parallel layer model" and the associated equivalent circuit; and (c) " Brick layer model".

4.3. Experimental

A B-site precursor method consisting of a two-step reaction process was used for the preparation of the (1-x)PFW-xPT ceramics. A more detailed description can be found in Chapter 3.

Starting chemicals Fe_2O_3 (>99.9%, Alfa) and WO_3 (99.8%, Alfa) were mixed in a molar ratio of 1:1 and ground in the presence of acetone for 4 hours. A reaction was carried out at 1000 ^oC for 2 hours to form an intermediate compound of Fe_2WO_6, according to reaction (4.10). It has been found by XRD analysis that Fe_2WO_6 shows a tri-αPbO_2 –type structure of the $B'B"_2O_6$ formula, resembling a perovskite phase [15]:

$$Fe_2O_3 + WO_3 \longrightarrow Fe_2WO_6 \quad . \qquad (4.10)$$

In the second step, the intermediate phase Fe_2WO_6 was mixed with PbO in a stoichiometric ratio based on the following reactions:

$$Fe_2WO_6 + 3\ PbO \longrightarrow 3Pb(Fe_{2/3}W_{1/3})O_3 \quad (4.11)$$

$$(1\text{-}x)(Fe_2WO_6 + 3PbO + 3x\ TiO_2 \longrightarrow 3Pb(Fe_{2/3}W_{1/3})_{1-x}Ti_xO_3 \quad (4.12)$$

The mixture was ground in the presence of acetone for 4 hours, and initially calcinated at 800 °C for 2 hours, then reground and finally sintered at 850 °C ~ 890 °C for 2-3 hours. With the increase of PT content in PFW-PT, the firing temperature increases slightly. The heating and cooling rates were controlled at 5 °C/min and 2 °C/min, respectively.

Since the Fe_2WO_6 phase was made in the first reaction (4.10), direct chemical reaction between PbO and WO_3 in the second reaction (4.11) or (4.12) has been mostly prevented, which would result in the formation of undesirable second phases, like $PbWO_4$ and $Pb_2FeWO_{6.5}$ phase [15]. Therefore, this B-site precursor method shows advantage in the preparation of pure PFW and PFW-PT compounds over the conventional direct mixed-oxide methods [16-18].

The ac impedance measurements of (1-x)PFW-xPT were carried out on a Solartron 1260 impedance analyzer combined with a Solartron 1296 dielectric interface, in the frequency range of 1 Hz to 1 MHz. The ceramic sample, with a size of 10 (diameter) x 1.0 (thickness) mm^2, was polished and painted with silver paste on both sides of the disk as electrodes. The sample was then dried at 160 °C for 2 hours before the impedance measurements in the temperature range of 100 - 600 K.

4.4 Results and Discussion

4.4.1 XRD Patterns

XRD patterns for the ceramic samples of (1-x)PFW-xPT (x = 0 to 0.8) are presented in Figure 4.3. It is found that PFW shows a pseudo-cubic perovskite structure at room temperature. When the PT content is increased to x = 0.25, the peaks (100) and (211) show a tendency to split, indicating the onset of phase transition from the pseudo-cubic to a tetragonal phase. With the further increase of PT content, all peaks, except peak (111), split, which clearly illustrates the composition (PT component) dependences of the perovskite structure.

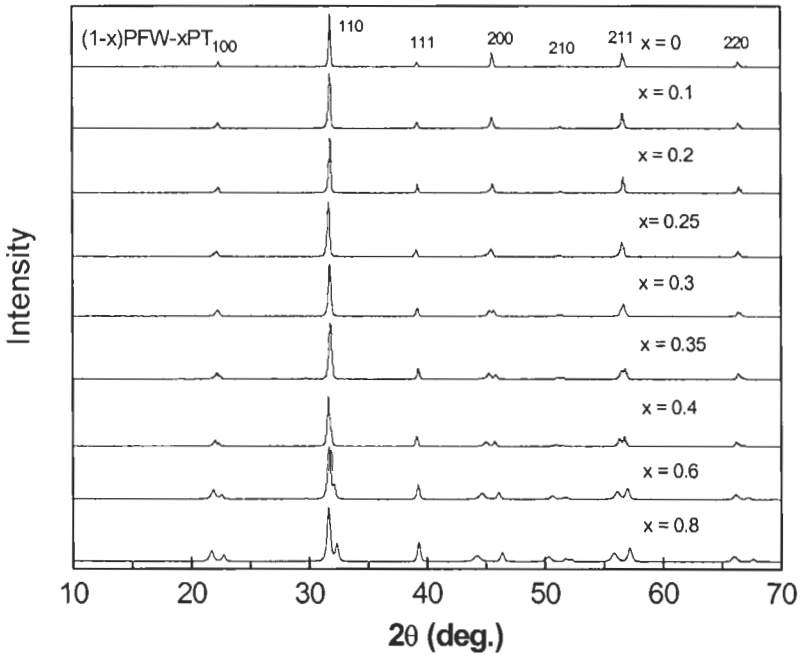

Figure 4.3: X-ray diffraction patterns for the various compositions of the (1-x)PFW-xPT ceramics at room temperature.

4.4.2 Dielectric Properties

Figure 4.4 shows the temperature dependence of the real dielectric permittivity at frequencies f = 1 kHz, 10 kHz, and 100 kHz, respectively, for the 0.90PFW-0.10PT ceramic. It exhibits a typical relaxor ferroelectric behaviour with a broad maximum and frequency dispersion around the temperature of dielectric constant maximum, T_m, which varies from 228 K at 1 kHz to 236 K at 100 kHz. With the increase of frequency, the maximum value of the dielectric constant decreases and T_m shifts to higher temperature.

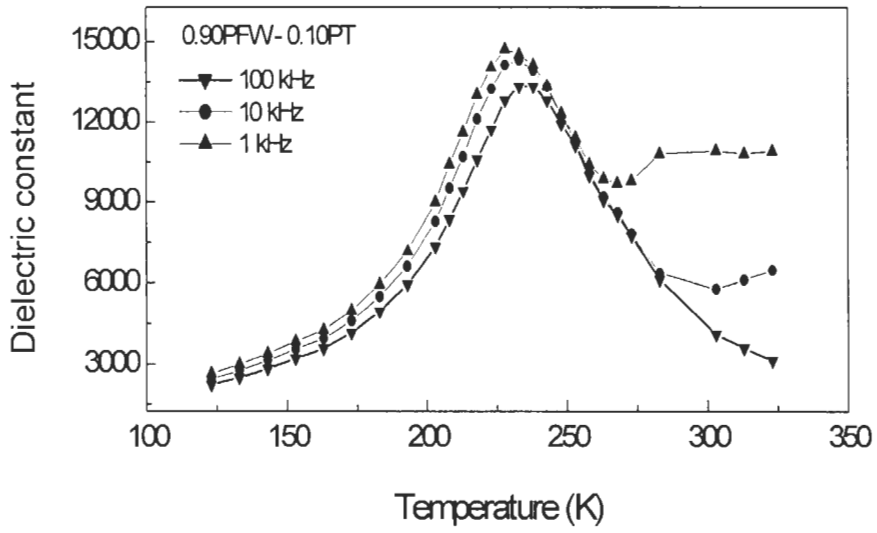

Figure 4.4: Dielectric constant vs. temperature at various frequencies for the 0.90PFW-0.10PT ceramics.

4.4.3 Impedance and Modulus Spectroscopic Analyses of the PFW-PT Ceramics

Figure 4.5 gives the complex impedance spectrum of the 0.90PFW-0.10PT ceramics in the form of resistivity at 293 K. ρ' and ρ" are the real part and imaginary part of the resistivity, respectively. It seems that the spectrum approximately consists of a distorted semicircle at high frequencies and a linear response at an angle of ~50° to the X-axis in low frequency range. The low-frequency 'spike' indicates that the diffusion of oxygen through the interfacial layer between the ceramics sample and the metal electrode is a semi-infinite diffusion process. This diffusion impedance is often called the Warburg diffusion impedance appearing on the surface layers [13]. The distorted and incomplete semicircle at high frequencies is possibly resulted from the overlap of some semicircles.

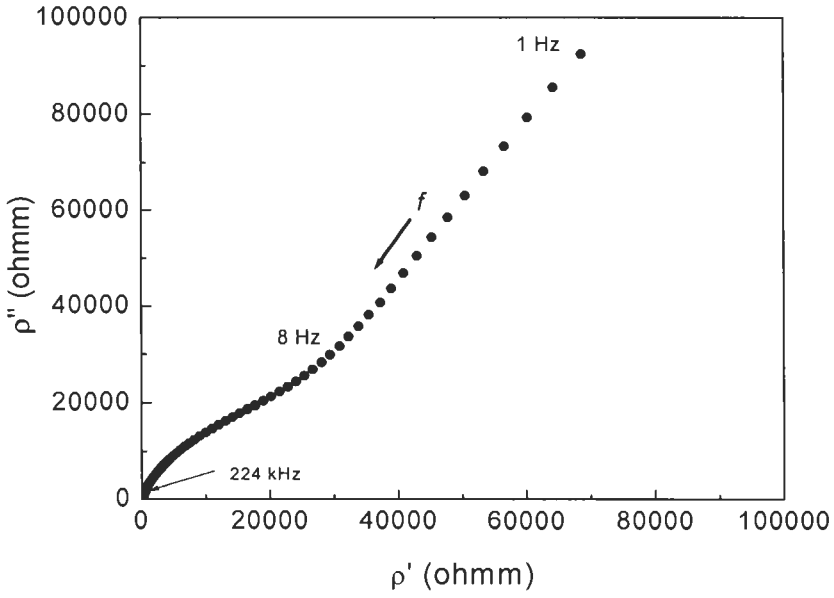

Figure 4.5: Complex impedance spectrum of the 0.90PFW-0.10PT ceramics at 293 K. Arrow indicates the direction of increasing frequency.

It is difficult to directly analyze and calculate each of the RC elements, because all the semicircles are merged into a depressed one. Therefore, an electric modulus analysis has to be performed here.

The corresponding electric modulus spectrum of the 0.90PFW-0.10PT ceramics is shown in Fig. 4.6. M' and M" represent the real and imaginary parts of the modulus, respectively. The spectrum is mainly composed of two semicircles in the middle frequency ranges and two other segments at lower and higher frequencies, respectively. Each part has individual electrical properties (R and C components) attributed by relevant component (phase) in the system. Clearly, the distorted semicircle in the impedance spectrum of Fig. 4.5 is indeed caused by the overlap of semicircles. In order to directly show the frequency dependence of the imaginary part of the modulus, M", and extract the capacitance values, the modulus spectrum in Fig. 4.6 is redrawn in terms of M" vs. frequency, as shown in Fig. 4.7. The maximal imaginary modulus, M''_{max}, for each peak of the plot is inversely proportional to the capacitance of each ceramic phase according to the following equation [10]:

$$M''_{max} = e_o / 2C \qquad (4.13)$$

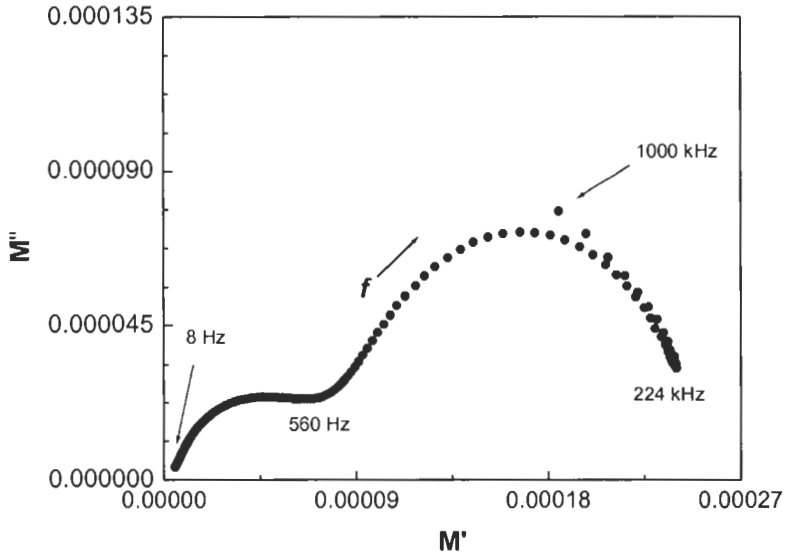

Figure 4.6: Electric modulus spectrum of the 0.90PFW-0.10PT ceramics at 293 K.

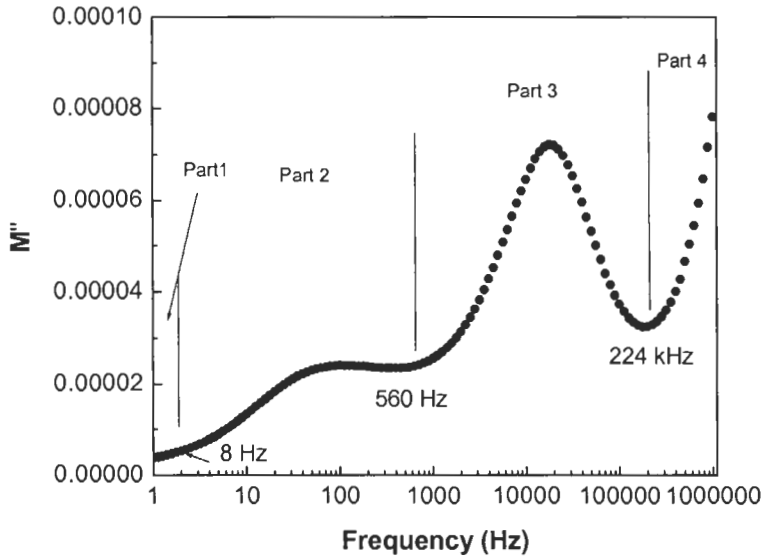

Figure 4.7: Imaginary modulus, M", plotted against frequency, for the 0.90PFW-0.10PT ceramics at 293 K.

The modulus spectrum M"(f) (Fig. 4.7) can be divided into four parts, according to the frequency responses of the modulus and impedance. In the low frequency range (part 1), the modulus M" gradually increases with the increase of frequency from 1 Hz to 8 Hz. This corresponds to the linear part of the impedance spectrum in Fig. 4.5, which can be associated with diffusion of oxygen through the electrode [13]. This Warburg diffusion impedance is related to the diffusion coefficient and concentration of the species. In the frequency range of 8 Hz - 560 Hz (Part 2), a small and broad modulus peak corresponding to the smaller semicircle in Fig. 4.6 is observed. According to Equation 4.13, the relevant magnitude of the capacitance, C, is found to be ~1.0 x 10^{-9} F, which is associated with a grain boundary phase in the polycrystalline material, since the grain boundary capacitance in electroceramics typically falls in the range of 10^{-11} to 10^{-8} F [11]. This relatively large value of grain boundary capacitance indicates the feature of the narrow intergranular regions (capacitance is inversely proportional to the thickness of the boundary) and the well-sintered properties of the PFW-PT ceramics [19]. In the third segment in the frequency range of 560 Hz - 224 kHz, a larger and sharper modulus peak appears at $f \approx$ 19.5 kHz, corresponding to a capacitance of ~ 3.0 x 10^{-10} F. It arises from the bulk (grain) phase of the ceramics, because a bulk phase exhibits a typical capacitance of 10^{-10}~10^{-9} F. The magnitudes of resistance of the grain boundary and bulk phases are ~3.0 x10^{6} ohms and ~1.0x10^{5} ohms, respectively, on the basis of Equation 4.7. These two resistances differ by ~30 times, while the relevant capacitances differ by only 3 times. This is the reason why only a single distorted semicircle can be seen in the complex impedance plane due to the domination of the impedance response by the very large resistance of the grain boundary phase. However, the separate semicircles can be

obtained in the corresponding electric modulus plane. For the last segment in the frequency range of 224 kHz-1000 kHz, as shown in Fig. 4.7 the modulus peak overflows with respect to the frequency scale of the instrumentation. A very small resistivity is estimated in this frequency range from the impedance plot in Fig. 4.5, where the high-frequency spectrum is close to the origin. Hence, a minor phase is possibly responsible for this electrical behaviour with a very small capacitance (very large M" in Fig. 4.7) and resistance [11]. This minor phase should be related to the structural defect and impurity in the ceramic system. For example, the charge defect in the form of Fe^{3+}/Fe^{2+} ions could promote the electron hopping between them, and thus affects the conductivity of the system and dielectric dispersion [15].

The corresponding equivalent circuit can be deduced from the impedance and modulus analyses above, as shown in Fig. 4.8. It results from a series model consisting of four parallel RC elements. R_g and C_g individually represent the resistance and capacitance of the dielectric bulk (grains) phase associated with the modulus M''_{max} in the frequency range of 560 Hz – 224 kHz. R_{gb} and C_{gb} are the resistance and capacitance of grain boundary phase, respectively, which corresponds to the M''_{max} in the frequency range of 8 Hz – 560 Hz. R_{ct} and C_{dl} are the charge transfer resistance and double-layer capacitance occurring at the sample-electrode interface, respectively. Z_w is the Warburg diffusion impedance as the oxygen ions diffuse through the electrode surface layer. R_m and C_m correspond to the resistance and capacitance of the minor phase due to the existence of structural defect and impurity in the system. It is clear that the conductance of the PFW-PT ceramics is composed of the four components connected in series, but their electrical contributions are different from each other. In most cases, the impedance

properties of bulk and grain boundary phases are given more attention in the studies of dielectric and ferroelectric ceramic microstructure, because of their major contribution to the dielectric properties.

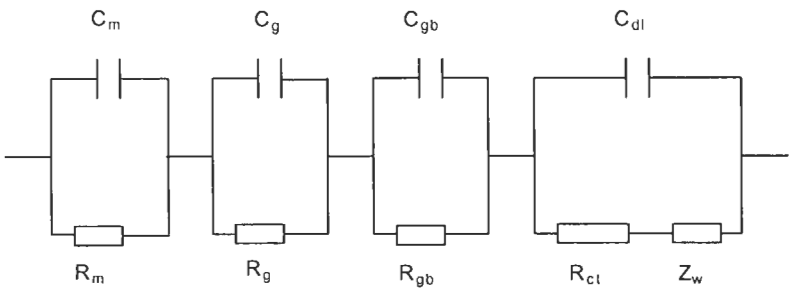

Figure 4.8. Equivalent circuit that describes the electrical response of the 0.90PFW-0.10PT ceramics. R_m and C_m stand for resistance and capacitance of the minor phase, respectively, R_g and C_g for those of the bulk (grain) phase, R_{gb} and C_{gb} for those of the grain boundary phase, R_{ct} and C_{dl} for those of charge transfer and double layer, and Z_w is for the Warburg diffusion impedance.

Figure 4.9 illustrates the resistivity of the 0.90PFW-0.10PT ceramics, as a function of frequency at 293 K. The resistivity decreases in a wavy form with the increasing frequency, demonstrating the influence of the capacitance impedance on the total resistivity of the system, because only the capacitance impedance, $Zc = -j/2\pi fC$, is frequency dependent. Each component has different capacitance impedance, which results in individual frequency dependence of the resistivity. In a ceramic system

composed of bulk and grain boundary components that are connected in series, the total complex resistivity, ρ_t, can be given by [13],

$$\rho_t = x_g\rho_g + x_{gb}\rho_{gb} \quad , \tag{4.14}$$

where ρ_g and x_g are the complex resistivity and volume fraction of the bulk phase, respectively. ρ_{gb} and x_{gb} are those of the grain boundary phase. The complex resistivity of each component (phase) is frequency-dependent, giving rise to the frequency dependence of resistivity of the system. The conductivity, $\sigma(\omega)$, is expressed as

$$\sigma(\omega) = \sigma_o + A\omega^n \quad , \tag{4.15}$$

where σ_o is a frequency-independent part, A is a constant, and n is a constant between 0 and1. Hence, the conductivity (resistivity) of the system increases (decreases) with increasing frequency.

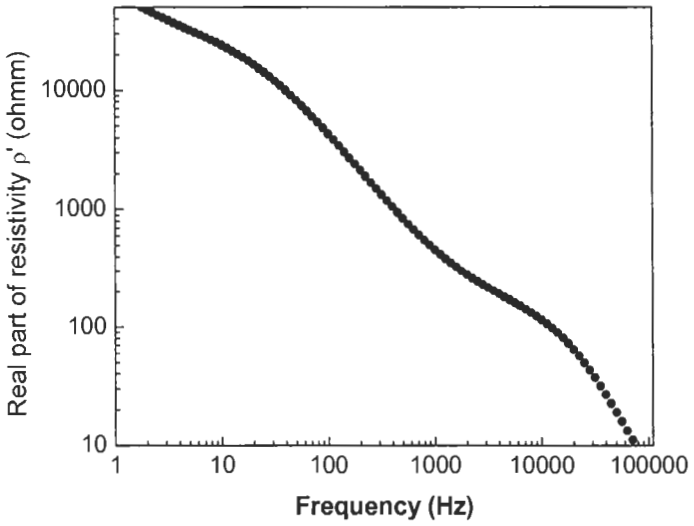

Figure 4.9: Frequency dependence of the real part of resistivity for the 0.90PFW-0.10PT ceramic at 293 K.

Figure 4.10 presents the imaginary parts of electric modulus (M") of the (1-x)PFW-xPT ceramics, with x = 0.10, 0.20, 0.25, and 0.325, as a function of frequency. The measurements were carried out at the temperatures above their Curie points. The modulus, M", for all compositions displays similar features with two distinguishable peaks related to the bulk phase at high frequencies and the grain boundary phase at low frequencies, respectively. They play an important role in making a contribution to the electric properties of the ceramic system (1-x)PFW-xPT.

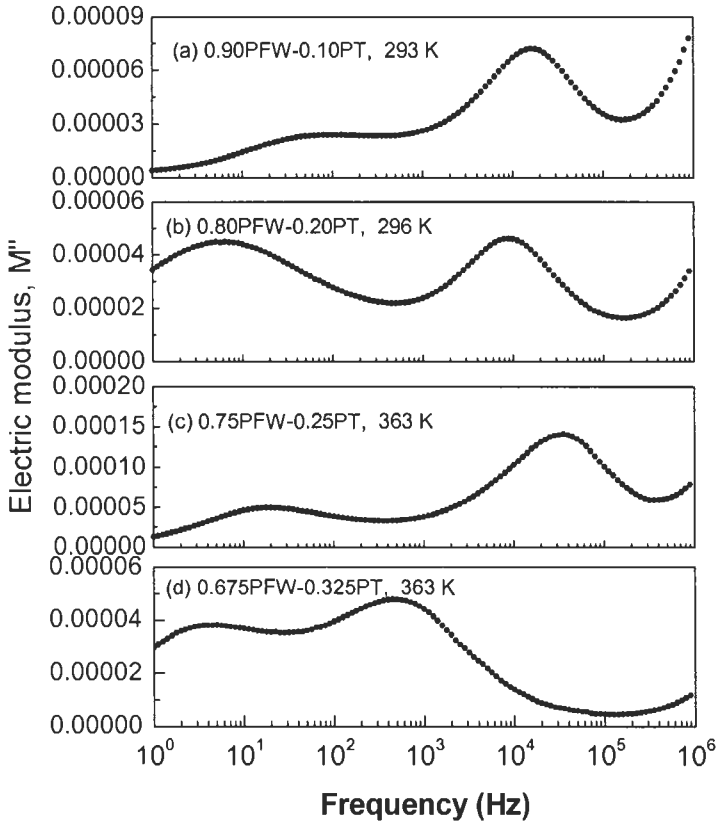

Figure 4.10: Frequency dependence of the imaginary part of electric modulus for (a) 0.90PFW-0.10PT at 293 K (T_C = 226 K), (b) 0.80PFW-0.20PT at 296 K (T_C = 275 K), (c) 0.75PFW-0.25PT at 363 K (T_C = 288 K), and (d) 0.675PFW-0.325PT at 363 K (T_C=350 K).

The influence of temperature on the electric modulus M" in the 0.75PFW-0.25PT ceramics is shown in Fig. 4.11. The electric modulus spectra with two peaks associated with grain boundary and bulk phases are clearly separated at high temperature, T = 363 K > $T_C \approx 288$ K. Since the modulus peak M''_{max} of the bulk phase at high frequencies is larger than that of grain boundary phase at low frequency, the corresponding capacitance value is smaller according to Equation 4.13 in which the capacitance is inversely proportional to maximum of imaginary modulus. Upon cooling to 303 K, the higher-frequency peak decreases rapidly and finally disappears, whereas the lower-frequency peak becomes broadened and shifts toward lower frequency. The high-frequency peak M''_{max} decreases much faster than the low-frequency peak M''_{max} in the temperature range of 363 K - 303 K. Therefore, the capacitance of the ceramic system is dominated by that

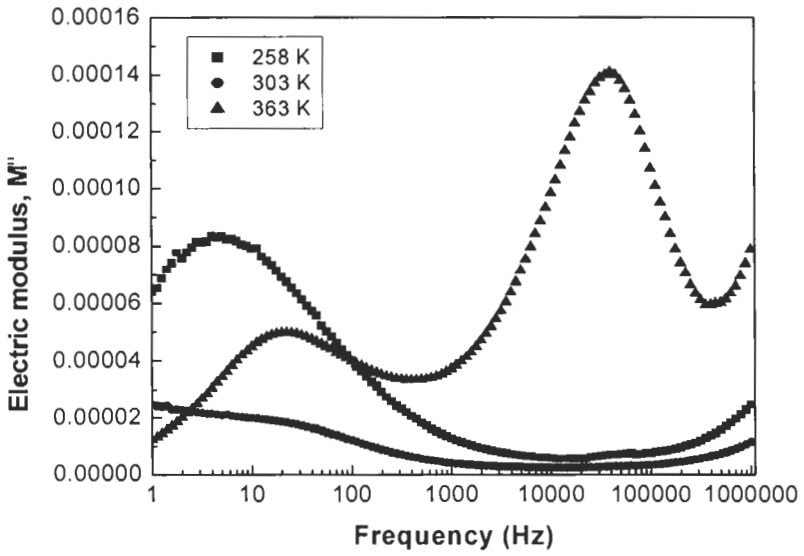

Figure 4.11: Frequency dependence of the modulus M" for the 0.75PFW-0.25PT ceramics at (a) 258 K, (b) 303 K, and (c) 363 K, respectively.

of the bulk phase. With the temperature decreasing to below the Curie point ($T = 258$ K < $T_C = 288$ K), the value of the whole electric modulus spectrum increases a bit, showing a decrease of the capacitance (or dielectric constant). The similar phenomenon also occurs in the 0.675PFW-0.325PT ceramics, as shown in Fig. 4.12, where the two modulus peaks are distinguishable at high temperature of 373 K ($>T_C \approx 350$ K), but the high-frequency modulus peak disappears at the temperature below T_C. The maximum of capacitance (or dielectric constant) occurs near the Curie temperature for these two systems. The temperature and frequency dependences of the modulus analyzed above are consistent with the dielectric and ferroelectric properties of the PFW-PT ceramics (see e.g. Fig. 5.5 and Chapter 3).

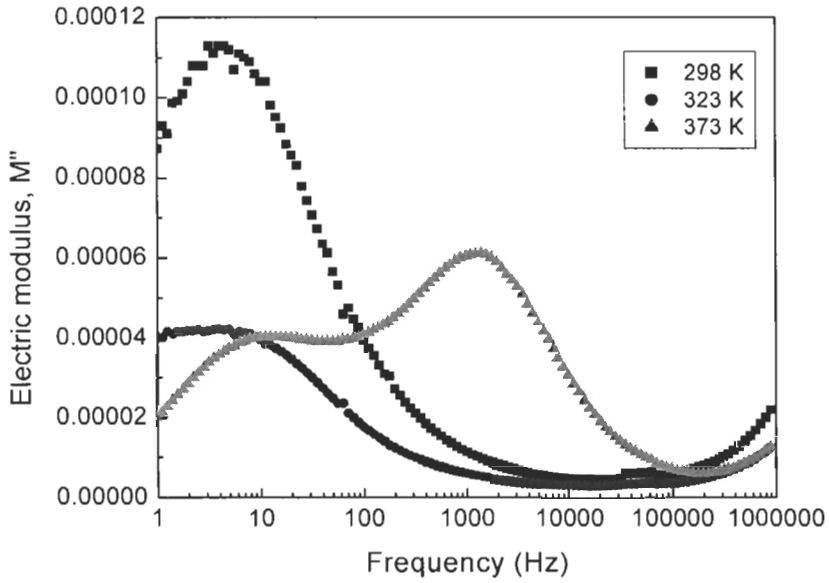

Figure 4.12: Frequency dependence of the modulus for the 0.675PFW-0.325PT ceramics at (a) 298 K, (b) 323 K, and (c) 373 K.

Since the electric modulus is inversely proportional to dielectric permittivity [13]:

$$\mathbf{M}^* = (\varepsilon^*)^{-1} \quad , \tag{4.16}$$

$$\varepsilon^* = \varepsilon' - j\varepsilon'' \quad , \tag{4.17}$$

where ε^* is the complex formalism of dielectric permittivity, and ε' and ε'' are the real and imaginary parts of ε^*, respectively. The electric modulus plot can be easily converted into the dielectric constant plot against the frequency. Figure 4.13 gives the frequency dependence of dielectric permittivity of the 0.90PFW-0.10PT ceramics at 293 K and 128 K, respectively. The real part of dielectric permittivity decreases nonlinearly with the frequency at the temperature above the Curie point ($T = 293\ K > T_C \approx 226\ K$), demonstrating a high-temperature frequency dispersion of the dielectric constant due to conductivity effects, as discussed in Chapter 3. On the other hand, the dielectric constant (ε') decreases slowly in the whole frequency range at a temperature far below the Curie point, as shown in Fig. 4.13b. This is because the frequency dispersion of the dielectric constant is greatly restricted by the freezing of the dipoles and the high potential barriers that give rise to a slowing down of the frequency responses of polar microdomains at low temperatures. The loss factor or $\tan\delta$ defined as the ratio of the imaginary part to the real part of dielectric permittivity, is also frequency dependent (dispersion) at high temperature. It is noticed that there are two peaks of loss factor near frequencies of ~9 Hz and ~10 kHz, respectively, as shown in Fig. 4.13a, which responds to a quick decrease of resistivity in Fig. 4.9. At the low temperature (Fig. 4.13b), the loss factor shows a monotonic increase with increasing frequency, which is rather normal behaviour for dielectric materials.

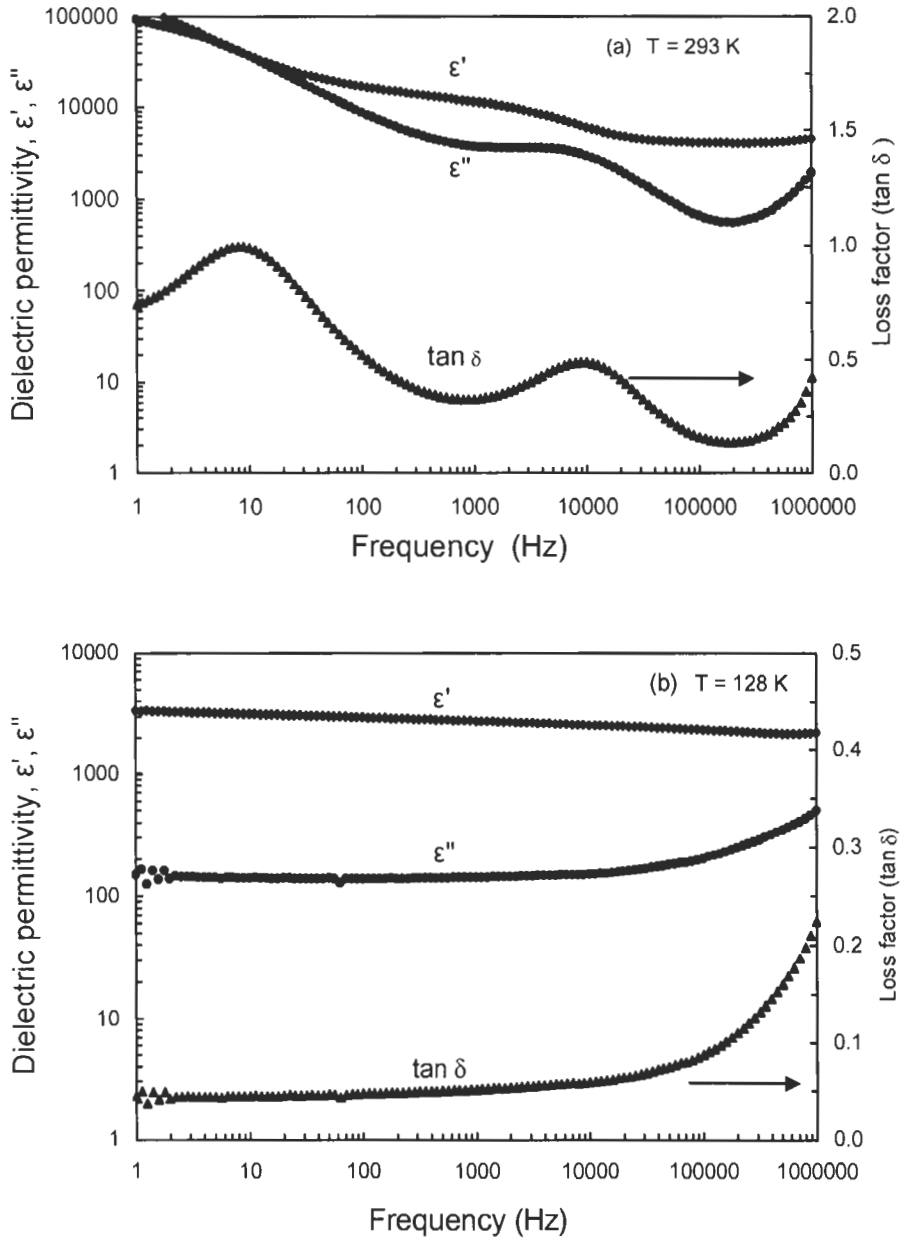

Figure 4.13: Frequency dependence of the dielectric permittivity and loss factor of the 0.90PFW-0.10PT ceramic at (a) 293 K and (b) 128 K, respectively.

4.5 Conclusions

The combined complex impedance and electric modulus formalisms have been successfully applied to analyze the electrical response of the (1-x)PFW-xPT ceramics (x = 0.10, 0.20, 0.25, and 0.325), and to reveal the electrical components (R and C) of each microstructural phase in the system, which contribute to the total electric properties of the solid solution ceramics.

It is found that four different microstructural phases: dielectric and ferroelectric bulk (grains), grain boundary, ceramics-electrode surface diffusion, and minor (structural defect and impurities) phase, contribute to the electrical properties of the (1-x)PFW–xPT ceramics. An equivalent circuit composed of the related RC elements has been presented to simulate and interpret the complex impedance and corresponding modulus spectra. The bulk (grains) and grain boundary phases are the main components making electrical contributions to the electric response of the ceramic system. The minor phase makes only a small electrical contribution to the system because of its very small resistivity.

The electric modulus spectra of 0.75PFW-0.25PT, in terms of imaginary part of the modulus vs. frequency, have been analyzed at 325 K, 303 K, and 258 K, respectively. The higher-frequency modulus peak M_{max}" corresponding the bulk (grains) phase is larger than the lower-frequency modulus peak referred to the grain boundary phase at the temperature far above the Curie point $T_C \approx 288$ K, indicating that the former has a smaller capacitance value than the latter. Upon cooling close to the Curie temperature, both the grain and grain boundary capacitances increase to their maximum values, showing the highest polar activities near the ferroelectric phase transition. The capacitance from the bulk phase increases more quickly than that from the grain

boundary phase. Hence, it is concluded that the dielectric and ferroelectric properties of the system are dominated by the bulk (grains) component.

The frequency dependences of the real and imaginary dielectric permittivity were measured for the 0.90PFW-0.10PT ceramics at the temperatures above and below T_C. The dielectric constant decreases significantly with increasing frequency at a temperature above T_C, demonstrating the high-temperature frequency dispersion. When the temperature is far below T_C, the dielectric constant changes slowly with the frequency, which is attributed to the dynamic freezing of the polar clusters and the attenuation of dipole relaxation. The resistivity and loss factor of the 0.90PFW-0.10PT ceramics at 293 K vary in a wavy form with the increasing frequency, which is related to multiple activation energies from the different phases in the system.

4.6 References

[1] L. E. Cross, *Ferroelectrics* **151**, 305 (1994).

[2] L. E. Cross, *Ferroelectrics* **76**, 241 (1987).

[3] Y.-J. Kim and S.-W. Choi, *Ferroelectrics* **186,** 287 (1996).

[4] M. Yonezawa, *Amer. Ceram. Soc. Bull* **62**, 1375 (1983).

[5] T. R. Shrout and A. Halliyal, *Amer. Ceram. Soc. Bull.* **66**, 704 (1987).

[6] Z.-G. Ye, K. Toda, M. Sato, E. Kita and H. Schmid, *Korean Phys. Soc.* **32,** S1028-31 (1998).

[7] G. A. Smolenskii, *J. Phys. Soc. Jpn. Suppl.* **28**, 26 (1970)

[8] G. Drazic, M. Trontel, and D. Kolar, *Mater. Sci. & Eng.* **B26**, 189 (1994).

[9] J. E. Bauerle, *J. Phys. Chem. Solids* **30**, 2675 (1969).

[10] B. Scrosati, *Electrochim. Acta* **26**, 1559 (1981).

[11] J. T. S. Irvine, D.C. Sinclair, A. R. West, *Adv. Mater.* **2**, 132 (1990).

[12] D. C. Sinclair and A. R. West, *J. Appl. Phys.* **66**(8), 3850 (1989).

1711 (1994).

[13] J. Ross Macdonald: *Impedance Spectroscopy*, A Wiley-Interscience Publication, New York 1987.

[14] O. Sakurai, K. Shinozaki, and N. Mizutani, *Trans. Mater. Res. Soc. Jpn.* **B14**,

[15] L. Zhou, P. M. Vilarinho and J. L. Baptista, *Mater. Res. Bulletin* **31**(6), 699 (1996).

[16] L. Zhou, P. M. Vilarinho, and J. L. Baptista, *J. Mater. Sci.* **33** 2673-77 (1998).

[17] G. A. Smolenskii, A. I. Agranovskaya, V. A. Isupov, *Sov. Phys. Sol. State* **1**, 907 (1959).

[18] M. Yonezawa, T. Ohno, in *Proceedings of the Japan – US Study Seminar on Dielectric and Piezoelectric Ceramics* **T-8**, 1(1982).

[19] P. G. Bruce, and A. R. West, *J. Electrochem. Soc.* **30**, 662 (1983).

[20] L. Feng and Z.-G. Ye, *J. Solid State Chem.* **163**, 484 (2002).

Chapter 5:
Growth and Electric Characterization of Relaxor Ferroelectric $Pb(Fe_{2/3}W_{1/3})O_3$ –$PbTiO_3$ [PFW-PT] Single Crystals

5.1 Introduction

Complex perovskite compound $Pb(Fe_{2/3}W_{1/3})O_3$ is a relaxor ferroelectric compound showing a broad and diffuse maximum of the dielectric permittivity at $T_m \approx$ 180 K with a strong frequency dispersion, and an absence of macroscopic polarization and anisotropy at temperatures far below T_m [1, 2]. This is attributed to the unusual chemical feature of the perovskite structure in which the A–sites are filled by Pb^{2+} ions and the octahedral B–sites are occupied by the Fe^{3+} and W^{6+} ions at random. On the other hand, PFW contains magnetic ions Fe^{3+} ($3d^5$) on the B–site with an occupancy of 66.7%. Magnetic ordering may occur upon cooling while the polar nanodomains form and develop [3].

Among the PFW–based systems, the solid solution between PFW and $PbTiO_3$ (PT) is of particular interest, because the relaxor ferroelectric and magnetic behaviour in PFW can be modified by the addition of the ferroelectric PT component. We recently studied the phase transitions in the ceramics and established the binary phase diagram for the (1-x)PFW–xPT solid solution system, which indicates the presence of a morphotropic phase boundary separating the rhombohedral (pseudo-cubic) from the tetragonal phase [2]. The magnetic hysteresis loop measurements of the PFW-PT ceramics revealed a

magnetodielectric coupling taking place near the temperature of dielectric constant maximum [4]. So far, all studies of the (1–x)PFW–xPT system have been carried out on the ceramic system which has potential applications in multilayered capacitors [5, 6].

Single crystals of the (1-x)PFW-xPT solid solution are expected to have superior dielectric/ferroelectric properties over the ceramic system because of their perfect and continued single crystal structure without heterogeneous phases such as grain boundaries. Unfortunately, the growth of the PFW-PT single crystals encountered some difficulties arising from the control of thermal and chemical parameters and from the volatilization of the solvent at high temperatures. Up to now, only the single crystals of PFW have been synthesized from high temperature solution growth and studied in terms of their optical, ferroelectric and magnetic properties [5, 7].

In this work, the single crystals of the (1-x)PFW-xPT solid solution, with x = 0, 0.07, 0.13, 0.17, 0.27 and 0.75, are successfully synthesized and characterized by X-ray diffraction and dielectric measurements.

5.2 Experimental

5.2.1 Growth of the (1-x)PFW-xPT Single Crystals

Single crystals of the (1-x)PFW-xPT solid solution are grown from high temperature solution using PbO as flux. PbO is an effective solvent for many oxides. In complex perovskite systems, it is also one of reactants, so that any contamination from foreign ions can be avoided when PbO is used as self-flux [8-10]. Table 5.1 lists the melting points of $Pb(Fe_{2/3}W_{1/3})O_3$ [6], $PbTiO_3$ [11] and PbO [12], which gives a reference to the determination of growth temperature of the (1-x)PFW-xPT single crystals.

Table 5.1: Melting points of $Pb(Fe_{2/3}W_{1/3})O_3$, $PbTiO_3$ and PbO compounds

Compounds	Melting point
$Pb(Fe_{2/3}W_{1/3})O_3$	~940 °C
$PbTiO_3$	1285 °C
PbO	886 °C

Starting chemicals, Fe_2O_3 (99.99%, Alfa), WO_3 (99.8%, Alfa), PbO (99.99%, Aldrich) and TiO_2 (99.99%, Aldrich), were weighed at the stoichiometric ratio of the (1-x)PFW-xPT solid solution based on the following reaction,

$$(1-x)Fe_2O_3+(1-x)WO_3+3xTiO_2+3PbO \rightarrow 3Pb[(Fe_{2/3}W_{1/3})_{1-x}Ti_x]O_3 \quad . \qquad (5.1)$$

About 30 grams of the chemicals, together with an excess of PbO (50wt%), were mixed and ground in an acetone media for half an hour before placed in a platinum crucible (30 cc) covered with a lid. Then, the Pt crucible was put in an alumina crucible that was sealed with Al_2O_3 cements around the lid. Such a double-crucible setting, as shown in Fig. 5.1a, was used to prevent the volatilization of PbO. Since the three-component phase diagram of the PFW–PT–PbO system is not available, the pseudo-binary PFW–PbO phase diagram [7] served as a reference to the ternary system for crystal growth. A preheating process was applied to test the melting point. With the increase of PT content, the soaking temperature (50 °C ~ 100 °C higher than the melting point) was increased accordingly due to the high melting point of PT (≈1285 °C). For example, it was 1010 °C, 1120 °C, 1150 °C, 1180 °C and 1230 °C for x = 0, 0.07, 0.13, 0.27, and 0.75, respectively. The preheated mixtures were held at the soaking temperature for 7-10 hours. A slow cooling was then proceeded at 1.0 ~ 2.0 °C/h down to 850 °C to promote the

nucleation and growth of the single crystals, followed by a final cooling to room temperature at 250 °C/h. Figure 5.1b shows the typical temperature profile used for the crystal growth. The solidified flux was leached out in hot HNO_3 aqueous solution (~0.5M). The residual PbO flux was further removed in an ultrasonic vibration bath to obtain clean PFW–PT single crystals.

(a)

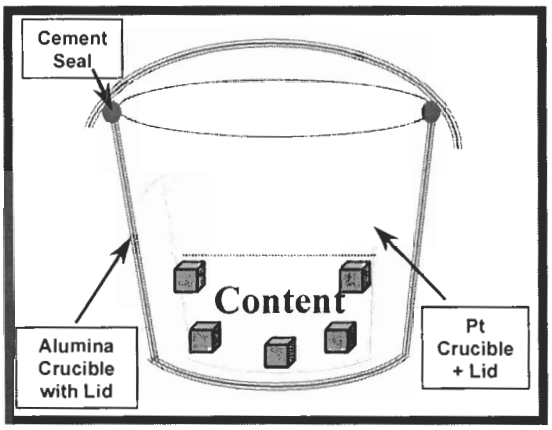

Alumina Sagger for Crystal Growth

(b)

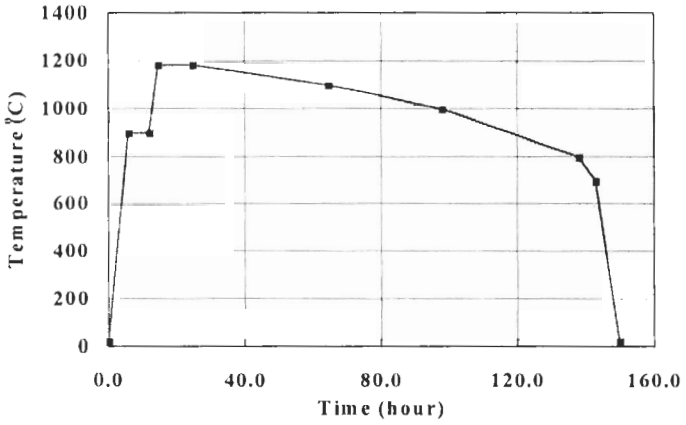

Crystal Growth Temperature Route

Figure 5.1: (a) Schematic of an alumina sagger for the PFW-PT crystal growth from high temperature solution and (b) the temperature profile for the crystal growth.

The crystal plates parallel to the $(001)_{cub}$ plane were polished using diamond pastes (#9 and #5), and then gold electrodes were sputtered on the plates using a Hummer 6-2 sputtering machine. The gold electrodes were connected to the dielectric analyzer by two gold wires. Figure 5.2 shows a sample of the crystal used for subsequent dielectric measurements. The dielectric measurements of the (1-x)PFW-xPT crystals were performed with an Alpha high-resolution dielectric/impedance analyser (NovoControl Broadband Dielectric Spectrometer) in a frequency range of $10 \sim 10^6$ Hz from 650 K to 100 K at 3-5 ^{o}C intervals. Ferroelectric loop measurements of the PFW-PT crystals were performed using RT66A standard ferroelectric testing system (Radiant.) combined with RT66A high voltage interface (HVI) based on the Sawyer-Tower circuit at the scanning rate of100 cycles/s.

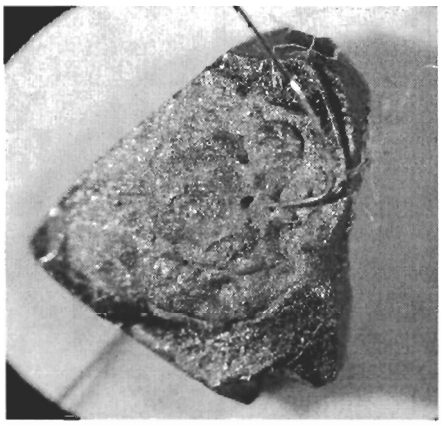

Figure 5.2: Photograph of a PFW-PT crystal with the Au electrode, showing the silver paste and Au wires on the surface of the crystal.

5.3 Results and Discussion

5.3.1 Morphology and XRD Characterization of the (1-x)PFW-xPT Single Crystals

Figure 5.3 depicts the samples of the (1-x)PFW-xPT (x = 0, 0.27 and 0.75) single crystals with different sizes. They are all black with semi-metallic luster. The small crystals (<1 mm) exhibit pseudo-cubic morphology (Fig. 5.3a & c). The larger crystals (3-5 mm) show a degenerated form (Fig. 5.3b & d), suggesting less stable conditions at late stages of the growth. The grown crystals show good quality and are suitable for subsequent structural and physical characterization.

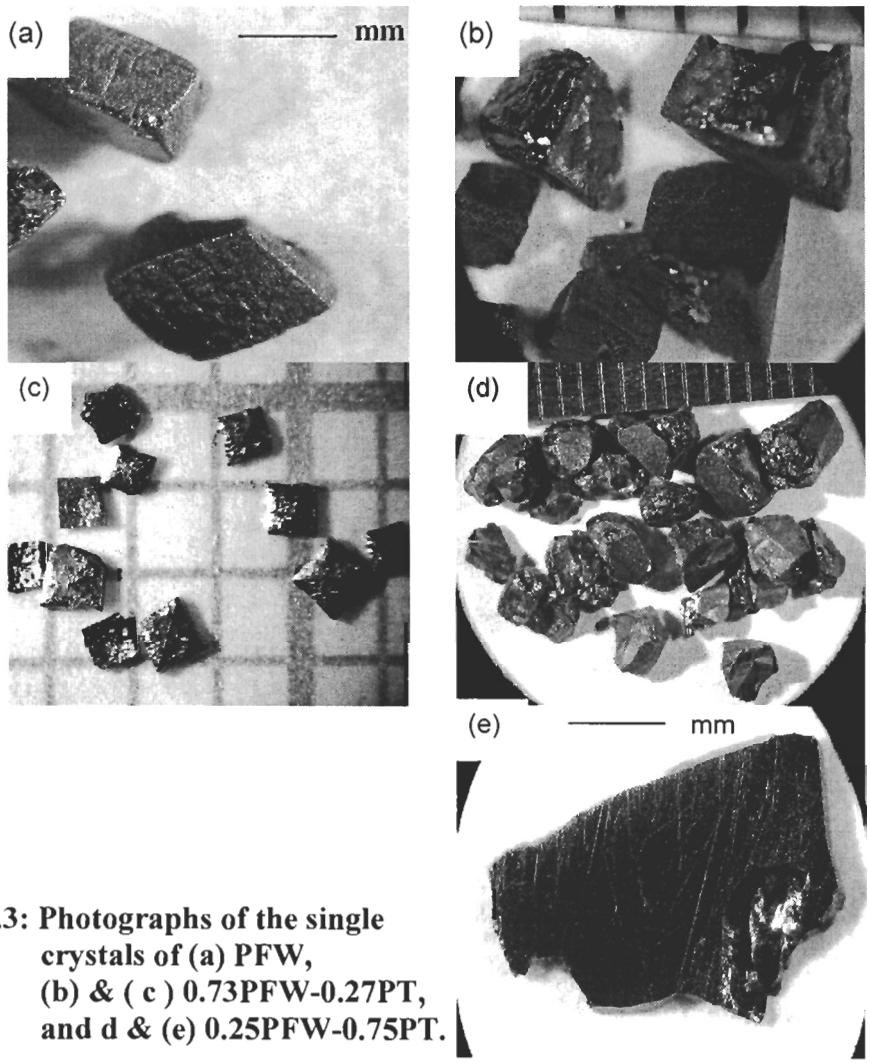

Figure 5.3: Photographs of the single crystals of (a) PFW, (b) & (c) 0.73PFW-0.27PT, and d & (e) 0.25PFW-0.75PT.

The phase and structure of the (1-x)PFW-xPT single crystals were characterized by X-ray diffraction (Rigaku diffractometer, Cu$K\alpha$ radiation, λ = 1.5418 Å) at room temperature. Figure 5.4 shows XRD patterns of the crushed crystals of (1-x)PFW-xPT, with x = 0, 0.13, 0.27 and 0.75. It is clear that PFW and 0.87PFW-0.13PT crystals have a pseudo-cubic perovskite phase at room temperature. As the PT content increases to 0.27, the (200), (211) and (220) peaks start to split (Fig. 5.4b), showing the onset of structure transition from the cubic to tetragonal one. In the XRD pattern of the 0.73PFW-0.27PT crystals, a very small peak at $2\theta = 28.60^{\circ}$ was found, which is related to the traces of the parasitic phase (a ferromagnetic phase of the hexagonal magnetoplombite "$PbFe_{12}O_{19}$"-type [7]) in the powder sample. It results from the inclusions of the magnetic phase and the composition inhomogeneity of the "magnetic" PFW crystal. In practice, the effect of the trace impurity phase on subsequent characterization of 0.73PFW-0.27PT is negligible. The 0.25PFW-0.75PT crystal exhibits a complete tetragonal phase with full split of the characteristic peaks. Such a structure variation with the PT content is in agreement with the phase diagram previously established for the (1-x)PFW-xPT binary ceramic system, as discussed on page 65 in Chapter 3.

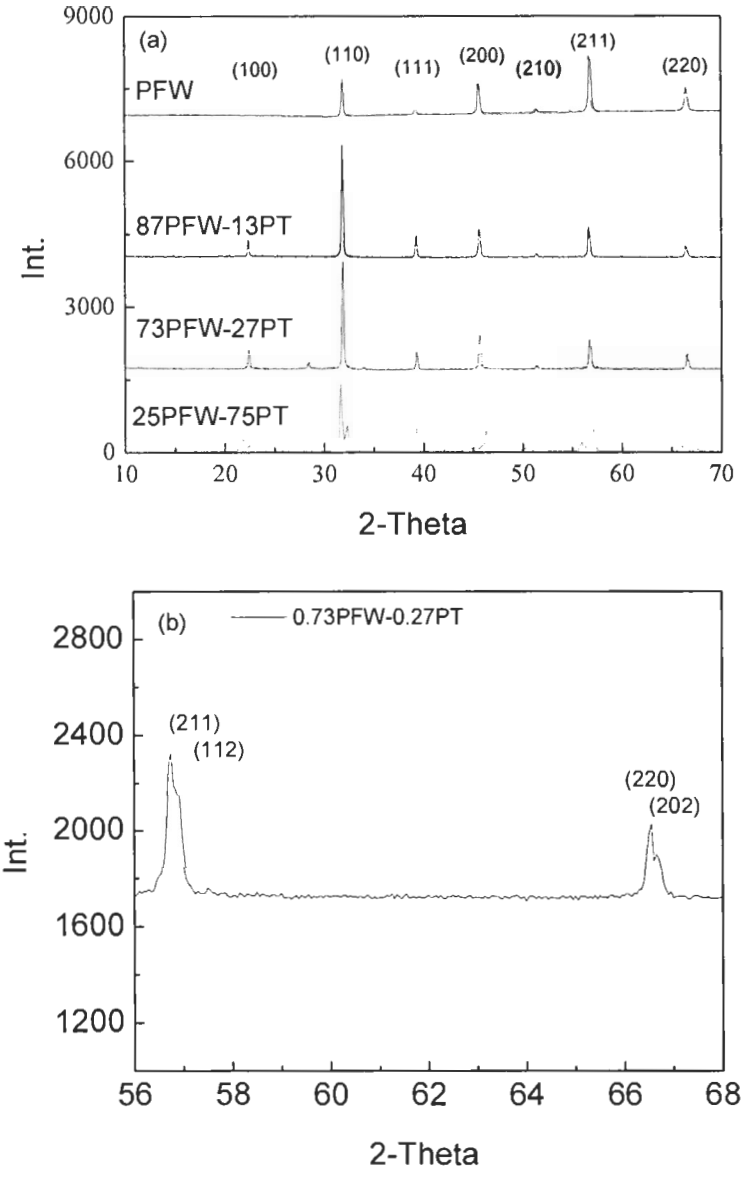

Figure 5.4: (a) X-ray powder diffraction of the (1-x)PFW-xPT single crystals, with x = 0, 0.13, 0.27, and 0.75, at room temperature, and (b) a part of XRD pattern of the 0.73PFW-0.27PT crystal in (a).

5.3.2 Dielectric Properties

Figure 5.5 displays the temperature dependence of the real part of dielectric permittivity for the (1-x)PFW-xPT crystals, with x = 0, 0.13, 0.17, 0.27 and 0.75. A broad and diffuse maximum of the dielectric permittivity with significant frequency dispersion is observed in Fig. 5.5a, b, c, and d, indicating typical relaxor ferroelectric behaviour. With the PT content increasing, the temperature (T_m) of maximal dielectric constant gradually shifts toward higher temperature (T_m = 185 K, 248 K, 267 K, 274 K and 603 K for PFW, 0.87PFW-0.13PT, 0.83PFW-0.17PT, 0.73PFW-0.27PT and 0.25PFW-0.75PT systems at 1 kHz, respectively) and the dielectric peaks become sharper, which exhibits an attenuation of the relaxor behaviour. In order to quantify the frequency dispersion of T_m, a parameter ΔT defined as $\Delta T = T_{m(1\ MHz)} - T_{m(1\ kHz)}$ is applied. Figure 5.6 illustrates the temperature difference, ΔT, as a function of the PT content. From the decreasing trend of ΔT, the ΔT will be zero at $x \geq 0.43$. Hence, the frequency dispersion of T_m will completely vanish at $x \geq 0.43$. This observation is consistent with that found in the PFW-PT ceramics system reported in Chapter 3 and in Ref. [13]. At high temperatures ($T > T_m$ or T_C), the dielectric constant increases and shows another kind of frequency dispersion in the crystals with $x \leq 0.27$, especially more significant at low frequencies (Fig5.5a, b, c, and d). The low-frequency dispersion can be attributed to the conductivity effect due to slowly mobile electronic charge. These charges arise from the Fe^{3+} ions, which are usually combined with Fe^{2+} ions to form charge defects. Thus, electron hopping between Fe^{3+} and Fe^{2+} ions results in an increase or decrease in conductivity, which in turn gives rise to the dielectric dispersion [2, 14]. The crystals with PT content $x \geq 0.43$, for example, 0.25PFW-0.75PT, exhibits a normal ferroelectric behaviour with a sharp permittivity peak at the temperature T_C = 603 K,

corresponding to the phase transition from a normal ferroelectric to paraelectric phase upon heating (Fig. 5.5e).

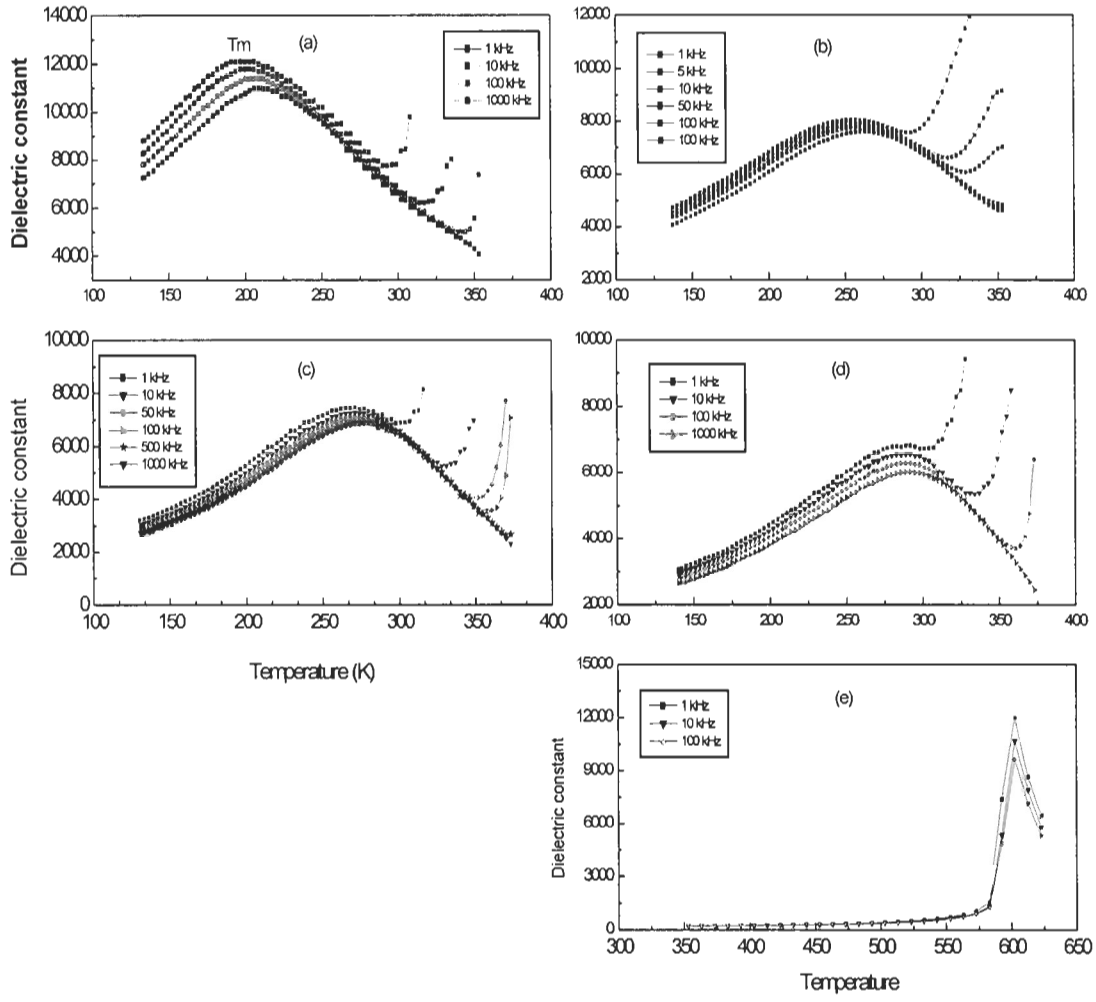

Figure 5.5: Temperature dependence of the dielectric constant at different frequencies for the PFW-PT crystals with various compositions, (a) PFW, (b) 0.87PFW-0.13PT, (c) 0.83PFW-0.17PT, (d) 0.73PFW- 0.27PT, and (e) 0.25PFW-0.75PT.

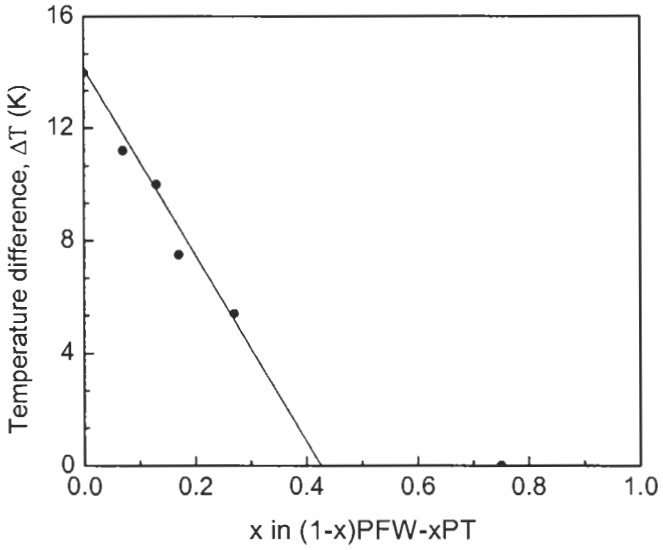

Figure 5.6: Frequency dispersion of T_m described in terms of the temperature difference $\Delta T = T_{m(100\ kHz)} - T_{m\ (1\ kHz)}$ of the crystal (1-x)PFW-xPT as a function of PT content x.

Table 5.2 gives the values of the dielectric dissipation factor (loss tangent) of the (1-x)PFW-xPT (x = 0, 0.27 and 0.75) single crystals measured at 10 and 100 kHz at room temperature and compares them to the ceramics (x = 0, 0.25 and 0.60) [2]. With the increase of PT content, the loss tangent decreases in both single crystals and ceramics. For the same or similar composition, however, the single crystals show a lower value of loss tangent than the ceramics. This indicates that the grown (1-x)PFW-xPT single crystals exhibit good quality with a better chemical stoichiometry than the ceramics, which reduces the concentration of charge carriers (mainly arising from defects and non-stoichiometry), and thereby improves the dielectric properties of the crystals.

Table 5.2. Dielectric dissipation factor (loss tangent) of the (1-x)PFW-xPT single crystals (SC) measured at 10 and 100 kHz at room temperature, compared to the ceramics.

	SC PFW	SC 0.73PFW-0.27PT	SC 0.25PFW-0.75PT	Ceramics PFW	Ceramics 0.75PFW-0.25PT	Ceramics 0.40PFW-0.60PT
100 kHz	0.018	0.027	<0.0008	0.261	0.028	0.021
10 kHz	0.067	0.037	<0.002	0.32	0.026	0.044

5.3.3 Vogel–Fulcher relationship

There have been various models proposed for the possible mechanism of dielectric relaxation and dispersive polarization behaviour in some relaxor ferroelectric systems [15-18].

In the dipole glassy-like model, a slowing down of dipole dynamics occurs, leading to the freezing of dipoles due to the size of the polar regions and potential barriers increasing upon cooling from temperatures above T_m to those below T_m. A broad and diffuse maximum of the dielectric constant from the paraelectric to dipole glass transition appears in the temperature dependence of dielectric constant because of a dynamic freezing. The dielectric relaxation can be described by the Vogel-Fulcher (V-F) equation (1.2) in terms of the AC frequency ω and the temperature of the maximal dielectric constant T_m.

Figure 5.7 is the reciprocal dielectric constant of the PFW crystal as a function of temperature for the purpose of fitting to the Curie-Weiss law according to Equation (1.1), $\varepsilon = C/(T-\theta)$. It is found that the linear relationship can be obtained only at temperatures (>270 K) far above T_m (~185 K). Therefore, the temperature dependence of the dielectric

constant of the PFW crystal does not obey the Curie-Weiss law for the description of simple ferroelectric behaviour.

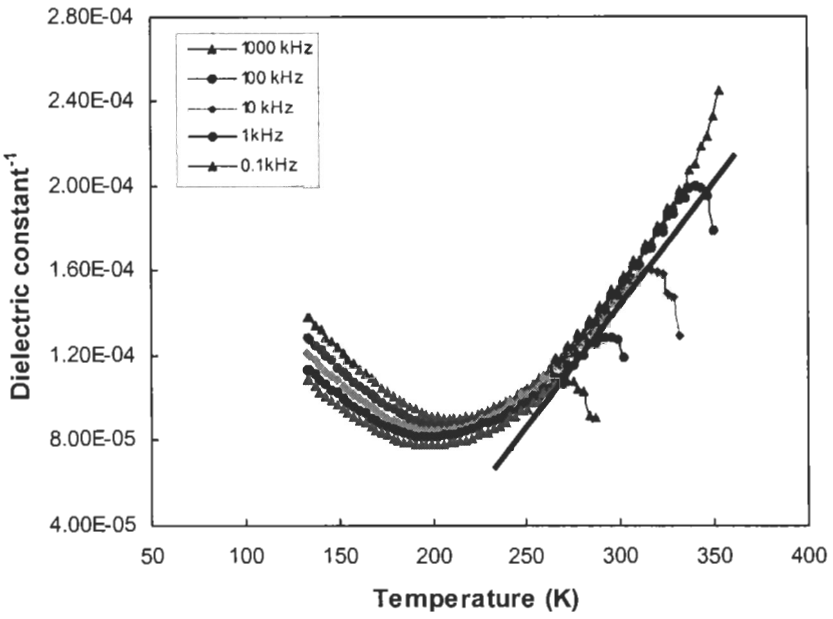

Figure 5.7: Reciprocal of dielectric constant as a function of temperature for the PFW single crystal at various frequencies.

The Vogel-Fulcher relationship (1.2) can be expressed in the following form:

$$1/(T_m\text{-}T_f) = -(K/E_a)\mathrm{Ln}(f) + (K/E_a)\ln(f_o) \quad , \qquad (5.2)$$

where T_f is the temperature of dynamic freezing of the polar clusters due to their interaction, f_o is a constant, E_a is the activation energy, and k is the Boltzman constant. A plot of $1/(T_m - T_f)$ vs. $\ln(f)$ is shown in Fig. 5.8 for the (1-x)PFW-xPT crystals, with x = 0, 0.07, 0.13, 0.17 and 0.27. A linear relationship between the natural logarithms of frequency and the reciprocal temperature difference in frequency range of 100 Hz ~ 1000 kHz was obtained. The data can be well fitted to the V-F law, indicating that the typical

relaxor ferroelectric behaviour in the PFW-PT system can be described by the glassy-like dipole relaxation and freezing mechanism [1, 19].

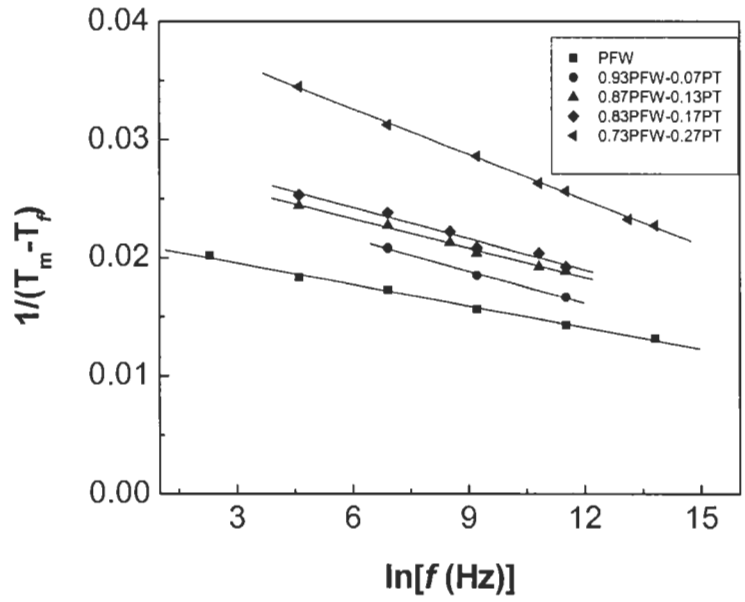

Figure 5.8: $1/(T_{m\,(100\ kHz)} - T_f)$ vs. Ln(f) for the (1-x)PFW-xPT crystal, with x = 0, 0.07, 0.13, 0.17 and 0.27. Solid lines show a linear fitting to the Vogel-Fucher relationship (5.4).

Table 5.3 gives the V-F equation fitting parameters, activation energy E_a, freezing point T_f, and temperature difference ($T_{m(100\ kHz)} - T_f$) for the crystals of (1-x)PFW-xPT, x = 0, 0.07, 0.13, 0.17, and 0.27. The activation energy needed for switching the dipole from one position to another opposite one tends to decrease with the increasing amount of PT component, which is in agreement with the characteristic of relaxor ferroelectric materials. The freezing temperature T_f increases with increasing PT content (T_f = 136 K, 157 K, 205 K, 226 K and 251 K for x = 0, 0.07, 0.13, 0.17 and 0.27, respectively), indicating that the temperature of the dynamic freezing of polar cluster, or glass

transition, gradually increases due to the enhanced correlation between dipole moments. The decrease of the temperature difference between T_m and T_f with the PT content increasing reveals that the relaxation behaviour gradually attenuates in the system. Since the size of the Ti^{4+} ion ($r \approx 0.605$ Å) is similar to the W^{6+} ion ($r \approx 0.60$ Å), but is smaller than the Fe^{3+} ion ($r \approx 0.645$ Å), the substitution of the Ti^{4+} ions for the Fe^{3+} and W^{6+} ions on the octahedral B-site is in favour of inducing the ferroelectric long-range order by increasing the correlation between dipole moments [1]. Hence, the transition into a glassy state with frozen random orientation of dipole moments weakens, making the freezing temperature increase. PFW has the lowest freezing temperature in the (1-x)PFW-xPT binary system. The increase of the freezing temperature was also found in the Mn doped PFW ceramics, because the formation of the defect pairs increases the correlation between the dipole moments [20].

Table 5.3: Vogel-Fucher law fitting parameters for the (1-x)PFW-xPT crystals.

Composition	E_a (ev)	T_f (K)	T_m-T_f at 100KHz
PFW	0.15	136	70
0.93PFW-0.07PT	0.1	157	60
0.87PFW-0.13PT	0.11	205	53
0.83PFW-0.17PT	0.11	226	49
0.73PFW-0.27PT	0.06	251	39

5.3.4 Induced Electric Polarization and Ferroelectric Hysteresis Loop

Macroscopic polarization in the relaxor ferroelectric (1-x)PFW-xPT crystals was also investigated by the application of an electric field. Figure 5.9 and 5.10 show the

induced polarization of (1-x)PFW-xPT, with x = 0 and 0.13, respectively, under an alternating electric field at different temperatures. The experiments were performed by measuring the electric displacement (polarization) as a function of the electric field with the help of a Sawyer-Tower circuit. It is seen that PFW shows a very small nonlinear polarization at room temperature (Fig. 5.9b), and a clear electric hysteresis loop (Fig. 5.9a) at 223 K. This macro polarization induced above the phase transition $T_m \approx 185$ K demonstrates the relaxor ferroelectricity of the PFW crystal. For the 0.87PFW-0.13PT crystal, two electric hysteresis loops were observed below and above the phase transition temperature ($T_m \approx 268$ K), as shown in Fig. 5.10. The remnant polarization and coercive electric field increase with decreasing temperature, showing a stronger ferroelectricity of the system at lower temperature. Compared with the results in Fig. 5.9, the larger ferroelectric hysteresis in Fig. 5.10 is attributed to the enhancement of the ferroelectric order due to the addition of the ferroelectric ion Ti^{4+} into the system.

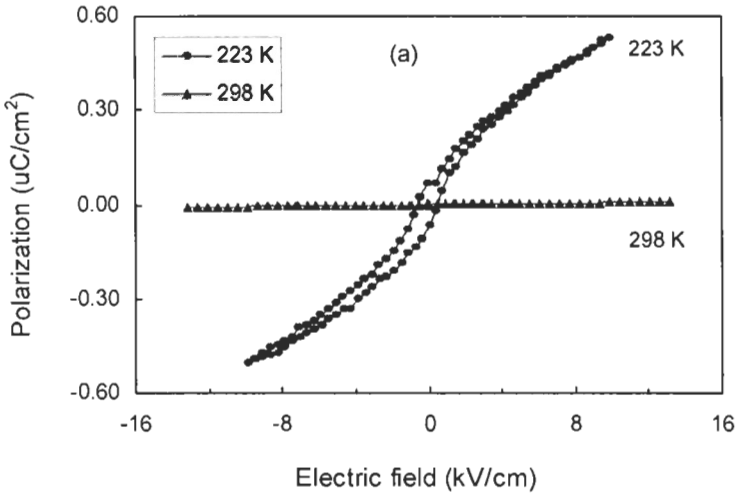

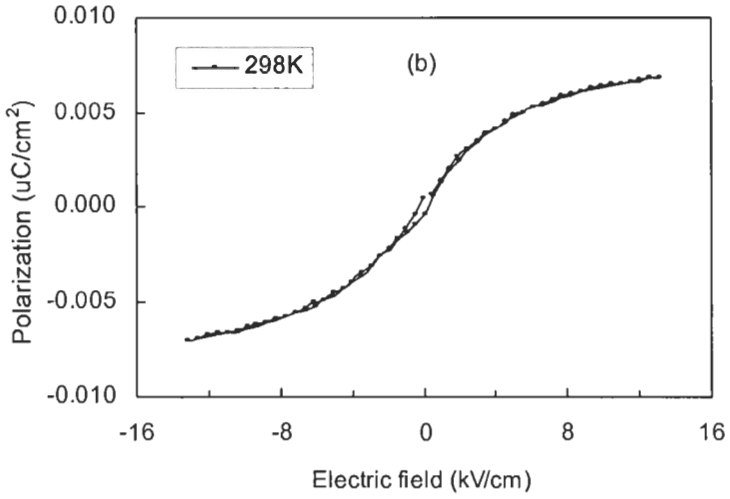

Figure 5.9: (a) Dielectric hysteresis loops of the PFW crystal at 223 K and 298 K, respectively, and (b) is the enlarged curve at 298 K.

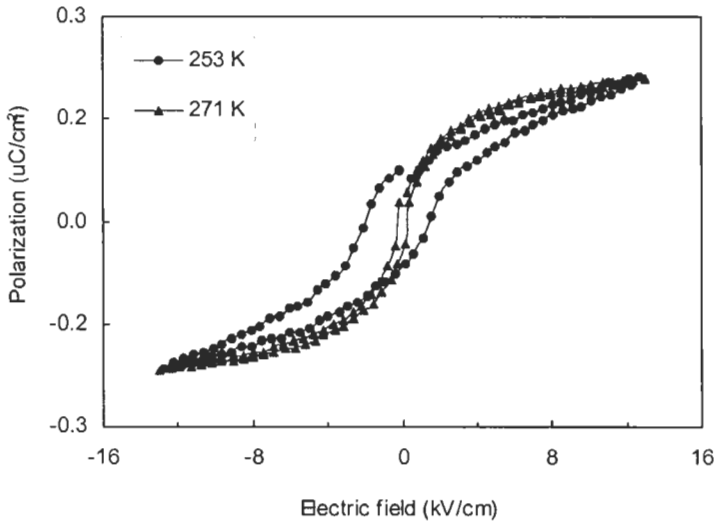

Figure 5.10: Dielectric hysteresis loops of the 0.87PFW-0.13PT crystal at 253 K and 271 K, respectively.

Figure 5.11 displays the polarization as a function of electric field for the crystal of (1-x)PFW-xPT, with x = 0, 0.13 and 0.27, at room temperature. The cyclic polarization

gave rise to the hysteresis loops in the 0.87PFW-0.13PT and 0.73PFW-0.27PT crystals, but a nonlinear polarization for PFW. The remnant polarization and coercive electric field are 0.14 $\mu C/cm^2$ and 0.50 kV/cm, respectively, for 0.73PFW-0.27PT, and 0.04 $\mu C/cm^2$ and 0.31 kV/cm, respectively, for 0.87PFW-0.13PT. With the increasing PT content, the macroscopic remnant polarization increases.

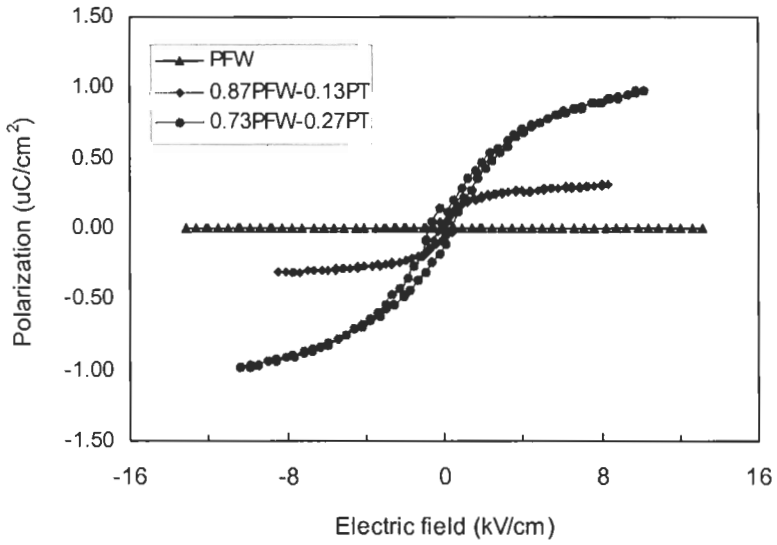

Figure 5.11: Induced dielectric polarization of the (1-x)PFW-xPT crystals, with x = 0, 0.13, and 0.27, at room temperature.

5.4 Conclusions

Single crystals of the (1-x)PFW-xPT solid solution, with x = 0, 0.07, 0.13, 0.17, 0.27 and 0.75, have been grown from the high temperature solution using PbO as flux, and characterized by X-ray diffraction and dielectric measurements. As the PT content x is increased to x = 0.27, the crystal structure at room temperature starts to change from a

pseudo-cubic to a tetragonal one, which is consistent with the phase diagram established previously for the ceramics (1-x)PFW-xPT system in Chapter 3.

The temperature and frequency dependences of the dielectric permittivity of the (1-x)PFW-xPT crystals show a crossover from the relaxor ferroelectric behaviour in low-content PT crystals ($x \leq 0.27$) to normal ferroelectric properties in high-content PT crystals ($x > 0.27$). The frequency-dispersive dielectric constant maxima arising from the relaxor behaviour can be well fitted to the Vogel-Fulcher (V-F) law. With the PT content increasing, the glassy-like behaviour with frozen random orientation of dipole moments attenuates due to the enhanced correlation between dipole moments. The grown crystals show improved dielectric properties with much smaller loss tangent than the ceramics at room temperature.

The macroscopic polarization in the (1-x)PFW-xPT crystals, $x = 0$, 0.13, and 0.27, induced by the application of an electric field has been measured at different temperatures. Non-linear polarization and a slim electric hysteresis loop at the temperatures above T_m further reveals the relaxor ferroelectric behaviour of the PFW crystal. With the PT content increasing, the macroscopic remnant polarization increases at room temperature, demonstrating the enhanced ferroelectricity in the PFW-PT system.

5.5 References

[1] Z.-G. Ye, *Key Eng. Mater.* **155 – 156**, 81 (1998).

[2] L. Feng and Z.-G. Ye, *J. Solid State Chem.* **163**, 484 (2002).

[3] Z.-G. Ye, K. Toda, M. Sato, E. Kita and H. Schmid, *J. Korean Phys. Soc.* **32**, S1028

(1998).

[4] L. Miliana, D. Marré, A. S. Siri and P. Nanni, *Appl. Phys. Lett*. **83**, 5509 (2003).

[5] Z.-G. Ye and H. Schmid, *Ferroelectrics* **162**, 119 (1994).

[6] T. R. Shrout and A. Halliyal, *Am. Ceram. Soc. Bull*. **66**, 704 (1987).

[7] Z.-G. Ye, H. Schmid, *J. Crystal Growth* **167**, 628 (1996).

[8] I. H. Brunskill, R. Boutellier, W. Depmeier, H. Schmid and H. J. Scheel, *J. Crystal Growth* **56**, 541 (1982).

[9] W. Brixel, R. Boutellier, W. Depmeier, H. Schmid and H. J. Scheel, *J. Crystal Growth* **82**, 396 (1982).

[10] Z.-G. Ye, P. Tissot and H. Schmid, *Mater. Res. Bull* **25**, 739 (1990).

[11] M. A. Eisa, M. F. Abadir, and A. M. Gadalla, *Trans. J. Br. Ceram. Soc*. **79**, 100 (1980).

[12] R. F. Geller and E. N. Bunting, *J. Research Nat. Bur. Standards* **18**, 585 (1937).

[13] Y. –J. Kim and S.-W. Choi, *Ferroelectrics* **186**, 287 (1996).

[14] Z. Li, A. Wu, P. M. Vilarinho and I. M. Reaney, *J. Phys.: Condens. Mater* **17**, 2167 (2005).

[15] Z. G. Lu and G. Calvarin, *Mater. Res. Bull*. **31**, 445 (1996).

[16] D. Viehland, J. –F. Li, S. J. Jang, E. Cross and M. Wuttig, *Phys. Rev. B* **46**, 8013 (1992).

[17] D. Viehland and J. F. Li, *J. Appl. Phys*. **75**, 1705 (1994).

[18] N. Yasuda, S. Fujimoto and K. Tanaka, *J. Phys. D: Appl. Phys*. **18**, 1909 (1985).

[19] L. E. Cross, *Ferroelectrics* **76**, 241 (1987).

[20] L. Zhou, P. M. Vilarinho and J. L. Baptista, *J. Mater. Sci.* **33**, 2673 (1998).

Chapter 6:
Magnetic Ordering in (1-x)$Pb(Fe_{2/3}W_{1/3})O_3$-x$PbTiO_3$ [(1-x)PFW-xPT] Single Crystals

6.1 Introduction

$Pb(Fe_{2/3}W_{1/3})O_3$ is an unusual member of the complex perovskite family of compound, which shows both relaxor ferroelectric behaviour and magnetic ordering. The octahedral B-sites of the ABO_3 unit cell are occupied with paramagnetic Fe^{3+} and non-magnetic W^{6+} ions at random. On the nanoscopic scale, polar nanoregions (or clusters) are expected to exist due to compositional fluctuations and partial order/disorder. Therefore, a broad and diffuse maximum of dielectric permittivity occurs at around $T_m \approx$ 178 K, accompanied with strong frequency dispersion on the temperature dependence of the dielectric constant [1, 2]. The dispersive maximum of dielectric constant is not related to any structural changes, the perovskite material remaining in a pseudo-cubic structure down to very low temperature [3].

On the other hand, the paramagnetic ions Fe^{3+} ($3d^5$) on the octahedral B-site with an occupancy of 66.7% in the perovskite structure may give rise to the magnetic ordering upon cooling while the polar nanodomains develop. Most studies on $Pb(Fe_{2/3}W_{1/3})O_3$ (PFW) and $Pb(Fe_{2/3}W_{1/3})O_3$–$PbTiO_3$ (PFW-PT) systems have been related to the dielectric and ferroelectric properties, while few attempts were made to investigate their magnetic properties in order to understand the magnetic ordering and to explore the

possible magnetoelectric (ME) coupling effect [2-4]. In the ME coupling effect, an electric (magnetic) field may induce not only electric polarization (magnetization), but also magnetization (electric polarization) [5, 6]. The magnetism and ferroelectricity are involved with local spin arrangement and off-centre structural distortions, respectively [7-9]. The intrinsic relationships among the magnetic ordering, ferroelectric relaxation, composition and structure are expected to exist in this system, which have not been thoroughly understood yet.

Smolenskii *et al.* [10] first reported the antiferromagnetic ordering appearing at 363 K in the PFW ceramics by magnetic and neutron-diffraction measurements. Later, Al'shin [11] found that there are two Curie-Weiss regions below T_N = 383 K. Below 10 K, the magnetic susceptibility drops, presumably as a result of a "full antiferromagnetic ordering". Uchino [12] investigated the magnetic field dependence of magnetization of the (1-x)$Pb(Fe_{2/3}W_{1/3})O_3$-x$Pb(Co_{1/2}W_{1/2})O_3$ system above the liquid nitrogen temperature, and suggested that the slight deviation from the theoretical curve in the phase diagram is caused by the partial Fe^{+3} ions participating in magnetic co-operative ordering based on the hypothesis of Goodenough *et al.* [13, 14], according to which a magnetic ion that has no magnetic neighbours or only one magnetic neighbour does not take part in magnetic ordering. Similar results were also obtained in PFW on the basis of the non-saturated magnetization at low temperature (10 K), suggesting that not all the magnetic moments participate in the ordering [15]. Ye *et al.* [2] found that two types of magnetic orderings take place in the PFW single crystals at T_{N1} = 350 K and T_{N2} = 20 K, respectively, based on the temperature dependence of the magnetization. The high-temperature magnetic ordering at 350 K was suggested to arise from a superexchange in the Fe/W disordered

regions through the – Fe^{3+} – O – Fe^{3+}– pathway, and the low-temperature one at 20 K from a superexchange of the – Fe^{3+} – O – W – O – Fe^{3+} – pathway in the Fe/W ordered nanoregions of the perovskite structure [2]. In the (1-x)PFW–xPT ceramic system, Mitoseriu *et al.* [3, 16, 17] found a small shift of low-temperature magnetic transition (T_{N1}) towards higher temperature and the high-temperature transition towards lower temperature with the increasing amount of PT component. Unfortunately, no detailed or satisfactory explanation was given.

Some phenomena related to magnetoelectric coupling effects were also reported. A very slight deviation of the magnetization from linearity in the temperature interval of dielectric relaxation around T_m = 175 K was observed [2], which was suggested to be associated with the effect of electric field on the magnetic ordering in the PFW crystal. A small anomaly of the magnetic hysteresis loop near the T_m of the PFW ceramics was suggested to indicate a magnetoelectric coupling [13]. However, a pronounced interplay between the electric and magnetic properties is not easily observed because of the very weak coupling effect between them [16]. It is necessary to prove the weak magnetoelectric effect by more detailed and accurate measurement techniques

Up to now, there still lacks the systematic studies on the (1-x)PFW–xPT systems, especially the magnetic properties of the single crystals of the solid solution. In this chapter, the magnetic properties of the single crystals of the (1-x)PFW–xPT solid solution, with x = 0, 0.07, 0.27 and 0.75, are studied with SQUID magnetometric measurements.

6.2 Experimental

Single crystals of the (1-x)PFW–xPT solid solution were grown from high temperature solution using PbO as self-flux, as described in chapter 5. A more detailed description of the crystal growth can be found in Chapter 5. The starting chemicals, Fe_2O_3 (99.99%, Alfa), WO_3 (99.8%, Alfa), PbO (99.99%, Aldrich) and TiO_2 (99.99%, Aldrich), were mixed at the stoichiometric ratios of the (1-x)PFW–xPT solid solution according to the following reaction,

$$(1\text{-}x)Fe_2O_3+(1\text{-}x)WO_3+3xTiO_2+3PbO \rightarrow 3Pb[(Fe_{2/3}W_{1/3})_{1\text{-}x}Ti_x]O_3 \quad , \qquad (5.1)$$

with x = 0, 0.07, 0.27, and 0.75. The mixtures, together with an excess of PbO (50wt%), were ground in an acetone media for half an hour before being placed in a platinum crucible covered with a lid. The Pt crucible was then put in an alumina crucible that was sealed to an alumina lid with Al_2O_3 cements. Such a double-crucible setting was used to prevent the volatilization of PbO. Since the three-component phase diagram of the PFW–PT–PbO system is not available, the pseudo-binary PFW–PbO phase diagram [18] served as a reference to the ternary system for the crystal growth. A preheating process was carried out to test the melting point. It was found that the melting point of the system increases with the increasing PT content because of the high melting point of PT (~1265 ^{o}C). Therefore, the mixtures of different compositions were heated to a higher soaking temperature (about 50 ^{o}C ~ 100 ^{o}C above the melting point) with the increasing PT content, i.e. 1010 ^{o}C, 1120 ^{o}C, 1180 ^{o}C and 1230 ^{o}C for x = 0, 0.07, 0.27, and 0.75, respectively, and held for 7 hours. A slow cooling process then took place at 1.0 ~ 2.0 ^{o}C/h down to 850 ^{o}C to trigger the nucleation and to promote the growth of the single crystals, followed by a final cooling down to room temperature at 250 ^{o}C/h. The solidified flux was leached out in hot and diluted HNO_3 aqueous solution. The residual

PbO flux was further removed in an ultrasonic vibration bath to obtain clean PFW–PT single crystals.

The magnetic measurements were performed on a Superconducting QUantum Interference Device (SQUID) magnetometer (Quantum Design, MPMS XL-7 Ever Cool). At first, the sample (0.020~0.070 grams) was heated to 373 K to eliminate any absorbed H_2O traces. The magnetization of the crystals was then measured upon magnetic field heating (FH) at 50 Oe and 1 kOe applied along $<100>_{cub}$, respectively, after zero field cooling (ZFC) down to 2 K, at the temperature intervals of 2 ~ 5 degrees. Ac magnetization measurements were carried out with a small ac magnetic field of 5 Oe and at frequencies of 10 Hz and 1 kHz, respectively.

6.3 XRD of the Single Crystals

The phase and structure of the (1-x)PFW–xPT crystals were characterized by X-ray powder diffraction (Cu Kα radiation, λ = 1.5418 Å). Figure 6.1 shows the XRD patterns of the ground (1-x)PFW-xPT crystals, with x = 0, 0.07, 0.27 and 0.75. The PFW and 0.93PFW-0.07PT crystals show a pseudo-cubic perovskite structure at room temperature. As the PT content is increased to 0.27, the (200), (211) and (220) peaks start to show a tendency to splitting, indicating the onset of phase transition from the cubic to a tetragonal structure. The crystals of 0.25PFW-0.75PT exhibit a complete tetragonal phase with full split of the characteristic peaks, except the (111) peak. This structural change as a function of the PT content is in agreement with the phase diagram we recently established for the (1-x)PFW-xPT solid solution ceramic system, as described in Chapter 3 and in Ref [19].

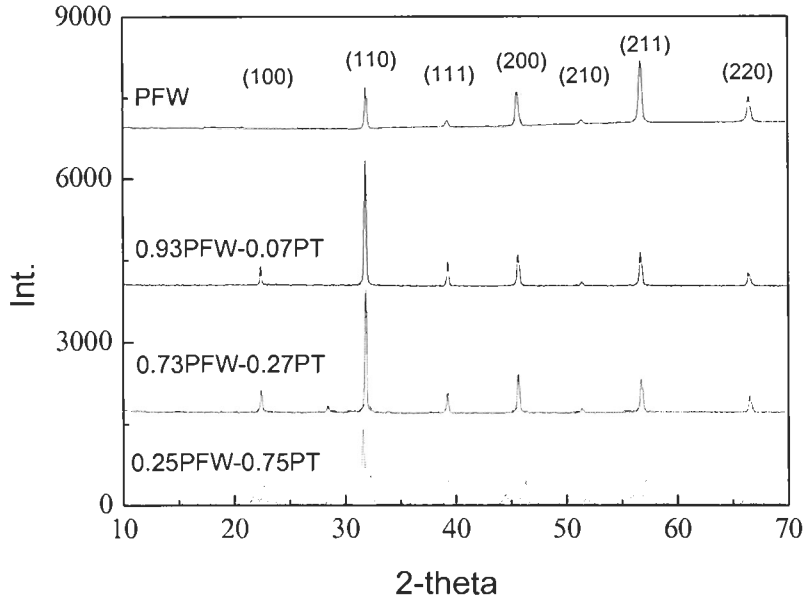

Figure 6.1: X-ray powder diffraction patterns of the (1-x)PFW-xPT single crystals, indicating a rhombohedral (pseudocubic) phase for low PT-contents and a tetragonal splitting for x > 0.27

6.4 Results and Discussion

6.4.1 Magnetic properties

Figure 6.2 presents the temperature dependence of the magnetization of the (1-x)PFW–xPT crystals, with x = 0, 0.07, 0.27 and 0.75, at a magnetic field heating of 50 Oe after zero field cooling. Upon heating from 2 K, a magnetization peak appears at the Néel temperature of T_{N1} = 8.5 K for PFW, which indicates a magnetic transition from a (weakly) ferromagnetic state to an antiferromagnetic phase. With the temperature further increasing, the magnetization gradually decreases and shows a high-temperature magnetic anomaly at T_{N2} = 370 K, which is attributed to the antiferromagnetic-to-paramagnetic transition. This transition is more clearly observed in Fig. 6(b) and (c).

These two types of magnetic orderings can be explained in light of the magnetic interactions proposed in Ref. [2] for the PFW single crystals. The weakly ferromagnetic ordering at low temperature arises from a superexchange of dominantly AFM-type (see subsection 6.4.1) in the Fe/W ordered nanoregions through the – Fe^{3+} – O – W – O – Fe^{3+} – pathway, while the one at high temperature results from a superexchange of the –Fe^{3+} – O – Fe^{3+} – pathway in the Fe/W disordered nanoregions. Since the magnetic interaction distance (~ 4.0 Å) between the adjacent Fe^{3+} ions in the disordered regions is shorter than that (~8.0 Å) in the ordered ones, the corresponding magnetic coupling within the disordered regions is stronger and can be stabilized at a higher temperature.

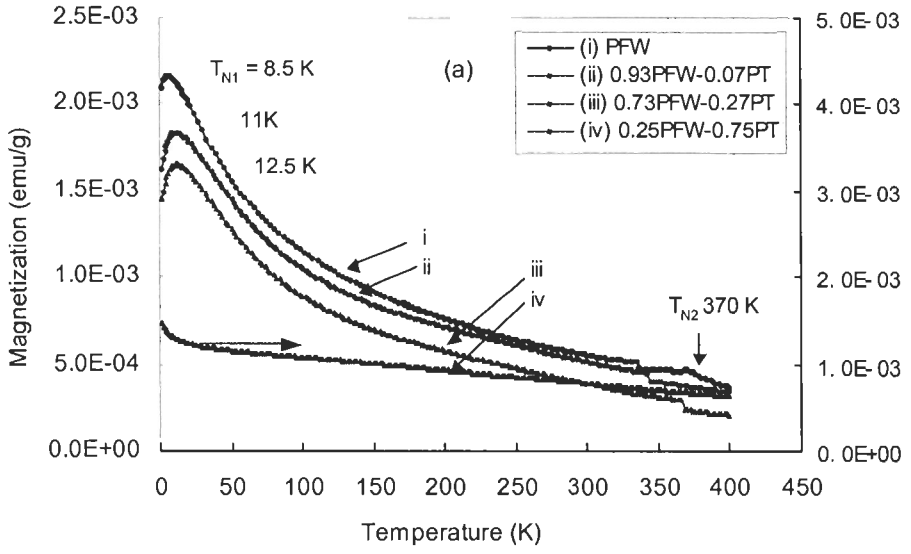

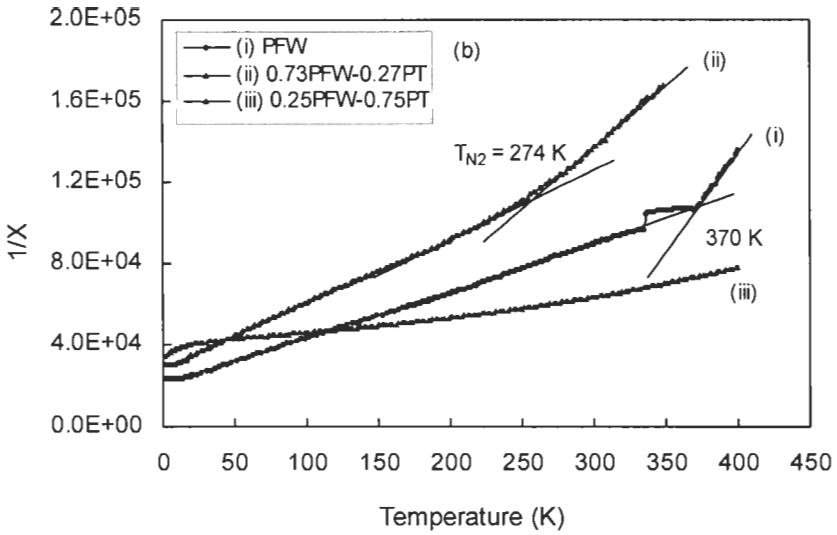

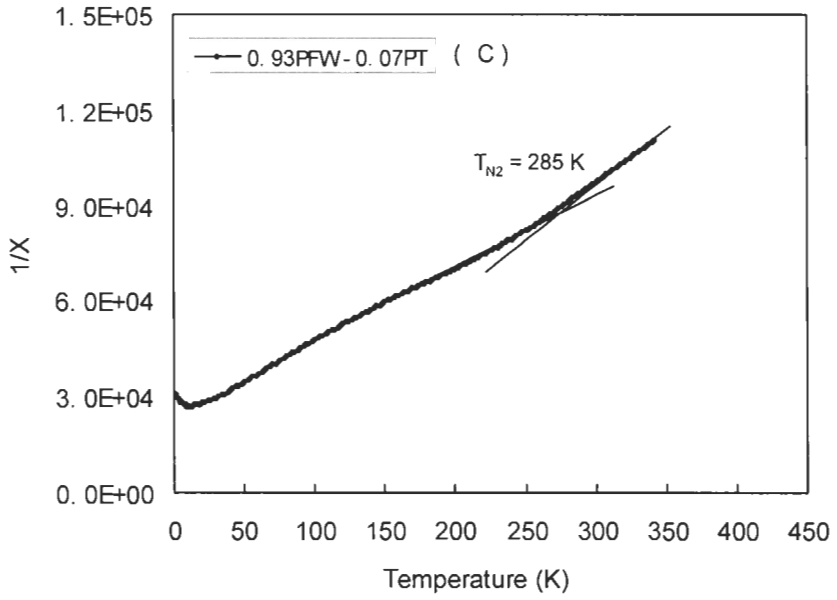

Figure 6.2: Temperature dependence of (a) magnetization and (b, c) reciprocal susceptibility ($1/\chi$) of the (1-x)PFW-xPT crystals, with x = 0, 0.07, 0.27 and 0.75, upon FH (50 Oe, //<100>$_{cub}$) after ZFC.

With the amount of PT component increasing from x = 0 to 0.07, and then to 0.27, the low-temperature magnetic ordering increases from T_{N1} = 8.5 K, to 11 K and to 12.5 K, respectively. On the other hand, the high-temperature magnetic transition shifts toward lower temperatures, i.e. T_{N2} = 370 K, 285 K and 274 K for x = 0, 0.07, 0.27 K, respectively, as shown in Fig. 6.2b and c, indicating a destabilization of the antiferromagnetic ordering. As the PT content is increased to 0.75, no magnetic transitions could be detected and the paramagnetic behaviour appears almost in the whole measured temperature range down to 2 K. The dilution of the concentration of magnetic ion Fe^{3+} by the substitution with the non-magnetic Ti^{4+} ion affects the magnetic nanodomains, and decreases and weakens the magnetic interactions in the system. In fact, it was reported that the magnetic ordering in the ceramics of 0.50PFW-0.50PT might already disappear based on the temperature dependence of magnetization [13].

To further study the magnetic interactions, the magnetization of the (1-x)PFW–xPT crystals, x = 0, 0.07, 0.27 and 0.75, was measured upon FH at 1000 Oe after ZFC. The results are shown in Figure 6.3. Similar to the small field heating at 50 Oe after ZFC (Fig. 6.2), two magnetic transitions are found in PFW occurring at T_{N1} = 9 K, and T_{N2} = 370 K, respectively. The high-temperature magnetic transitions in the 0.93PFW-0.07PT and 0.73PFW-0.27PT systems are also determined from the plot of the reciprocal magnetic susceptibility ($1/\chi$) *vs.* temperature in Fig. 6.3b. No magnetic anomaly in the 0.25PFW-0.75PT system can be detected, even though the external magnetic field was increased by 20 times. Compared with the results in Fig. 6.2a, the induced magnetization in Fig. 6.3a is increased with the increasing field, but the magnetic transition temperatures remain almost unchanged with the magnetic field.

Based on the above results, a partial magnetic phase diagram of the (1-x)PFW-xPT system is established, as shown in Fig. 6.4. It indicates the areas of paramagnetic, antiferromagnetic and (weakly) ferromagnetic phases as a function of temperature (T) and composition (x), which are delimited by the two magnetic transition temperatures. The high-temperature magnetic ordering temperature T_{N2} decreases more rapidly as the PT-content increases from 0 to 0.1, suggesting that the dilution of the magnetic ion has a significant influence on the magnetic transition at T_{N2}. Interestingly, the low-temperature magnetic transition temperature increases slightly with the increase of x from 0 to 0.27.

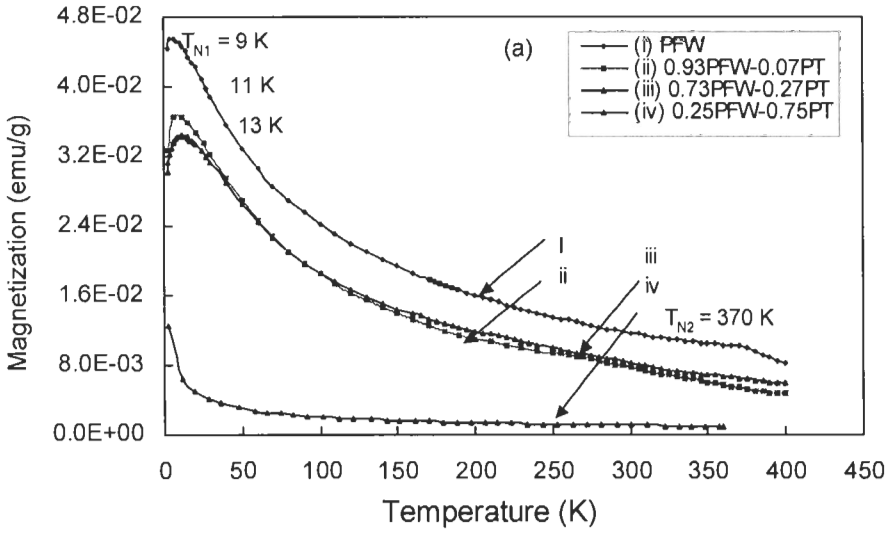

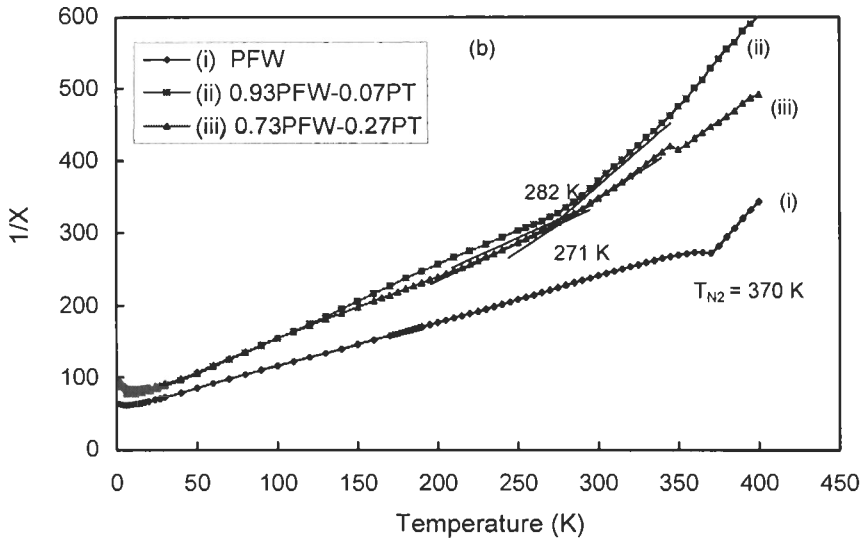

Figure 6.3: Temperature dependence of (a) magnetization and (b) reciprocal susceptibility ($1/\chi$) of the (1-x)PFW-xPT crystals, with x = 0, 0.07, 0.27 and 0.75, upon FH (1000 Oe, //$<100>_{cub}$) after ZFC.

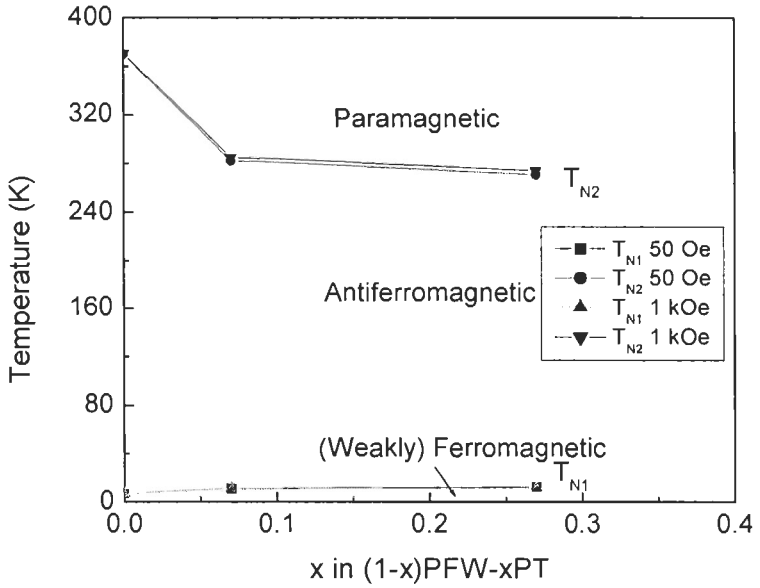

Figure 6.4: Partial magnetic phase diagram of the (1-x)PFW-xPT system, which delimits the paramagnetic, antiferromagnetic, and weakly ferromagnetic phases.

It can be seen in Fig. 6.4 that the high-temperature magnetic transition at T_{N2} shifts towards lower temperatures with the decreasing concentration of the magnetic Fe^{3+} ions in the (1-x)PFW-xPT system, in order to balance the magnetic ordering against thermal agitation. However, the low-temperature magnetic transition at T_{N1} slightly moves to higher temperature, which seems to come into conflict with the common belief that the "dilution" of the concentration of magnetic ion Fe^{3+} usually weakens the magnetic coupling strength and would cause the magnetic transition to shift towards a lower temperature in order to stabilize the magnetic ordering against the thermal motion agitation. Similar experimental results were also found in the PFW-PT ceramic system, but were not explained in detail [16, 17]. In order to understand this unusual variation of T_{N1} with composition, the unit cell volume of the perovskite solid solution calculated from the XRD patterns [19] is presented in Fig. 3.6 (Chapter 3) as a function of composition. The volume decreases with the PT content x increasing from 0 to about 0.30, and then increases slowly with x further increasing. The magnetic interaction distance between the magnetic ions Fe^{3+}, i.e. $- Fe^{3+} - O - W - O - Fe^{3+} -$, in the ordered region, corresponding to the double edge length of the primitive unit cell, is also reduced, giving rise to a stronger magnetic coupling. Therefore, the thermal stability of magnetic ordering increases and the transition temperature T_{N1} moves toward a higher temperature. Two different factors determine the magnetic ordering, (i) the concentration of Fe^{3+} ions and (ii) the magnetic interaction distance. Our results seem to point out that at PT content $x \leq 0.27$, the enhanced magnetic coupling due to the shortened magnetic interaction distance plays a dominant role in the low-temperature magnetic ordering, so that T_{N1} shifts toward higher temperature with increasing x. With the PT content further

increasing, it is expected that the effect of the "dilution" of Fe^{3+} ion concentration on the destabilization of the weakly ferromagnetic ordering becomes more important, and thereby T_{N1} should decrease. At higher PT content (e.g. 75%), no magnetic orderings should occurs because the so much diluted Fe^{3+} ions become magnetically isolated almost in the whole range of experimental temperatures.

The decrease of the average unit cell volume as the PT-content increases up to x = 0.30 should normally enhance the both magnetic interactions at T_{N2} and T_{N1} in the same way. However, since the latter interaction occurs at a much lower temperature of T_{N1}, the thermal agitation/destabilization effect is much smaller and thereby the enhancement of magnetic interaction is much more effective than the interaction that occurs at T_{N2}. In other words, the effect of decreasing unit cell volume on increasing T_{N2} is offset by the thermal destabilization effect, while the dilution of magnetic Fe^{3+} ion by the substitution of PT becomes a predominant factor. Therefore, T_{N2} decreases while T_{N1} increases with the PT-content x increasing from 0 to about 0.30.

The influence of PT-content on the low-temperature magnetic ordering was further investigated by ac magnetization measurements, in which an oscillating ac magnetic field is applied on the sample. This method demonstrates an increased sensitivity to the measurements by reducing the effective noise level. A small ac magnetic field of 5 Oe at frequencies of 10 Hz and 1 kHz, respectively, was applied on the crystals. Figure 6.5 shows the ac magnetization of the PFW and 0.93PFW-0.07PT crystals in the temperature range of 1.9 K ~ 20 K. An ac magnetization peak appears at $T_{N1} \approx 8.0$ K for PFW in Fig. 6.5a, which is close to the magnetic ordering temperature detected in the dc magnetic measurements (Fig. 6.2 and 6.3). In the 0.93PFW-0.07PT

crystal, the magnetic transition appears at 12 K and 13.5 K at the frequencies of 10 Hz and 1 kHz, respectively, as shown in Fig. 6.5b. This indicates the frequency dispersion of the magnetization, probably arising from the relaxational responses of the magnetic nanodomains, which is possibly enhanced by the addition of a third and non-magnetic ion (Ti^{4+}) on the B-site of the perovskite structure. The imaginary part of magnetization (M") referred to the right y-axis has an order of magnitude of 10^{-6}, indicating a very small magnetic energy loss in the system.

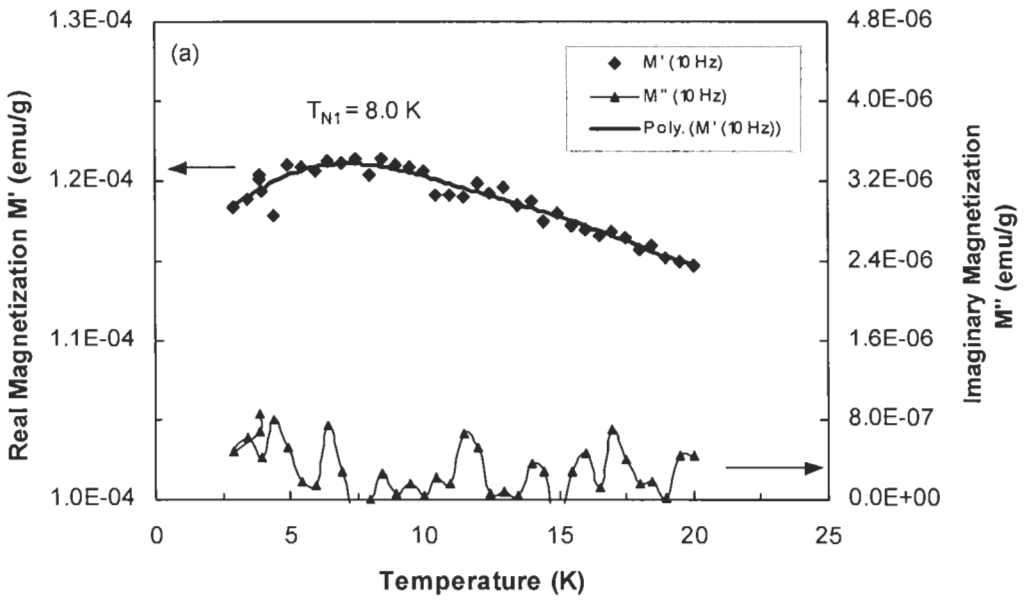

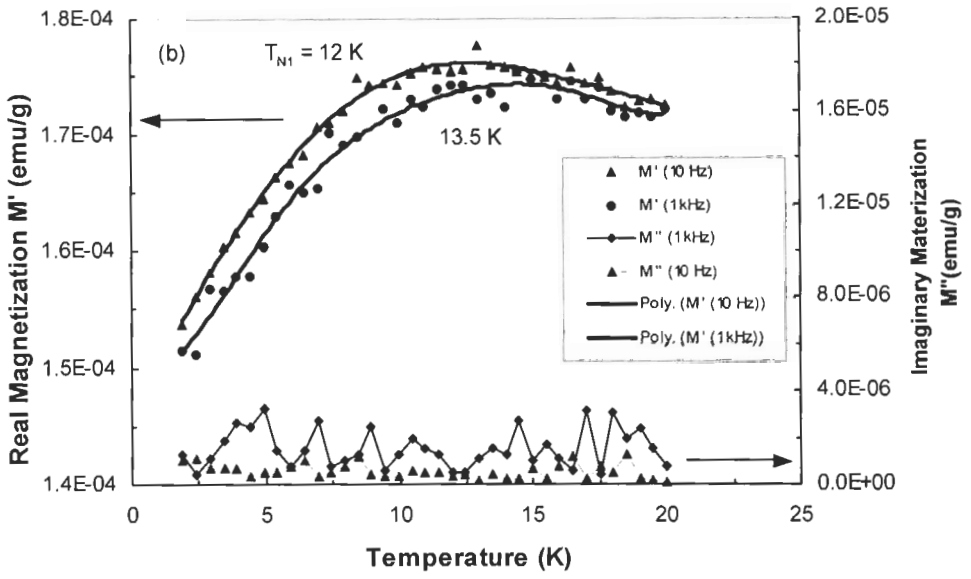

Figure 6.5: AC magnetization of (a) PFW and (b) 0.93PFW-0.07PT crystals as a function of temperature measured at a field of 5 Oe with the frequencies of 10 Hz and 1 kHz, respectively.

6.4.2 Magnetic Hysteresis Loops

The macroscopic magnetization of the (1-x)PFW-xPT crystals was measured by the application of an alternating magnetic field. Figure 6.6 presents the magnetic field dependence of the magnetization of the PFW crystal at 1.9 K, 150 K, 185 K, 300 K and 390 K, respectively. At low temperature (T = 1.9 K), a slim hysteresis loop was displayed, as shown in Fig. 6.6a, confirming the presence of a weak ferromagnetism in the material. It is believed that the weak ferromagnetism in PFW arises from the canted antiferromagnetic interactions in which the magnetic moments of two sublattices containing Fe^{3+} ions no longer completely align antiparallel, but are at some constant angle, to each other. This kind of weak ferromagnetic ordering was observed at low temperatures in other compounds ($MnCO_3$, $CoCO_3$, α-Fe_2O_3 etc.) with primarily

antiferromagnetic ordering [20]. In the ferromagnetic $Pb(Fe_{1/2}Nb_{1/2})O_3$ single crystals [21], the existence of the hysteresis below T_N was suggested to originate from the magnetoelectric coupling.

At 150 K (Fig. 6.6b), 185 K (Fig. 6.6c), and 300 K (Fig. 6.6d), the magnetization vs. field becomes non-linear and the non-linearity increases as temperature decreases, indicating an enhancement of antiferromagnetic ordering. A complete linear field dependence of magnetization occurs at the temperature of 390 K, which obeys the Curie-Weiss law. Hence, PFW is in a paramagnetic state above T_{N2} = 370 K (Fig. 6.6e).

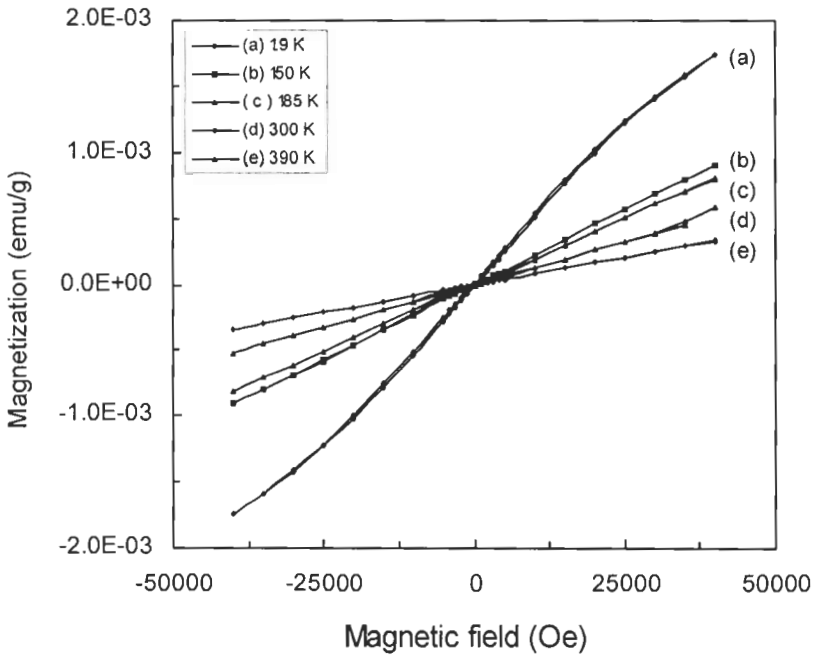

Figure 6.6: Field dependence of the magnetization for the PFW crystal measured at (a) 1.9 K, (b) 150 K, (c) 185 K, (d) 300 K, and (e) 390 K, respectively.

Figure 6.7 gives the induced magnetization of the 0.93PFW-0.07PT crystal. Interestingly, compared with PFW, a more opened magnetic hysteresis loop was displayed at low temperature (T = 1.9 K, Fig. 6.7a), suggesting an enhancement of the weak ferromagnetism by the PT-substitution. The nonlinear magnetization showing antiferromagnetic behaviour appears in the temperature range of T_{N1} - T_{N2} (Fig. 6.7b). At higher temperatures (T ≥ 300 K or T ≥ T_{N2}), a linear field dependence of the magnetization appears, indicating the paramagnetism in the material (Fig. 6.7c, d, and e). For the 0.73PFW-0.27PT crystal, the M-H hysteresis becomes even more opened and hence the weak ferromagnetism more enhanced, as shown in Fig. 6.8

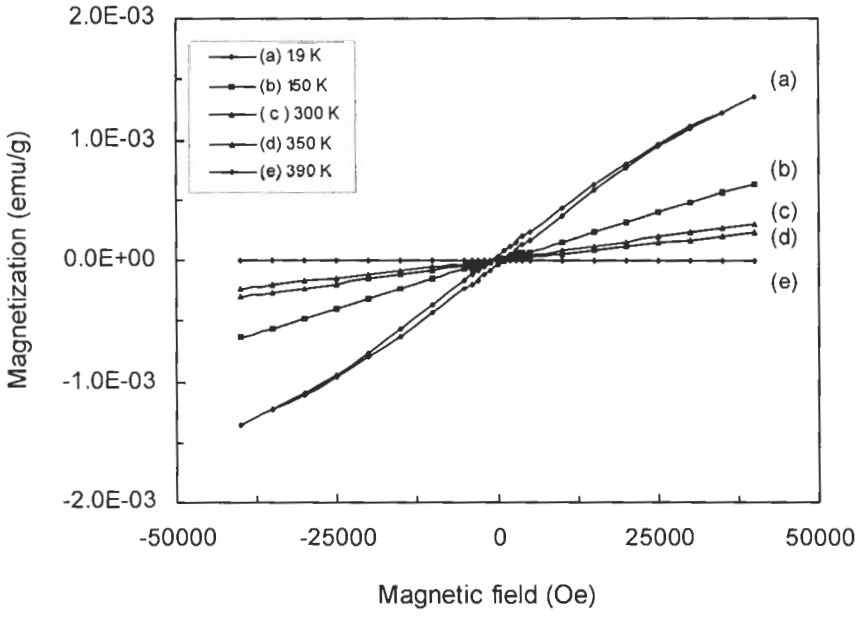

Figure 6.7: Field dependence of the magnetization for the 0.93PFW-0.07PT crystal measured at (a) 1.9K, (b) 150 K, (c) 300 K, (d) 350 K, and (e) 390 K, respectively.

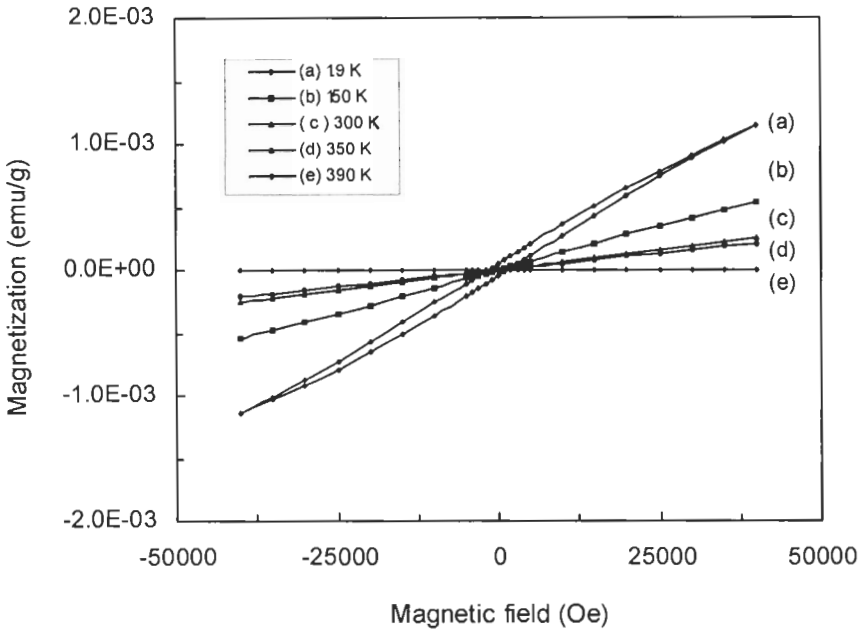

Figure 6.8: Field dependence of the magnetization for the 0.73PFW-0.27PT crystal measured at (a)1.9 K, (b) 150 K, (c) 300 K, (d) 350 K, and (e) 390 K, respectively.

Figure 6.9 presents the M(H) relations of the 0.25PFW-0.75PT crystal at different temperatures. Only a nonlinear M(H) curve appears at T = 2 K (Fig. 6.9a), indicating a tendency towards antiferromagnetic order. This result is basically consistent with the temperature dependence of magnetization shown in Fig. 6.2 and Fig. 6.3, which deviate from the linearity at low temperature. A perfect linear relationship of the magnetization vs. field occurs at 10 K (Fig. 6.9b), 200 K (Fig. 6.9c), and 300 K (Fig. 6.9d). Therefore, the 0.75PFW-0.25PT crystal remains in the paramagnetic state down to very low temperature.

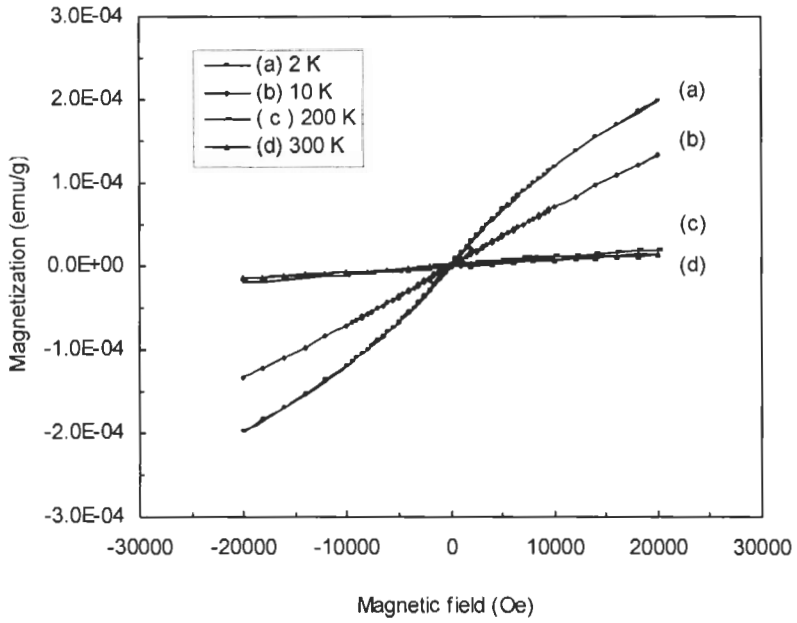

Figure 6.9: Field dependence of the magnetization for the 0.25PFW-0.75PT crystal measured at (a) 2 K, (b) 10 K, (c) 200 K, and 300 K, respectively.

Figure 6.10 shows the field dependences of the magnetization at 1.9 K for the (1-x)PFW-xPT crystals, with x = 0, 0.07, 0.27 and 0.75. With the increasing amount of the non-magnetic PT component, the magnetization gradually decreases due to the dilution of the magnetic Fe^{3+} ions. Therefore, the addition of the PT component in the system changes not only the microstructure with a redistribution of the ordered/disordered regions, but also the magnetic interactions and relaxor ferroelectric behaviour (from relaxor ferroelectric to normal ferroelectric).

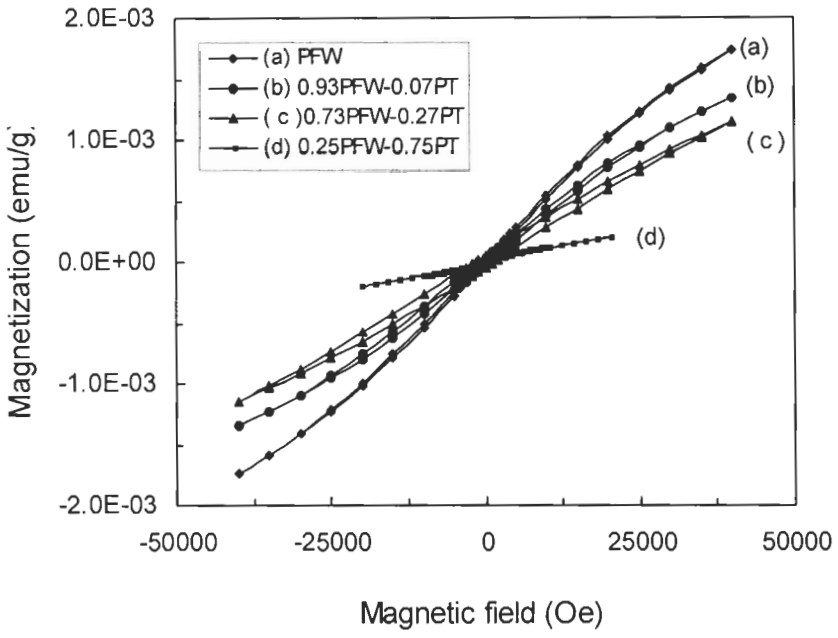

Figure 6.10: Magnetic hysteresis loops for the (1-x)PFW-xPT crystals with various PT contents measured at 1.9 K.

The (1-x)PFW-xPT crystals, with x = 0, 0.07 and 0.27 display a weak ferromagnetism at low temperature. Figure 6.11 is the remnant magnetization M_r as a function of the PT content (x). It can be seen that the remnant magnetization (or hysteretic effect) increase as the PT content increases from 0 to 0.27, and then decrease with the further increasing the amount of PT component. This phenomenon is in accordance with the variation of the low-temperature magnetic transition temperature T_{N1} with the PT content x, demonstrating an enhancement of weak ferromagnetism by the addition of the ferroelectric PT in the solid solution up to x = 0.27.

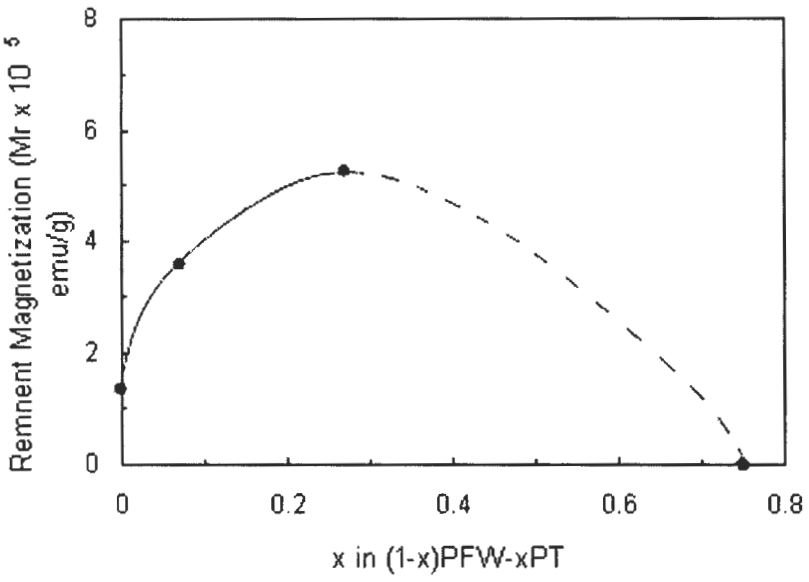

Figure 6.11: Variation of the remnant magnetization at 1.9 K as a function of ferroelectric PT-content for the (1-x)PFW-xPT crystals.

6.5 Conclusions

The magnetic properties in the (1-x)PFW-xPT single crystals, x = 0, 0.07, 0.27 and 0.75, have been investigated by measuring the magnetization as a function of temperature and magnetic field. Two types of antiferromagnetic orderings have been observed on the temperature dependence of magnetization in the crystals with $x \leq 0.27$, which arise from the different magnetic interactions. The low-temperature magnetic ordering corresponding to the weakly ferromagnetic to antiferromagnetic transition occurs at T_{N1} = 8.5 K, 11 K, and 13 K for x = 0, 0.07, and 0.27, respectively, which results from the canting of the primarily antiferromagnetic coupling in the ordered regions, through the $- Fe^{3+} - O - W - O - Fe^{3+} -$ pathway. The high-temperature ordering referred to antiferromagnetic to paramagnetic transition appears at T_{N2} = 370 K, 284 K, and 274 K, respectively, which arises from the antiferromagnetic coupling of the

– Fe^{3+} – O – Fe^{3+} –type occurring in the disordered microregions. With the measuring magnetic field increasing from 50 Oe to 1000 Oe, the magnetization increases, but the magnetic transition temperatures T_{N1} and T_{N2} remain unchanged. The low-temperature magnetic orderings in the PFW and 0.93PFW–0.07PT systems have been further confirmed by means of ac magnetization measurements. It is worth noting that no clear and reliable anomaly on the temperature or magnetic field dependence of magnetization has been found near the temperature of the maximal dielectric permittivity ($T_m \approx 185$ K).

There are two factors that affect the magnetic transitions in the (1-x)PFW–xPT system. On the one hand, the "dilution" of the concentration of the magnetic ion Fe^{3+} by the addition of the non-magnetic PT component generally destabilizes the magnetic ordering of the substance. On the other hand, the decrease in distance of the magnetic interaction due to lattice contraction gives rise to a stronger magnetic coupling between adjacent Fe^{3+} ions in the system. The former is responsible for the vanishing of the low-temperature and high-temperature magnetic orderings at T_{N1} and T_{N2}, respectively, as the amount of PT component is increased to a large extent. The latter plays an important role in the shifting towards higher temperatures of the low-temperature magnetic transition and the enhancement of the weak ferromagnetism with the increasing PT amount in the low-content PT crystals. Based on the analysis of the magnetic transitions, a partial magnetic phase diagram has been established, which delimits the paramagnetic, antiferromagnetic and weakly ferromagnetic phases in the (1-x)PFW-xPT solid solution system.

The magnetization of the crystals (1-x)PFW-xPT *vs* an alternating magnetic field has been measured at different temperatures. In the PFW, 0.93PFW-0.07PT and

0.73PFW–0.27PT crystals, the M(H) curve at 1.9 K displays a slim hysteresis loop with weak ferromagnetic feature. The remnant magnetization and the hysteretic effect increase with the increasing PT content, indicating an enhancement of the ferromagnetism by the addition of the ferroelectric PT (up to x = 0.27). The M(H) variation appears in the form of a nonlinear curve without hysteresis in the temperature range between T_{N1} and T_{N2}, consistent with the antiferromagnetic nature in this temperature interval. At the temperatures above T_{N2}, a perfect linear relationship between the magnetization and magnetic field is displayed and the Curie-Weiss relationship is observed. Hence, the crystals are in the paramagnetic state. For the 0.25PFW–0.75PT crystal, the paramagnetic behaviour exists down to 10 K with only a tendency toward antiferromagnetic ordering at $T < 10$ K, suggesting that the magnetic Fe^{3+} ions become isolated in the perovskite structure as a result of the high substitution of non-magnetic Ti^{4+} ion for Fe^{3+}.

Therefore, as the perovskite structure gradually changes from a pseudo-cubic to a tetragonal phase by increasing the amount of ferroelectric and non-magnetic PT component in the PFW-PT system, the nature of dipole interaction transforms from the relaxor ferroelectric state with short-range order to the ferroelectric long-range order. At the same time, the low-temperature magnetic ordering slightly shifts toward a higher temperature with enhanced weak ferromagnetism up to x = 0.27 and then disappears at higher PT content, while the high-temperature antiferromagnetic transition moves towards lower temperatures and then vanishes. These observations demonstrate the intrinsic relationships among the microstructure, composition, dielectric and magnetic properties and the intriguing multiferroic feature of the relaxor-based PFW–PT solid solution system.

6.6 References

[1] Z.-G. Ye and H. Schmid, *Ferroelectrics* **162**, 119 (1995).

[2] Z.-G. Ye, K. Toda, M. Sato, E. Kita and H. Schmid, *J. Korean Phys. Soc.* **32,** S1028 (1998).

[3] L. Mitoseriu, M. M. Carnasciali, P. Piaggio, P. Nanni, *Appl. Phys. Lett.* **81,** 5506 (2002).

[4] G. A. Smolenskii and V. A. Bokov, *J. Appl. Phys.* **35**, 915 (1964).

[5] N. Hur, S. Park, P.A. Sharma, J.S.Ahn, S. Guha & S-W. Cheong, *Nature,* **429,** 394 (2004).

[6] T. Kimura et al. *Phys. Rev. B* **67**, 180401 (2003).

[7] G. A. Smolenskii and I. E. Chupis, *Ferroelectromagnets. Usp. Fiz. Nauk.* **137**, 415 (1982).

[8] H. Schmid, *Ferroelectrics* **162**, 317 (1994).

[9] J. Wang, J. B. Neaton, H. Zheng, V. Nagarajan, S. B. Ogale, B. Liu, D. Viehland, V. Vaithyanathan, D. G. Schlom, U. V. Waghmare, N. A. Spaldin, K. M. Rabe, M. Wuttig, R. Ramesh, *Science* **299**, 1719 (2003).

[10] V. A. Bokov, I. E. Myl'nikova and G. A. Smolenskii, Ferroelectrics-Antiferromagnets, Zh. Teor. Fiz **42 (2)**, 643 (1962).

[11] V. I. Al'shin, Investigation of Magnetoelectric Interactions in Magnetically Ordered Crystals, Cand. Sci. (Phys. –Math.) Dissertation, Leningrad : Inst. of Semiconductors, USSR Acad. Sci., 1970.

[12] K. Uchino and S. Nomura, *Ferroelectrics* **17**, 505 (1978).

[13] J. B. Goodenough, D. G. Wickham and J. W. Croft, *J. Phys. Chem. Solids* **5**, 107

(1958).

[14] M. A. Gilleo, *J. Phys. Chem. Solids* **13**, 33 (1960).

[15] S. A. Ivanov, S.-G. Eriksson, R. Tellgren, and H. Rundlöf, *Experimental Report* **486**, 1 (2006).

[16] L. Mitoseriu, D. Marré, A. S. Siri and P. Nanni, *Appl. Phys. Lett.* **83**, 5509 (2003)

[17] L. Mitoseriu, D. Marré, A. S. Siri, A. Stancu, C. E. Fedor and P. Nanni, *J. Opt. and Adv. Mater.* **6** (2), 723 (2004).

[18] Z.-G. Ye and H. Schmid, *J. Crystal Growth* **167**, 628 (1996).

[19] L. Feng and Z.-G. Ye, *J. Solid State Chem.* **163**, 484 (2002).

[20] I. E. Dzialoshinskii, *Soviet Physics Jetp* **5** (6), 1259 (1957).

[21] Y. Yang, J.-M. Liu, H. B. Huang, W. Q. Zou, P. Bao, and Z. G. Liu, *Phys. Rev. B* **70**, 132101 (2004).

Chapter 7:
Mössbauer Spectroscopic Studies of $Pb(Fe_{2/3}W_{1/3})O_3$ and $Pb(Fe_{2/3}W_{1/3})O_3$ -$PbTiO_3$

7.1 Introduction

The magnetic properties of PFW and (1-x)$Pb(Fe_{2/3}W_{1/3})O_3$ – x$PbTiO_3$ [(1-x)PFW-xPT] single crystals presented in the last chapter indicate that the magnetic transition temperatures change with the PT content and that the different magnetic orderings occur in the temperature range of 2 ~ 390 K (see Chapter 6).

On the atomic scale, the statistically random distribution of Fe^{3+} and W^{6+} on the crystallographic B-site positions of the perovskite structure very likely affects the electric field symmetry at the position of Fe nucleus, which should result in a hyperfine interaction between the electric quadrupole moment of the Fe nucleus and the electric field gradient at the nucleus. In addition, the magnetic field arising from the magnetic ordering of Fe^{3+} ions may interact with the Fe nuclear magnetic moment, giving rise to a magnetic hyperfine interaction at the Fe nucleus, which is known as magnetic hyperfine Zeeman splitting. The magnetic hyperfine interaction can bring about as many as six gamma absorption peaks in the Mössbauer spectrum (sextet). Therefore, the Mössbauer spectroscopic technique is a very useful tool to investigate these magnetic (or electric) hyperfine interactions between the Fe nucleus and its magnetic (or electronic)

environments. The environment is closely related to the valence of the Mössbauer atom, the structure of the compound, and its magnetic and electric properties.

Despite the unusual relaxor ferroelectric and magnetic properties of the PFW and PFW-PT systems, and thereby their potential multiferroic features, there have been few studies on the Mössbauer spectroscopy of PFW and PFW-based multicomponent material systems, none of which was performed below liquid nitrogen temperature. Nomura *et al.* [1] measured the Mössbauer spectra of the PFW ceramics at temperatures of 100 K and 400 K, and attributed the magnetic hyperfine Zeeman splitting in the Mössbauer spectra of PFW at 100 K to the statistically random distribution of the Fe^{3+} ions on the B-site positions of the perovskite structure. The data suggested the existence of two sites of Fe^{3+} ions with internal magnetic field strengths slightly different from each other. Uchino and Nomura [2] investigated the Mössbauer spectra of the $0.6Pb(Fe_{2/3}W_{1/3})O_3$–$0.4Pb(Co_{1/2}W_{1/2})O_3$ [0.6PFW-0.4PCW] solid solution at 295 K and 89 K, i.e. above and below the "Curie" temperature of the system, and observed an asymmetric shape of the paramagnetic Mössbauer spectrum with a doublet and singlet above the Curie temperature. This was explained by the proposed model of two sublattices in which Fe^{3+} ions fill in the different sites, giving rise to the different electric field gradients. Below the "Curie" temperature, a ferrimagnetic Mössbauer spectrum composed of a main central peak and a small sextet on the sides was observed. Because of non-resonant scattering by the Pb and W nuclei, the Mössbauer spectra obtained in these two studies were of relatively poor quality. It was felt that a systematic study of the Mössbauer spectra in the PFW-PT system would be useful for providing a better understanding of the complex magnetic interactions in this disordered structure.

In the present work, the ^{57}Fe isotope-enriched PFW and 0.75PFW-0.25PT ceramics prepared using a B-site precursor method were characterized by X-ray powder diffraction and Mössbauer spectroscopic measurements. The Mössbauer spectra are interpreted based on the magnetic interactions, disorder perovskite structure and the composition.

7.2 Experimental Section

Ceramics of PFW and 0.75PFW-0.25PT solid solutions were prepared by a modified B-site precursor method consisting of two-step reactions. A detailed description of the method can be found in Chapter 3. The mixture of 33 % ^{57}Fe-enriched $^{57}Fe_2O_3$ (75% in abundance) and 67% normal Fe_2O_3 (>99.9%, Alfa) was used as iron oxide starting material.

^{57}Fe Mössbauer spectra of the PFW and 0.75PFW-0.25PT samples were recorded using a Web Research spectrometer operating in transmission mode at temperatures between 295 K and 4.4 K. In addition, Mössbauer spectroscopic measurements for PFW above room temperatures, i.e. 353 K and 373 K, were carried out using a constant acceleration Harwell Mössbauer drive. A $^{57}Co/Rh$ (20 mCi) source was mounted on a velocity transducer driven in a constant acceleration mode at room temperature. A Reuter-Stokes proportional counter was used to monitor the 14.4 keV Mössbauer γ-ray. The spectra were calibrated using a 25 μm Fe foil spectrum obtained at room temperature and isomer shifts are reported relative to Fe foil.

Powdered samples of around 100 mg were prepared on a Parafilm sheet and sealed using Kapton tape. By using samples enriched in ^{57}Fe, excellent quality Mössbauer spectra were obtained.

Samples were cooled for the low-temperature studies in a Janis Research SHI-850 variable temperature closed-cycle refrigerator. For PFW, which was studied above room temperature, the sample was mounted in a hole through an electrically heated copper block, insulated with asbestos tap. The temperature at the sample was measured using a thermocouple to ± 2K. The WMoss (v. 2.5) Mössbauer spectral analysis software supplied with the spectrometer was used to fit the Mössbauer data.

7.3 X-ray Diffraction

Figure 7.1 displays the X-ray powder diffraction patterns of the ^{57}Fe-enriched PFW and 0.75PFW-0.25PT ceramic samples. Both of them have a pseudo-cubic perovskite structure, which is consistent with the phase diagram previously established in Chapter 3 for the (1-x)PFW-xPT binary ceramic system where the phase transition from a pseudo-cubic phase to the tetragonal phase usually happens as the PT content is increased higher than 25% in the binary system.

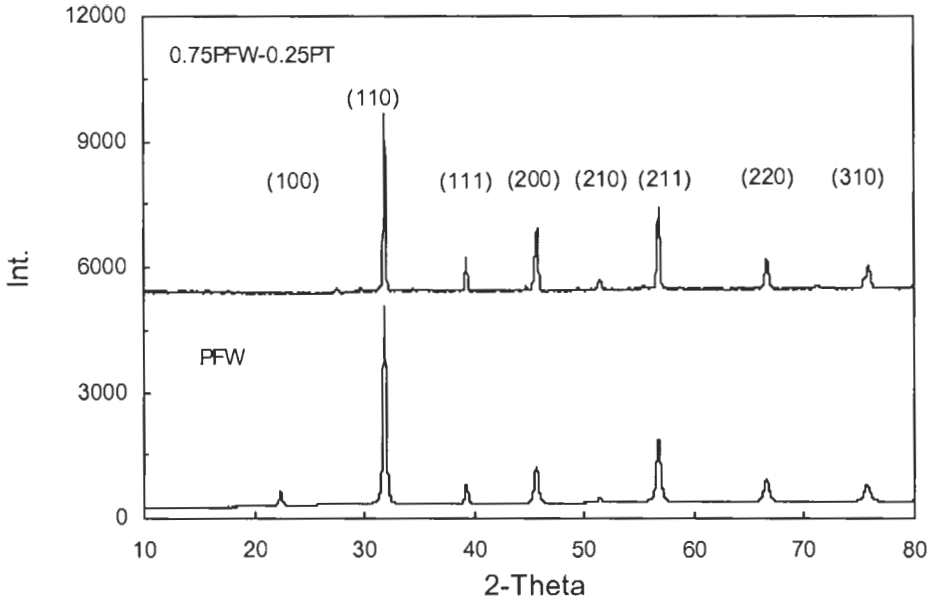

Figure 7.1: X-ray diffraction patterns of the ^{57}Fe-enriched PFW and 0.75PFW-0.25PT ceramics at room temperature.

7.4 Mössbauer Spectroscopy of PFW and 0.75PFW–0.25PT

7.4.1 Mössbauer Spectroscopy of PFW

Figure 7.2 shows the Mössbauer spectra of PFW at 373 K and 353 K, respectively. The quadrupole split doublet observed in these spectra has an isomer shift of 0.34 mm/s and a splitting of 0.50 mm/s, with a linewidth of 0.55 mm/s. These parameters are consistent with the high spin state of Fe^{3+}. The 373 K spectrum can be fitted to a single doublet. In contrast to the interpretations of References 6 and 7, there is no clear evidence for two iron sites with different quadrupole splittings. The different iron sites which arise from the random distribution of Fe^{3+} and W^{6+} ions on the B-sites of the perovskite structure, as shown in Fig. 7.3, appear to be indistinguishable in the Mössbauer spectrum. PFW becomes anti-ferromagnetic below T_{N2} (= 340 ~ 370 K) [3, 4,

Chapter 6]. As a result, in the 353 K spectrum (Fig. 7.2b), we begin to see the onset of magnetic ordering which produces the broad background absorption on which the doublet is still superimposed.

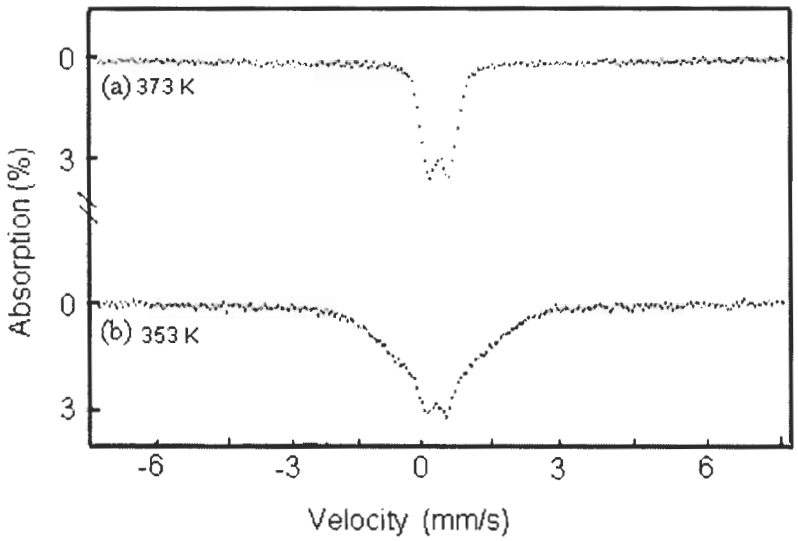

Figure 7.2: Mössbauer spectra of PFW at (a) 373 K and (b) 353 K.

The Mössbauer spectra of PFW at 295 K, 77 K and 4.4 K are shown in Fig. 7.4. These spectra clearly show magnetic ordering and the doublet is no longer observed. The magnetic field observed at the iron atoms increases as the temperature is lowered. This, and the general form of the spectra at 353 K and 373 K, is consistent with the presence of thermal relaxation which is greater at higher temperatures and which decreases as the temperature is lowered. This would be consistent with the presence of chemical nano regions within the material. For example, two types of nano regions can be found in Fig. 7.3. One shows a structure of the $-Fe^{3+}-O-Fe^{3+}-$ and the other has a structure of the $-Fe^{3+}-O-W-O-Fe^{3+}-$. Within a nano region, the electron spins on the iron ions begin to line up as the temperature is lowered below T_{N2}, generating the magnetic field. However,

this ordering of a relatively small number of spins has to compete with thermal relaxation which tends to remove the alignment of the spins. As the thermal relaxation decreases at lower temperatures, the magnetic ordering becomes dominant. These processes would result in a distribution of magnetic fields at any one temperature, broad linewidths and a divergence from the relative intensities normally observed in a magnetic hyperfine interaction, at least at higher temperatures.

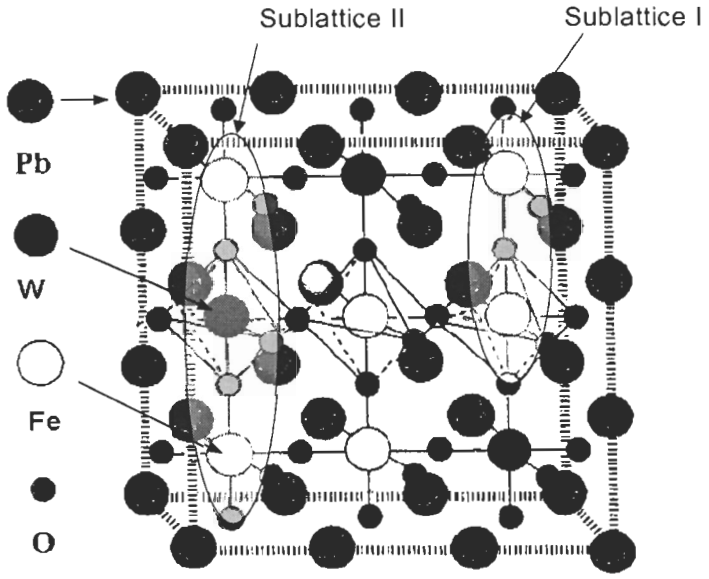

Figure 7.3: PFW perovskite structure showing the octahedral B-site positions occupied by Fe^{3+} and W^{6+} ions at random, which forms two different sublattices of Fe^{3+} ion.

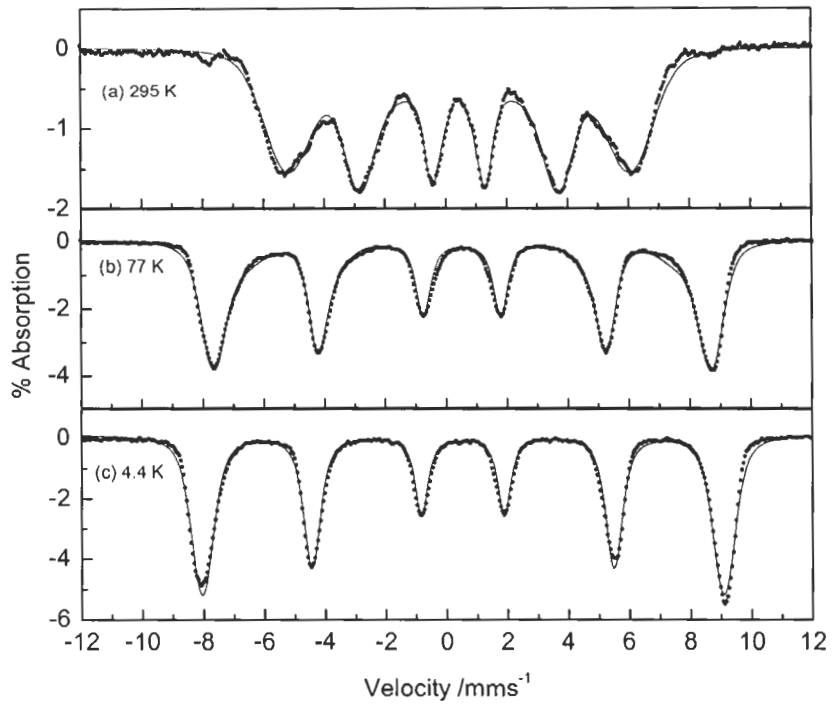

Figure 7.4: Mössbauer spectra of the PFW samples at (a) 295 K, (b)77 K and (c) 4.4 K, respectively. The solid lines represent the fitting results.

According to the magnetization as a function of temperature reported in Chapter 6, at $T_{N1}\approx 9.0$ K the PFW material becomes weakly ferromagnetic due to a canted antiferromagnetic interaction where the magnetic moments on the two sub-lattices containing Fe^{3+} are no longer anti-parallel but are at some angle to each other. The spectrum at 4.4 K shows a normal magnetic sextet with H=530 kOe, suggesting the two sub-lattices below 9.0 k have the same internal magnetic field.

As discussed above, the broadened linewidths of the 295 K and 77 K spectra can be explained by the relaxation phenomenon that would result in a range of magnetic field at a given temperature. However, these two spectra can also be fitted assuming the two sub-lattices give rise to different magnetic fields at the two iron sites, at least above T_{N1}. Figure 7.5 shows the hyperfine field distributions obtained using the WMoss (v.2.5) Mössbauer spectral analysis software assuming the two sites model. This interpretation must be treated with some caution. It can be seen that the larger hyperfine field distribution is attributed to the iron ions on site 1 in the disordered nanoregions of the perovskite structure (see Fig. 7.3) because of a stronger magnetic interaction, and the smaller one results from the iron ions on site 2 in the ordered nanoregion with a weaker magnetic interaction. The total field distribution is contributed from the iron ions on the two sites. Table 7.1 lists the Mössbauer parameters obtained based on the fitting of the spectra. At lower temperatures, the isomer shifts keep in a range of 0.3~0.6 mms^{-1}, indicating that the Fe^{3+} ion ($3d^5$) exists in the form of the high spin state [1, 5, 6], which is expected.

Table 7.1: Mössbauer parameters: isomer shifts [δ (mm^{-1})] and magnetic hyperfine fields [H_{hf} (kOe)] for PFW.

Temperature (K)	Subspectrum	δ (mms^{-1})	H_{hf} (kOe)
295 K	B-site 1	0.43	348
	B-site 2	0.45	229
77 K	B-site 1	0.52	505
	B-site 2	0.53	451
4.4 K	B-site	0.53	530

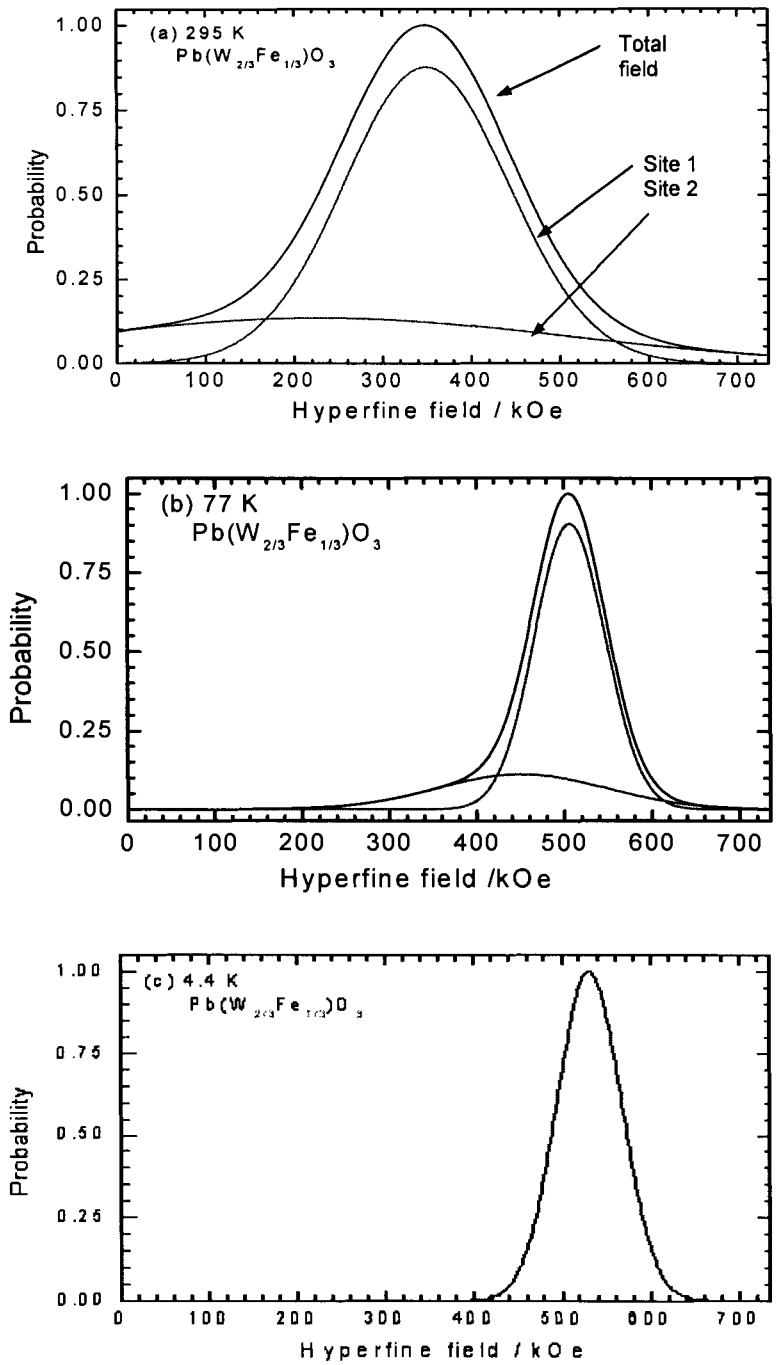

Figure 7.5: Hyperfine field distribution of PFW at (a) 295 K, (b) 77 K and (c) 4.4 K, respectively. The site 1 and site 2 correspond to the fitted results.

7.4.2 Mössbauer Spectroscopy of 0.75PFW-0.25PT

The Mössbauer spectra of 0.75PFW-0.25PT at 295 K, 77 K and 4.4 K are shown in Fig. 7.6. The dominant feature of the former two spectra is a quadrupole doublet with a splitting of 0.6 mm/s and an isomer shift of 0.4 to 0.5 mm/s (see Table 7.2), again consistent with high-spin state of Fe^{3+}. The somewhat larger splitting observed here in comparison with PFW can be rationalized in terms of the increasing disorder resulting from the addition of PT to the system.

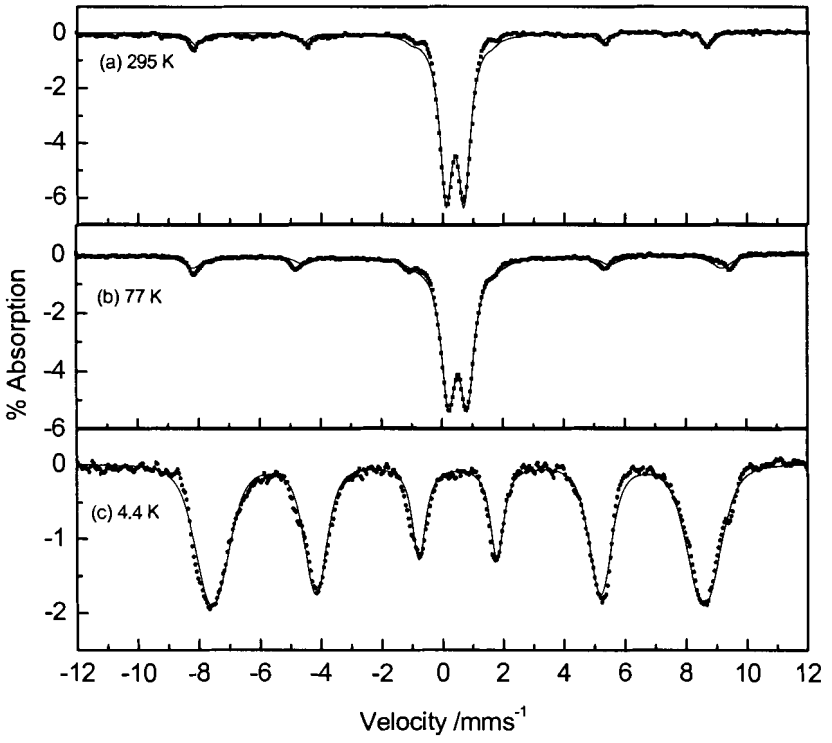

Figure 7.6: Mössbauer spectra of the 0.75PFW-0.25PT sample at (a) 295 K, (b) 77 K and (c) 4.4 K, respectively. Solid lines represent the fitting results.

On cooling to 4.4 K the quadrupole split doublet is replaced by a magnetic hyperfine interaction with a field of 500 kOe. The fact that the onset of magnetic ordering occurs at a much lower temperature in 0.75PFW-0.25PT than in PFW is in agreement with the dilution of the Fe^{3+} ions by the non-magnetic PT component. Magnetic measurements reported in Chapter 6 on this phase show that it is anti-ferromagnetic below 274 K and weakly ferromagnetic below 13 K.

The spectra at 295 K and 77 K contained, in addition to the doublet, a lower-intensity magnetic component. The magnetic field strength of this component increased somewhat in going from 295 K to 77 K. This component is also present in the spectrum at 4.4 K and has a field strength at 4.4 K similar to, but somewhat larger than, that of the primary magnetic component. The fact that the two magnetic field strengths are so similar would be consistent with both arising from iron ions in similar lattice environments. The major magnetic component observed at 4.4 K arises from iron ion on B-site of the perovskite structure. But, the weak magnetic component at 295 K, 77 K and 4.4 K probably result from an impurity, most likely Fe_2O_3. As temperature is lowered, the weak magnetic field was increased and the positions of two lines (#2 and #6) in the spectra were moved clearly, which is very similar to Fe_2O_3. However, no peak of Fe_2O_3 was observed in the X-ray powder diffraction patterns. Further clarification is necessary for the magnetic component at 295 K.

Again, an interpretation in terms of a two-site model is possible. The Mössbauer parameters obtained from the fitting based on a two-sites model are listed in Table 7.2. As mentioned above, all results on the isomer shifts and quadrupole splitting indicate that

the addition of PT component into the system does not change the high-spin state of Fe^{3+} in the measured temperature range.

Table 7.2: Isomer shifts δ (mm^{-1}), quadrupole splitting (mm^{-1}), and magnetic hyperfine fields [H_{hf} (kOe)] for 0.75PFW-0.25 PT.

Temperature (K)	Subspectrum	δ (mms^{-1})	Quadrupole splitting (mms^{-1})	H_{hf} (kOe)
295 K	B-site 1	0.34		525
	B-site 2	0.41	0.59	
77 K	B-site 1	0.5		542
	B-site 2	0.51	0.62	
4.4 K	B-site	0.51		500

The hyperfine field distribution at 4.4 K is presented in Fig.7.7 for 0.75PFW-0.25PT. Compared with the field distribution of PFW at 4.4 K in Fig. 7.5, the hyperfine field of 0.75PFW-0.25PT is smaller, but the corresponding half width of the peak is wider. This suggests that the dilution of the Fe^{3+} ion by the non-magnetic PT component results in an increase of disordered nano regions within the material, giving rise to a broadened field distribution.

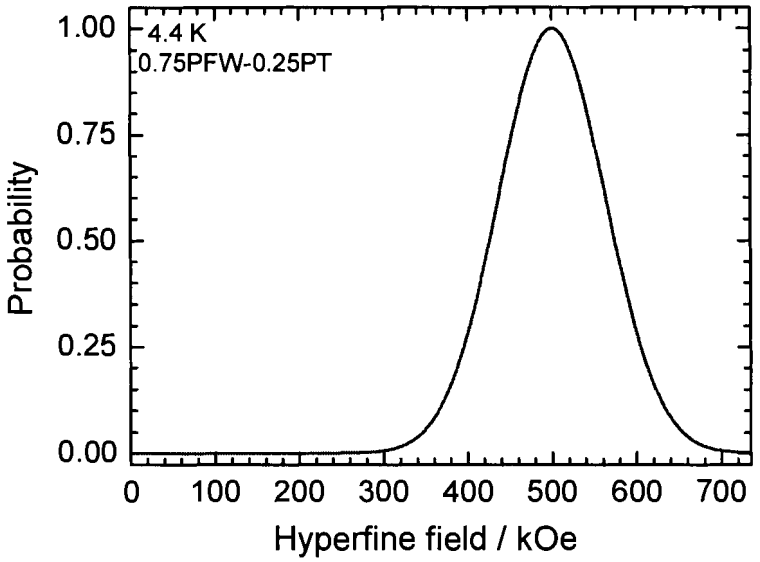

Figure 7.7: Hyperfine field distribution of 0.75PFW-0.25PT at 4.4 K.

7.5 Conclusions

The ^{57}Fe-enriched PFW and 0.75PFW-0.25PT ceramics have been prepared by a B-site precursor method and characterized by X-ray powder diffraction and Mössbauer spectroscopy down to 4.4 K for the first time. Both of the ceramic samples display a pseudo-cubic perovskite structure.

Compared to previous reports on PFW, more clear Mössbauer spectra in the two ^{57}Fe-enriched compounds have been obtained in our experiments, which is beneficial to the subsequent accurate analysis and interpretation of the Mössbauer spectra.

At the temperatures above the (high-temperature) antiferromagnetic transition (T_{N2}=340~370 K), the Mössbauer spectra of PFW show a doublet corresponding to the quadrupole splitting due to the presence of the statistically random distribution of Fe^{3+} ion on the B-sites of the perovskite structure. The onset of magnetic ordering was

observed at 353 K. As the temperature is cooled down to 295 K, 77 K and 4.4 K, the doublet was gradually changed to a sextet, indicating that the magnetic hyperfine interaction dominates the whole Mössbauer spectra below the antiferromagnetic transition T_{N2}. Because the low-temperature magnetic ordering (a canted antiferromagnetic interaction) occurs at $T_{N1} = 9$ K, the spectrum at 4.4 K shows a normal magnetic sextet with H = 530 kOe, suggesting the two sub-lattices below 9 K have the same internal magnetic field. In addition, the spectra show evidence for the presence of thermal relaxation between 4.4 K and 353 K.

On the other hand, the 0.75PFW-0.25PT solid-solution system displays different Mössbauer spectra from PFW at 295 K and 77 K. The spectra consist of a doublet and a lower-intensity magnetic component. In fact, the difference can easily be explained on the basis of the lower onset of magnetic ordering in 0.75PFW-0.25PT than in PFW because of the dilution of the Fe^{3+} ions by the non-magnetic PT component. Two magnetic field strengths in 0.75PFW-0.25PT have been observed at 4.4 K. It is induced that the major magnetic component could arise from iron ion on the B-site of the perovskite structure and the weak one (also appears at 295 K and 77 K) is related to an impurity phase.

Based on the two sites model that gives rise to different magnetic fields on the two iron sites, the Mössbauer spectra of the PFW and 0.75PFW-0.25PT systems have been fitted. As the temperature decreases, the magnetic hyperfine field strength in the PFW system increases, indicating the increase of magnetic stability against thermal relaxation. It is also found that the half width of the hyperfine field distribution of 0.75PFW-0.25PT is broader than that of PFW at 4.4 K, which suggests an increase in the

degree of disordered magnetic domain in nano regions resulting from the addition of the non-magnetic component PT.

The chemical isomer shifts are within 0.3 ~ 0.6 mms^{-1} and quadrupole splitting are in a range of 0.5 to 0.6 mms^{-1} for both PFW and 0.75PFW-0.25PT systems, confirming that the magnetic Fe^{3+} ion exists in the form of high spin Fe^{3+} ($3d^5$) state in the measurement temperature range. The Mössbauer spectroscopic results are consistent with the structural and magnetic behaviours of the PFW and PFW-PT systems reported in the previous chapters.

7.6 References

[1] S. Nmura, M. Kaachi and F. Kojima, *J. Phys. Soc. of Jpn* **35**, 1008 (1973).

[2] K. Uchino and S. Nomura, *Ferroelectrics* **17**, 505 (1978).

[3] Z.-G. Ye, K. Toda, M. Sato, E. Kita and H. Schmid, *J. Korean Phys. Soc.* **32**, S1028 (1998).

[4] A. R. West, *Basic Solid State Chemistry*, John Wiley & Sons, Ltd., Chichester (1996).

[5] A. Vértes, L. Korecz znd K. Burger, *Mössbauer Spectroscopy*, Elsevier Scientific Publishing Company, New York, 1979.

[6] S. Trudel and R. H. Hill, *Polyhedron*, in press, (2006).

Chapter 8:
General Summary

8.1 Extended Summary of This Work

This work has contributed to a better understanding of the relationships of properties, structure and composition in the unusual relaxor-based multiferroic (1-x)PFW-xPT solid solution. It is composed of the following five parts:

i) Synthesis, structure and properties of the relaxor ferroelectric (1-x)$Pb(Fe_{2/3}W_{1/3})O_3$-x$PbTiO_3$ [(1-x)PFW-xPT] solid solution ceramics;

ii) Electrical microstructure and properties of the (1-x)$Pb(Fe_{2/3}W_{1/3})O_3$-x$PbTiO_3$ ceramics;

iii) Growth and electric characterization of the (1-x)$Pb(Fe_{2/3}W_{1/3})O_3$-x$PbTiO_3$ single crystals;

iv) Magnetic properties of the (1-x)$Pb(Fe_{2/3}W_{1/3})O_3$-x$PbTiO_3$ single crystals;

v) Mössbauer spectroscopic studies of $Pb(Fe_{2/3}W_{1/3})O_3$ [PFW] and $Pb(Fe_{2/3}W_{1/3})O_3$-$PbTiO_3$ [PFW-PT].

An extended summary of each part is provided in this chapter to highlight the contribution of the work.

8.1.1 Synthesis, Structure and Properties of the Relaxor Ferroelectric (1-x)$Pb(Fe_{2/3}W_{1/3})O_3$-x$PbTiO_3$ [(1-x)PFW-xPT] Solid Solution Ceramics

A modified B-site precursor method has been developed to prepare highly pure solid solution of (1-x)PFW-xPT in the form of ceramics. It has been shown that this synthesis route is superior to conventional oxide mixed method in the synthesis of the (1-x)PFW-xPT ceramics with high quality perovskite structure and excellent dielectric properties.

The detailed phase analysis and structural refinements based on X-ray diffraction spectra at room temperature indicate that the perovskite structure of (1-x)PFW-xPT is transformed from a pseudo-cubic phase ($x < 0.25$) to a tetragonal phase as the PT content is increased to $x \geq 0.25$. A complete tetragonal perovskite structure is observed at the PT content $x \geq 0.35$. It is possible that a morphotropic phase boundary is located in the composition range $0.25 \leq x \leq 0.35$, which probably displays different dielectric and magnetic properties.

The temperature dependence of the dielectric permittivity measured at various frequencies has shown that the temperature of permittivity maximum T_m in PFW, a characteristic of relaxor ferroelectric behaviour, increases with the increase of the PT content, while the relaxor ferroelectric behaviour of the system is gradually transformed into a normal ferroelectric state, as evidenced by the sharp and nondispersive dielectric permittivity peaks at the ferro/paraelectric phase transition temperature T_C for $x \geq 0.25$. The second anomaly below T_m (or T_C) on the temperature dependence of dielectric constant has been clearly observed for the first time within the composition interval $0.25 \leq x \leq 0.35$. This anomaly is further confirmed by DSC (Differential Scanning Calorimetry) thermal analysis, as an addition thermal event at T_{MPB} corresponding to a

morphotropic phase transition from the low-temperature rhombohedral (or pseudocubic) phase to a tetragonal phase, in addition to the high-temperature ferro-/paraelectric phase transition from the tetragonal to cubic phase at T_C. Therefore, the dielectric and thermal analysis experimental results are in agreement with our prediction based on the perovskite structural analysis.

A complete phase diagram for the (1-x)PFW-xPT system has been established for the first time. It clearly delimits the high-temperature paraelectric cubic phase and the low-temperature ferroelectric rhombohedral (pseudocubic) and tetragonal (*P4mm*) phases. The morphotropic phase boundary (region) is located in the composition range $0.25 \leq x \leq 0.35$, which separates the rhombohedral (pseudocubic) phase from the tetragonal phase. Such a phase diagram is useful for understanding the structural and physical properties of the multiferroic (1-x)PFW–xPT system.

8.1.2 Electrical Microstructure and Properties of the (1-x)Pb($Fe_{2/3}W_{1/3}$)O_3 – x$PbTiO_3$ Ceramics

The ferrolectric behaviour of polycrystalline ceramics is closely associated with the electrical properties (dielectric constant, capacitance, conductivity, resistivity, etc.) of microstructural components. Each microstructural component (phase) has individual contribution to the total electrical properties of the ceramic system.

The combined complex ac impedance and electric modulus formalisms have been applied for the first time to analyze the electrical properties of the (1-x)PFW-xPT ceramics, with x = 0, 0.10, 0.20, 0.25, and 0.325, on the basis of ac impedance spectroscopic measurements at various temperatures. Four different constituent phases (bulk, grain boundary, ceramics-electrode surface diffusion, and minor phase) have been

found to make contributions to the total electrical behaviour of the systems. An equivalent circuit composed of four RC elements connected in series was proposed to simulate and interpret the complex impedance and corresponding modulus spectra. Bulk (grains) and grain boundary phases are the main components making the electrical contributions to the electroceramic materials of PFW-PT. The minor phase shows a very small resistivity and a large electric modulus (M"), suggesting an insignificant electrical contribution to the whole system.

It is also found that the bulk phase and grain boundary phase capacitances (inversely proportional to the electric modulus) increase and reach their maximum values upon cooling down to around the ferroelectric Curie temperature in the 0.75PFW-0.25PT and 0.675PFW-0.325PT systems, showing the highest polar activities near the ferroelectric phase transition. Especially, the capacitance arising from the bulk phase increases more quickly than that from the grain boundary phase. Hence, it is concluded that the dielectric/ferroelectric properties of the ceramics are controlled by the bulk (grains) phase.

The frequency dependence of resistivity and dielectric permittivity of the 0.90PFW-0.10PT ceramics has been studied. It is found that the resistivity decreases in a wavy form with the increasing frequency, demonstrating the capacitance impedance effects on the resistivity of the electroceramic material at room temperature. The dielectric constant decreases significantly with increasing frequency at the temperatures above T_m, but varies very slowly in a non-wavy form with frequency far below T_m. The former is related to the high-temperature frequency dispersion due to the electronic

conductance. The latter clearly shows the dynamic slowing down and freezing of the polar clusters, giving rise to the attenuated relaxation behaviour.

8.1.3 Growth and Electric Characterization of Relaxor Ferroelectric $Pb(Fe_{2/3}W_{1/3})O_3$ –$PbTiO_3$ Single Crystals

Single crystals of the ferroic materials provide ideal specimens for characterizing the dielectric/ferroelectric and magnetic properties, and are also expected to have superior properties over the ceramic samples. Therefore, we have strived to synthesize the crystals and to investigate their structural and physical properties.

Single crystals of the (1-x)PFW-xPT solid solution, with x = 0, 0.07, 0.13, 0.17, 0.27, and 0.75, have been successfully grown for the first time from the high temperature solution using PbO as flux and characterized by X-ray diffraction, dielectric and ferroelectric measurements. As the PT content is increased to $x \geq 0.27$, the crystal structure at room temperature starts to change from a pseudocubic to a tetragonal phase, which is in accordance with the phase diagram established for the (1-x)PFW-xPT ceramics system in Chapter 3.

The temperature and frequency dependences of the dielectric permittivity of the (1-x)PFW-xPT crystals show a crossover from the relaxor ferroelectric behaviour in low PT- content crystals to normal ferroelectricity in high PT-content crystals. The frequency-dispersive dielectric maxima arising from the relaxor properties can be well fitted to the Vogel-Fulcher (V-F) equation. The appearance of normal ferroelectric behaviour indicates an enhanced correlation between dipole moments with the increase of PT-content in the PFW-PT system. It is found that the grown crystals exhibit improved

dielectric properties with much smaller loss factor (tangent δ) than the ceramics at room temperature.

The macroscopic polarization of the (1-x)PFW-xPT crystals, x = 0, 0.13, and 0.27, as a function of the applied alternating electric field has been investigated. The non-linear polarization and a slim electric hysteresis loop obtained in PFW above the maximal permittivity temperature T_m further demonstrate the relaxor ferroelectric characteristic. With the increasing PT content in the binary system, the enhanced ferroelectricity with more opened hysteresis loops was observed around the transition temperature T_m (or T_C). At room temperature, the induced polarization as a function of electric field changes from non-linear, to a slim, and then to a general electric hysteresis loop for PFW, 0.87PFW-0.13PT, and 0.73PFW-0.27PT, respectively, indicates that the addition of PT component enhances the ferroelectric order range through the ferroelectrically active Ti^{4+}ions on the B-site of the perovskite structure.

8.1.4 Magnetic Properties of the (1-x) $Pb(Fe_{2/3}W_{1/3})O_3$ –x$PbTiO_3$ Single Crystals

Apart from the relaxor ferroelectric behaviour, PFW also exhibits peculiar magnetic properties because of the presence of the paramagnetic Fe^{3+} ions. The magnetization of the single crystals of the (1-x)PFW-xPT solid solution, with x = 0, 0.07, 0.27 , and 0.75, have been measured as a function of temperature and magnetic field. Two types of antiferromagnetic orderings and a succession of magnetic transitions with the PT content dependence of Néel temperature, have been observed at T_{N2} = 370 K, 285 K, and 274 K, and T_{N1} = 8.5 K, 11 K, and 12.5 K, in the (1-x)PFW-xPT crystals, with x = 0, 0.07 and 0.27, respectively. The antiferromagnetic orderings are explained on the basis

of the superexchange magnetic interaction mechanism through – Fe^{3+} – O – Fe^{3+}– and – Fe^{3+} – O – W – O – Fe^{3+} – pathway, respectively. It is found, interestingly, that the low-temperature magnetic transition from the weakly ferromagnetic to antiferromagnetic phase increases with the increase of PT content x from 0 to 0.27, and then vanishes as x is continuously increased to 0.75. On the other hand, the (high-temperature) antiferromagnetic-to-paramagnetic phase transition temperature decreases and then disappears with the PT content increasing.

It is suggested that two different factors affect the magnetic transitions in the (1-x)PFW-xPT system. The "dilution" of the concentration of the magnetic ion Fe^{3+} by the addition of the non-magnetic PT component generally destabilizes the magnetic ordering of the substance. On the other hand, the decrease in the distance of magnetic interaction due to lattice contraction of the perovskite structure gives rise to a stronger magnetic coupling between adjacent Fe^{3+} ions in the system. The former is responsible for the vanishing of the low-temperature and high-temperature magnetic orderings at T_{N1} and T_{N2}, respectively, as the amount of PT component is increased to a large extent ($x \geq 0.75$). The latter plays an important role in the shifting towards higher temperature of the low-temperature magnetic transition and the enhancement of the weak ferromagnetism against thermal agitation with the increasing PT amount in the low-PT content crystals ($x \leq 0.27$). In this way, the substitution of the non-magnetic PT for PFW actually enhances the ferromagnetic interaction at low temperature in the PFW-PT solid solution. Such an unusual behaviour has never been reported in detail in this system. A partial magnetic phase diagram has been established, which clearly delimits the paramagnetic,

antiferromagnetic, and weak ferromagnetic phases by the low-temperature and high-temperature magnetic transition temperature curves.

The macroscopic magnetization of the crystals (1-x)PFW-xPT under an alternating magnetic field has been measured at various temperatures. In the PFW, 0.93PFW-0.07PT and 0.73PFW-0.27PT crystals, the magnetization curve M(H) at 1.9 K displays a slim hysteresis loop, indicating the weak ferromagnetic behaviour. The remnant magnetization and the hysteretic effect also increase with the PT content increasing from 0 to 0.27 and decreases with the further increase of the PT content. A nonlinear magnetization curve M(H) appears in the temperature range of T_{N1}-T_{N2}, revealing that the magnetic ordering is transformed from the ferromagnetic into antiferromagnetic phase upon heating. At temperatures above the high-temperature magnetic transition temperature T_{N2}, a perfect linear relationship between the magnetization and magnetic field is displayed, which obeys the Curie-Weiss law. Hence, the crystals are in the paramagnetic state. For the 0.25PFW-0.75PT crystal, a paramagnetic feature exists nearly in the whole measured temperature range (at least ≥ 10 K), suggesting that the long-range magnetic orderings have been destroyed as a result of high-substitution of the non-magnetic Ti^{4+} ion for Fe^{3+} ion and that Fe^{3+} ions are embedded in magnetically isolated nanoregions in the complex perovskite. The magnetization induced by magnetic field decreases with the increasing amount of PT component.

Therefore, as the perovskite structure gradually changes from a pseudo-cubic to a tetragonal phase by increasing the amount of ferroelectric and non-magnetic PT component in the PFW-PT binary system, the nature of dipole interaction transforms

from the relaxor ferroelectric short-range order to the ferroelectric long-range order. At the same time, the low-temperature magnetic ordering slightly shifts toward a higher temperature with enhanced weak ferromagnetism and then disappears, while the high-temperature magnetic transition moves toward lower temperature and then disappears. In addition, the anomalies on the temperature dependence of dielectric permittivity and enhanced magnetic hysteresis loop just happen near the compositions showing morphotropic phase boundary. These observations point to the intrinsic relationships among the microstructure, composition, dielectric and magnetic properties, and demonstrate the intriguing multiferroic features of the PFW-PT system.

8.1.5 Mössbauer Spectroscopic Studies of $Pb(Fe_{2/3}W_{1/3})O_3$ and $Pb(Fe_{2/3}W_{1/3})O_3$-$PbTiO_3$.

In order to study the effects of the magnetic (electric) properties on the Mössbauer spectra of the (1-x)PFW-xPT system, the ^{57}Fe-enriched PFW and 0.75PFW-0.25PT ceramics have been prepared and characterized for the first time by Mössbauer spectroscopy at temperatures between 373 K and 4.4 K.

At temperatures above the high-temperature magnetic ordering T_{N2}, the Mössbauer spectra of PFW display a quadrupole split doublet related to the presence of the statistically random distribution of Fe^{3+} ion on the B-sites of the perovskite structure. But, there is no obvious evidence for the two iron sites showing different quadrupole splittings reported by other authors. As the temperature is lowered to 295 K, 77 K and 4.4 K, a sextet occurs in the Mössbauer spectra, indicating that the antiferromagnetic ordering is established within PFW. In particular, the spectrum at 4.4 K shows a normal magnetic sextet with the magnetic field of 530 kOe. Therefore, it is suggested that the

iron ions at two sub-lattices in the disordered perovskite structure have the same internal magnetic field at temperatures below the low-temperature antiferromagnetic transition (T_{N1} = 9.0 K), because the weakly ferromagnetic behaviour was observed in the magnetization measurements of the PFW single crystal, as a function of temperature and magnetic field. The linewidths of distribution of magnetic fields of PFW become narrow, revealing that the magnetic field gradually increases and thermal relaxation decreases upon cooling.

On the other hand, the Mössbauer spectra of 0.75PFW-0.25PT at 295 K and 77 K are composed of a doublet and a lower-intensity magnetic component, which indicates that the onset of magnetic ordering occurs at a lower temperature in 0.75PFW-0.25PT than in PFW after the dilution of the Fe^{3+} ions by the non-magnetic PT component. On cooling to 4.4 K, the magnetic sextet dominates the Mössbauer spectrum, showing a strong internal magnetic field arising from the weakly ferromagnetic due to a canted antiferromagnetic interaction in the material at very low temperature. It is suggested that the major magnetic component at 4.4 K arises from Fe^{3+} ion on the B-site of the perovskite structure and the weak magnetic component observed at 295 K 77 K, and 4.4 K probably results from an impurity phase, most likely Fe_2O_3.

The Mössbauer spectra have also been fitted assuming the two-sites model. The different hyperfine field distributions of the iron ions from two sub-lattices of the perovskite structure were obtained at least above the magnetic transition T_{N1} for PFW. It is found that the half width of the hyperfine field distribution of 0.75PFW-0.25PT is broader than that of PFW at 4.4 K, suggesting that the degree of disordered magnetic domain is enhanced by the addition of non-magnetic component into the system.

The chemical isomer shifts and quadrupole splitting are obtained at various temperatures, indicating the presence of high-spin state of Fe^{3+}.

In conclusion, a synthetic method for the preparation of highly pure ceramics and single crystals of the $Pb(Fe_{2/3}W_{1/3}]O_3$ $-PbTiO_3$ [PFW-PT] solid solution has been developed. The dielectric/ferroelectric and magnetic properties of the binary system have been investigated, which reveals the intrinsic relationships of properties, structure and composition.